THE TAMING OF THE SCREW:
OR HOW I LEARNED TO STOP WORRYING AND LOVE ELLIPTIC FUNCTIONS

Elisabetta A. Matsumoto

A DISSERTATION

in

Physics and Astronomy

Presented to the Faculties of the University of Pennsylvania

in

Partial Fulfillment of the Requirements for the

Degree of Doctor of Philosophy

Supervisor of Dissertation

Signature _____

Randall D. Kamien

Professor of Physics and Astronomy

Graduate Group Chairperson

Signature _____

A. T. Johnson, Professor of Physics and Astronomy

Dissertation Committee

Andrea J. Liu, Professor of Physics and Astronomy

Tom C. Lubensky, Professor of Physics and Astronomy

Kathleen J. Stebe, Chair Department of Chemical and Biomolecular Engineering

Mark Trodden, Professor of Physics and Astronomy

The Taming of the Screw:

Or How I Learned to Stop Worrying and Love Elliptic Functions

COPYRIGHT

2011

Elisabetta Adriana diSomma Matsumoto

DEDICATION

To whom it may concern.

ABSTRACT

THE TAMING OF THE SCREW:
OR HOW I LEARNED TO STOP WORRYING AND LOVE ELLIPTIC FUNCTIONS

Elisabetta A. Matsumoto

Randall D. Kamien

Nonlinear elastic phenomena appear time and again in the world around us. This work considers two separate soft matter systems, instabilities in an elastic membrane perforated by a lattice of circular holes and defect textures in smectic liquid crystals. By studying the set of singularities characterizing each system, not only do the analytics become tractable, we gain intuition and insight into complex structures.

Under hydrostatic compression, the holes decorating an elastic sheet undergo a buckling instability and collapse. By modeling each of the buckled holes as a pair of dislocation singularities, linear elasticity theory accurately captures the interactions between holes and predicts the pattern transformation they undergo. The diamond plate pattern generated by a square lattice of holes achieves long ranged order due to the broken symmetry of the underlying lattice. The limited number of two dimensional lattices restricts the classes of patterns that can be produced by a flat sheet. By changing the topology of the membrane to a cylinder the types of accessible patterns vastly increases, from a chiral wrapped cylinder to pairs of holes alternating orientations to even more complex structures.

Equally spaced layered smectics introduce a plethora of geometric constraints yielding novel textures based upon topological defects. The frustration due to the incompatibility of molecular chirality and layers drives the formation of both the venerable twist-grain-boundary phase and the newly discovered helical nanofilament (HN) phase. The HN phase is a newly found solution of the chiral Landau-de Gennes free energy. Finally, we consider two limiting cases of the achiral Landau-de Gennes free energy, bending energy dominated allows defects in the layers and compression energy dominated enforces equally spaced layers. In order to minimize bending energy, smectic layers assume the morphology of minimal surfaces. Riemann's minimal surface is composed of a nonlinear sum of two oppositely

handed screw dislocations and has the morphology of a pore. Likewise, focal conic domains result from enforcing the equal spacing condition. We develop an approach to the study of focal sets in smectics which exploits a hidden Poincaré symmetry revealed only by viewing the smectic layers as projections from one-higher dimension.

Contents

1 In Which We Meet Our Protagonist and Our Story Begins **1**

1.1 Soft Matter and Defects 1

1.1.1 Symmetries, Order Parameters and Topological Defects 2

1.2 Elasticity and Pattern Formation 3

1.3 Smectics! 4

1.3.1 The Frustration of Layers and Chirality 6

1.4 Outline 6

1.4.1 Harnessing Elastic Instabilities: From Complex Pattern Formation to Functionality 7

1.4.2 Smectics! 8

2 In Which We are Presented with the Theory of Linear Elasticity and We Discover an Instability **10**

2.1 Linear Elasticity Theory 10

2.2 Elasticity in *Flatland* [1] 14

2.2.1 Identities in Orthogonal Coordinates 16

2.2.2 Linear Elasticity in Bipolar Coordinates 16

2.3 I'm Fixing a Hole 19

2.3.1 *I'm Fixing a Hole (Demo)* 19

2.3.2 *I'm Fixing a Hole (Take 2)* 22

3 In Which Dislocation Dipoles Interact and a Diamond Plate Emerges **28**

3.1 The Linear Theory of Nonlinear Elasticity 28

3.1.1 The Theory of Dislocations 29

3.2 I'm Filling a Crack 30

3.2.1 We Had to Count Them All 33

3.2.2 Stretching the Lattice 35

3.2.3 Why We Can Ignore Higher Order Terms 36

3.3 Conclusion 40

4 In Which Cylinders Complicate the Interaction and New Patterns are Formed 42

4.1 The Experiment 42

4.2 The Model 44

4.2.1 Three Simple Lattices 46

4.2.2 Another Look at the Lattices 49

4.2.3 Complex Lattices Lead to Complex Patterns 52

4.3 Conclusion 53

5 In Which Chirality Frustrates Layers and a Screw is Born 55

5.1 Introduction 55

5.2 The Landau-de Gennes Free Energy 57

5.2.1 Chirality and Frustration and the Screw Dislocation 58

5.3 The Structure of the Helical Nanofilament Phase 59

5.3.1 Phase Fields and the Screw Dislocation 59

5.3.2 A Single Bundle 60

5.3.3 Complex Analysis and Smectic Topology 61

5.3.4 A Bulk Texture and the Helical Nanofilament Phase 64

5.4 The Phase Diagram 68

5.5 Discussion 71

6 In Which We Encounter a Minimal Surface and a Pore is Opened 72

6.1 Free Energy, Smectic Topology and Minimal Surfaces 72

6.2 Riemann's Minimal Surface 74

6.2.1 Weierstrass elliptic functions 74

6.2.2 Jacobi elliptic functions 75

6.3 Pores and Defect Cores 77

6.4 Discussion 79

7 In Which Equal Spacing is Enforced and We Shed Light on Focal Conic Domains 80

8 In Which a Conclusion is Reached and We Say Goodbye **89**

Bibliography **91**

List of Figures

2.1 A two dimensional flat elastic medium undergoes a deformation, taking points $\mathbf{x}$ and $\delta\mathbf{x}$ in the undeformed material to points $\mathbf{r}(\mathbf{x})$ and $\mathbf{r}(\mathbf{x}+\delta\mathbf{x})$ in the deformed material. 10

2.2 Curves of constant α and β are circles in bipolar coordinates. 23

2.3 An elastic sheet with two circular holes cut out (a) is subjected to uniform tension (b) and compression (c). The dark blue curves are the the boundary of the holes. The other curves show deformations of the circles in (a) to aid the eye. 27

3.1 Two dipoles of strengths $\mathbf{d}_1$ and $\mathbf{d}_2$ are separated by $\mathbf{R}$. 30

3.2 A contour plot of the angular dependence of the interaction energy, Eq. (3.8), between two dislocation dipoles. 32

3.3 The groundstate orientation of the 2×2 plaquette. 33

3.4 The groundstate orientations for square lattices of 6×6 (a), 10×10 (b), 17×17 (c), and 20×20 (d). 34

3.5 The groundstate orientations for square lattices of 3×20. 35

3.6 The results of the energy minimization for a square lattice of dipoles undergoing a strain of (a) 10%, (b) 25%, (c) 50%, and (d) 75% along one of the principal axes of the lattice. These patterns qualitatively match experiments [103, 104]. 36

3.7 Set up for dipole expansion of an elongated shape symmetric about both the x- and y-axes, in this case, an ellipse. 37

4.1 (a) The experimental setup for the cylinder with a square lattice of circular holes. (b) Under a compressive strain of $\sim 12.5\%$ the circular symmetry of the holes has clearly been broken. The pattern of collapsed holes, alternating angles $\pm\theta$ with respect to horizontal, has begun to emerge. (c) The fully compressed cylinder under a strain of $\sim 25\%$ clearly displays the final pattern. The central three rows have average angles of $\theta_1 = 0.360$, $\theta_2 = -0.339$, $\theta_3 = 0.366$ from the bottom up, respectively. 43

4.2 (a) A cylinder of radius R with two dislocation dipoles $\mathbf{d}_1$ and $\mathbf{d}_2$. (b) The unrolled version of the cylinder with the first two image cylinders at $2\pi nR\hat{\mathbf{x}}$, $n = \pm 1$. 44

4.3 *left:* (Video online) A typical representative of the pattern generated by the square lattice on a cylinder. *right:* The pattern generated by a 10×5 square lattice shown on the unwrapped cylinder. All of the collapsed holes form the angle $\theta \approx 0.58$ radians with respect to the $\mathbf{x}$-axis. 47

4.4 *left:* (Video online) A sample ground state configuration of a triangular lattice on a cylinder. *right:* The unwrapped pattern made by a 9×5 triangular lattice. Dipoles alternate sign between rows, taking the values $\theta \approx \pm 50$. . . 48

4.5 *left:* (Video online) An example pattern resulting from a honeycomb lattice of 6×8 holes on a cylinder. *right:* The flattened cylinder shows all dipoles all aligned with angle $\theta \approx -0.32$ radians. 48

4.6 *left:* (Video online) By changing the alignment of the principal axes to $\pm\pi/4$ away from the axis of the cylinder, this square lattice produces a radically different patterns from the initial version. *right:* This pattern generated by a tilted square lattice of 7×7 holes features alternating rows of dipoles sitting at angle $|\theta| \approx 0.35 \approx \pi/9$ radians. 50

4.7 *left:* (Video online) The rotated triangular lattice is the third example of a rectangular lattice with a basis. The aspect ratio of the unit cell controls the average dipole angles of the "twisted" diamond plate pattern. *right:* This pattern generated by a rotated triangular lattice with 10×4 holes features alternating rows of dipoles sitting at angle $\theta \sim \pm 0.4904$ radians 50

4.8 *left:* (Video online) A new type of pattern forms from a rotated honeycomb lattice of holes on a cylinder. *right:* This pattern generated by 8×7 holes on the rotated honeycomb lattice features pairs of dipoles, both at the same angle, which. 51

4.9 The top and bottom rows of the honeycomb lattice form a boundary layer with a distinctly different pattern than the interior. The pattern of these rows exhibits an "odd-even" effect depending on the number of rows of holes. As they encircle the cylinder, the dipoles on the bottom row alternate between $\theta \approx -0.123$ and $\theta \approx -0.845$. However, the dipoles on the top row alternate between $\theta \approx -0.845$ and $\theta \approx -0.123$ for cylinders with an odd number of rows (left) and $\theta \approx 0.123$ and $\theta \approx 0.845$ for cylinders with an even number of rows (right). 52

4.10 *left:* (Video online) As the complexity of the lattice increase so too does the intricacy of the pattern it can generate. The kagome lattice of holes in a cylindrical elastic sheet produces this complicated pattern. *right:* This kagome lattice, six unit cells wide and three unit cells tall, each containing three holes, generates a complex pattern. 53

4.11 (Video online) An example application uses the pattern generated by the Kagome lattice on a cylinder as a rolling printer onto a flat substrate. . . . 54

5.1 A single bundle of helicoidal layers locally attains the absolute minimum of the chiral Landau-de Gennes free energy. The compression energy vanishes on the surface shown here in green. 61

5.2 *left:* (Video online) The smectic texture corresponding to a square lattice of bundles. The conjugate lattice of defects, $\tilde{\Theta}_{\rm sq} \sim \zeta^{-1}$, correspond to helicoids of the opposite handedness. *right:* Top view. 65

5.3 *left:* (Video online) In the bulk texture of the helical nanofilament phase, homochiral smectic bundles decorate the vertices of a hexagonal lattice. Each of the helical bundles has on average two defects corresponding to the divergence $\tilde{\Theta}_{\rm hex} \sim \zeta^{-1/2}$. *right:* Top view. 67

5.4 The contour plot of the compression energy density for single (a) square and (b) hexagonal unit cells. We approximate the region $\tilde{\Omega}$ where smectic order exists by the truncated hexagon bounded by the solid red line. Within the dashed black line the compression energy is well approximated by an expansion about the origin, while outside it an expansion about the singularities is used. 68

5.5 We show the schematic phase diagram for chiral smectics. The phase becomes unstable when the chirality exceeds $q_0 = \alpha/\lambda \sim |t_c - t|^{1/2}$ (dashed, red line). The phase transition to the HN phase occurs near the intersection between this line and the upper critical chirality q_{c_2}. 70

6.1 (Video online) Riemann's minimal surface, shown here with elliptic modulus m=0.5, is composed of two helices whose cores (shown in black) are linear with a superimposed periodic modulation. 77

6.2 (Video online) Riemann's minimal surface evolves from two oppositely handed helicoids that are infinitely far apart at $m = 0$ to a single infinitely thin pore located at the origin at $m = 1$. Shown here from two perspectives is the transformation of the surface for two values of the control parameter, $m = 0.05$ (top) and $m = 0.95$ (bottom). 78

7.1 Achronal boundaries for (a) a pair of space-like and (b) time-like separated events, both in their rest frames (left) and in a general frame (right). The corresponding smectic textures are shown below each surface, with focal lines indicated in red. 81

7.2 Two Dupin cyclide domains sharing a point of tangency in a trellis configuration. The cyclides fill conical regions extending from the point of intersection of their hyperbolae to their focal ellipse, while outside these regions the layers are continued by concentric spheres. In Minkowski space (inset, $z = 0$ subspace) the ellipses lie on the surface of an hyperboloid. Tangency of ellipses corresponds to null separation of their foci, as is most easily seen in the rest frame of one of the ellipses. 84

7.3 Two-dimensional slice ($y = 0$) of a tilt grain boundary configuration, shown both in real space and in Minkowski space. Note the "ridge" at which there is a change in orientation of the ground state: under a boost (bottom) this ridge becomes an additional focal set. 87

Chapter 1

In Which We Meet Our Protagonist and Our Story Begins

Our story begins on a small rock, orbiting a middle aged star out along a spiral arm of the Milky Way Galaxy, where it has always been the prerogative of the strange inhabitants known as humans, least of all their students of physics, to ponder the existence, origins, and laws of the universe. That, however, is not what this story is about.

1.1 Soft Matter and Defects

From the textured dimples cloaking a grain of pollen to the buckled ridges and folds of the towering Himalayan peaks and the labyrinth of pathways and pores in the mitochondrial membrane to the graceful curves of a calla lilly beautiful yet complex geometric constructs and patterns adorn much of the natural world around us. All of these seemingly disparate phenomena owe many of their properties to the elasticity theory of thin sheets. Nonlinearities in the elasticity play a crucial role in defining the morphologies for all of these systems.

Curvature, confinement and boundary conditions are among the many geometric constraints that dominate the energetics and behavior of many soft condensed matter systems. Such intrinsically geometric phenomena tend to be extremely difficult to solve analytically. A variety of methods have been generated to simplify the analysis and extract principle behaviors. Among the most powerful, field theories exploit the differences between the symmetries of the ordered and disordered states to predict both ground state morphologies and phase transitions. Such theories frequently include contributions of deformations from the ground state only to quadratic order. Harmonic interactions control the long wavelength physics, and nonlinearities exist only at finite wavenumber. As the physics cannot depend

crucially on the details of a particular theory, the singularities in a system dominate its general behaviors and interactions.

Understanding the energetic cost of a singularity is not necessarily well defined. While in a linear theory the energy is divergent, the real system cannot have an infinite energy. However, divergences are also places where linear theories break down. Topological defects present a solution to this seemingly problematic situation. Such defects represent a special class of singularity which are constrained by the symmetries of the ordered phase and cannot therefore be relaxed to the ground state.

1.1.1 Symmetries, Order Parameters and Topological Defects

Pinpointing the difference between the ordered and disordered phases requires the identification of a broken symmetry. In mean field theory, the order parameter field is a statistical measure of the local phase of the system. Near the phase transition, where it remains valid that the reduced temperature, $t = \frac{T-T_c}{T_c}$, where T_c is the transition temperature, a Landau expansion of the free energy in small values of the order parameter, respecting symmetries of both phases, accurately captures the equilibrium behavior of the system. Every broken continuous symmetry results in a zero frequency Goldstone mode. These modes are associated with long wavelength deformations away from the ground state.

The group defined by the symmetries of the ordered state determines the set of allowed configurations, in particular, symmetry transformations that take one ground state of the system to an equivalent but distinct ground state. The language of homotopy theory has proven an exceedingly powerful tool in the understanding of defects in ordered media [83, 76, 49]. It is important to draw the distinction between deformations and defects. Deformations, although potentially energetically costly, are trivial topologically. That is to say, they can be smoothed away by local transformations. Topological defects, on the other hand, are global properties of the system.

1.2 Elasticity and Pattern Formation

Elastic instabilities have been long been utilized as a means of generating patterns in thin films. The simplest example occurs when a freely suspended elastic sheet with clamped edges under tension develops an instability toward developing wrinkles parallel to direction of the tension [16, 15]. The buckling instability of thin elastic films on the surface of a bulk elastic substrate is well understood [13, 22], of particular note, the development of a herringbone patter of wrinkles [20, 21]. It remains a challenge to direct the formation of patterns using these methods. Over short lengths, the surface wrinkles are neatly organized, yet, long ranged order is not maintained over larger length scales. Mastery of such processes would revolutionize the fabrication and design of novel materials with specific properties. Synthetic elastomeric membranes can be coaxed into exhibiting these sorts of elastic instabilities under swelling, buckling, and dewetting [98, 13, 43, 40, 58, 52]; these effects have been used to build microlenses [18, 45] and stretchable electronics [57].

Zhang *et al.* [103] showed that when an elastomeric poly(dimethylsiloxane) (PDMS) membrane with a square lattice of circular holes (with diameter roughly half the lattice spacing) in it is uniformly swollen or, alternatively, is compressed hydrostatically, the holes deform into a striking diamond plate pattern, depicted in Figure 3.4 for several $N \times N$ square lattices and shown in schematically [103]. The order persists for upwards of 10^5 times the original lattice spacing with only phase-slip defects, which do not change the overall symmetry of the pattern. It is interesting to note that the same diamond plate pattern emerges from membranes with vastly different lattice spacings, ranging from 1 μm to 1 cm. Because the same mechanism causes patterns to form over such a wide range of length scales, this technique is well suited to create devices for many fields and industries. In particular, a membrane of holes, which possesses no photonic band-gap, induces a photonics band-gap is in the diamond plate state, it has a photonic band-gap [105]. Likewise, the material's novel auxetic properties make it appealing for metamaterial applications [8]. We note that the thin, perforated film of PDMS sits a top a thick, solid PDMS film. This forces the deformations of the thin membrane to be two-dimensional and simplifies our following

analysis.

This effect occurs in the highly non-linear regime of elasticity, complicating the analysis. Technological advances have made computational techniques, for instance finite element simulations, increasingly feasible. Only finite element simulations using specific models of nonlinear elasticity capture the entire process of the holes collapsing [77, 7]. These nonlinear effects are needed to predict the final shape of the collapsed holes and not merely their orientation. As the complexity of the system grows, such methods tend to be more accurate but lack the ability to distinguish between mechanisms responsible for different phenomena. Analytic calculations generate intuitive solutions and can form the basis for subsequent numerical calculations. With the sole assumption that each hole collapses to some elongated shape, our model uses only linear elasticity to successfully predict the orientational order in the diamond plate pattern and the herringbone pattern formed from an underlying triangular lattice. Not only does our model shed light on the interactions in the system, it greatly facilitates the rational design of other patterns and devices.

Merely by patterning the elastic membrane with a lattice of holes, one is able to direct the resulting buckling instability [103, 77, 74, 104]. Under uniform swelling or hydrostatic pressure, the holes in the lattice collapse and form a diamond plate pattern. The main mechanism for collapse is similar to the Von Mises buckling instability of thin shelled piper under hydrostatic pressure [100] and the collapse of two dimensional rings under pressure which has been studied for over a century [65, 78, 56]. However due to the width of membrane in between neighboring holes, these linear approximations do not capture all of the physics in a two dimensional sheet with holes. The broken symmetry of the underlying lattice is responsible for breaking the collapsing holes.

1.3 Smectics!

Symmetries govern the unique physics of liquid crystalline phases. Broken rotational symmetry of the constituent anisotropic mesogens enables the generation of many new phases with aspects of both liquid and crystalline order. The highest symmetry state is an isotropic liquid of molecules. The nematic phase is characterized by the development

of orientational order, while the centers of mass of the particles still behave as a three dimensional fluid. By coarse-graining over the individual orientations, the director field $\mathbf{n}(\mathbf{x})$ is a unit vector which describes average orientation of the nematic at position $\mathbf{x}$. Technically speaking, instead of a unit director field, the average orientation should be described as a unit line field, as the head and tail of each mesogen are indistinguishable. However, for the unit vector formalism to holds every term in the energy must remain invariant under the transformation $\mathbf{n}(\mathbf{x}) \to -\mathbf{n}(\mathbf{x})$. Consider a nematic ground state where all molecules point along the $\hat{\mathbf{z}}$ direction. Low energy deformations away from the ground state originate from the two Goldstone modes of the system, corresponding to the two broken rotational symmetries. Linear combinations of these deformations give us the Frank free energy for nematics,

$$F_{\text{Frank}} = \frac{1}{2}\int d^3x \Big\{ K_1 \big(\nabla \cdot \mathbf{n}\big)^2 + K_2 \big(\mathbf{n} \cdot \nabla \times \mathbf{n}\big)^2 + K_3 \big((\mathbf{n} \cdot \nabla)\mathbf{n}\big)^2 \Big\}, \tag{1.1}$$

where the K_i are the elastic moduli determining the cost of the splay, twist and bend distortions, respectively [82, 32, 25].

Molecular chirality is responsible for breaking an additional symmetry in the cholesteric (N^*) phase. When neighboring molecules prefer to align themselves at a fixed angle with respect to their neighbors, instead of lying parallel, the resulting structure displays an additional periodicity associated with the rotation of the molecules. The effective chirality field $K_2 q_0$ indicates a preference for nonzero twist in the system, where $q_0 = -\mathbf{n} \cdot \nabla \times \mathbf{n}$ is a measure of the rotation of the molecules. This field couples to the free energy via $K_2 q_0 \int d^3x (\mathbf{n} \cdot \nabla \times \mathbf{n})$, such that the chiral Frank free energy is

$$F_{N^*} = \frac{1}{2}\int d^3x \Big\{ K_1 \big(\nabla \cdot \mathbf{n}\big)^2 + K_2 \big(\mathbf{n} \cdot \nabla \times \mathbf{n} + q_0\big)^2 + K_3 \big((\mathbf{n} \cdot \nabla)\mathbf{n}\big)^2 \Big\}, \tag{1.2}$$

which attains an absolute minimum for the director field $\mathbf{n}^* = \cos(q_0 z)\mathbf{e}_x + \sin(q_0 z)\mathbf{e}_y$.

The development of one dimensional periodic order signifies the onset of smectic order, lending itself naturally to a description by a complex scalar order parameter $\psi(\mathbf{x}) = \psi_0(\mathbf{x}) e^{i q_{\text{sm}} \Phi(\mathbf{x})}$, where the magnitude of the order $\psi_0(\mathbf{x})$ indicates the presence of smectic

order and the phase denotes the position of the layers, $\Phi(\mathbf{x}) = nd$, where $d = 2\pi/q_{\rm sm}$ is the ideal layer spacing. Within each layer, the molecules are free to diffuse and behave as a two dimensional fluid. The free energy functional must contain additional terms associated with the interactions of this newly formed mass density wave. The layers tend to form with their normals, $\mathbf{N} = \nabla\Phi(\mathbf{x})/|\nabla\Phi(\mathbf{x})|$, aligned with the nematic director field. This induces a gauge-like coupling term in the free energy, assigning a cost for the normal to deviate from the director field $\left|(\nabla - iq_{\rm sm}\mathbf{n})\psi(\mathbf{x})\right|^2$. A Landau expansion in the smectic order parameter completes the Landau-de Gennes free energy for smectics,

$$F_{\rm L-dG} = \int d^3x \Big\{ C\left|(\nabla - iq_{\rm sm}\mathbf{n})\psi(\mathbf{x})\right|^2 + t\left|\psi(\mathbf{x})\right|^2 + \frac{u}{2}\left|\psi(\mathbf{x})\right|^4 + f_{\rm Frank} \Big\}, \tag{1.3}$$

where t is the reduced temperature [24].

1.3.1 The Frustration of Layers and Chirality

Attempts to grow a smectic from an underlying cholesteric phase reveal an added frustration in the system. It is impossible to simultaneously satisfy $\mathbf{N} = \nabla\Phi(\mathbf{x})/|\nabla\Phi(\mathbf{x})|$ and $\mathbf{N}\cdot\nabla\times\mathbf{N} = -q_0$. In 1972, de Gennes famously noted an analogy between the frustrated system of chiral smectics and superconductors [24]. A twist Ginzburg parameter κ, which depends only on material parameters, governs the phase behavior of the chiral smectic. Type I materials $\kappa < 1/\sqrt{2}$ have a high temperature cholesteric phase and a low temperature smectic A phase, which expels all twist; whereas type II materials $\kappa > 1/\sqrt{2}$ have an additional intermediate phase, known as the twist-grain-boundary (TGB) phase. A proliferation of screw dislocations allow twist to penetrate the TGB phase, analogous to the Abrikosov vortex lattice phase of superconductors [84].

1.4 Outline

This manuscript considers two main problems in nonlinear elasticity theory. Chapters 2-4 focus on the formation and design of complex patterns by exploiting elastic instabilities, while Chapters 5-7 address a variety of problems in the theory of topological defects in smectics.

1.4.1 Harnessing Elastic Instabilities: From Complex Pattern Formation to Functionality

Our system consists of a two dimensional elastic sheet, confined to the plane, with a square array of circular holes it it. Under hydrostatic compression, the membrane undergoes deformation, linearly at first, and then the boundaries of the holes buckle and eventually collapse, forming a diamond plate pattern. We briefly introduce the reader to the formalism of linear elasticity theory in Chapter 2, paying particular attention to results peculiar to flat two dimensional elastic media. As it is our goal to study the deformations of a system of holes in an elastic membrane, prudence warrants a review of systems of one and two holes in linear elasticity theory. The system of two holes can be worked out entirely analytically in bipolar coordinates [66, 50, 74]. Analytic calculations of the stresses in systems of many holes proved an impressive *tour de force* in the late 1930s and early 1940s [47, 48, 38]. Although advances have been made in the study of systems of multiple holes [62], analytic calculations of the instability remain elusive.

Chapter 3 studies the perforated membrane from a new point of view. We assume that there is an instability toward the collapse of holes in our membrane. We are now free to use linear elasticity theory to look at the interaction between collapsed holes. The analysis of this system draws inspiration from the theory of cracks [63]. The equilibrium shape of a crack in a membrane and the resulting stresses are the same as the stresses caused by extra material with the same shape as the crack inserted into an isotropic elastic sheet. Formally, the added material is a continuous array of dislocation singularities, infinitesimally thin strips of material stacked one upon another. An analogous model describes the deformation of holes. Under the auspices of linear elasticity theory, interactions between two collapsed holes have a remarkably simple form, and the energetics of a system of hole is merely a superposition of pairwise linear terms. The pairwise interaction scales as $\sim r^{-2}$ in two dimensions. The long ranged nature of the interaction prevents the use of a standard lattice model method of solving for ground states and phase transitions, as the interaction between *all* pairs of holes must be accounted for in the energy. Using this approximation, we are able to study a number of systems, in particular the lattice of $N \times N$ holes in an infinite

elastic sheet. Deformations associated with the collapsed holes may be combined with other linear elastic deformations. We consider the effect of a external applied tension prior to the holes undergoing the buckling instability. The resulting morphologies qualitatively match the findings in experiments [103, 74].

Solely studying systems of holes in an infinite flat elastic membrane limits the set of possible patterns that can be produced. In Chapter 4, we consider the effects of changing the topology of our elastic film from a flat sheet to a cylinder. Because the interaction between pairs of holes is long ranged, the effect of cylindrical topology is nontrivial. Keeping in mind the ultimate goal of the rational design of complex patterns in two dimensions, we begin by cataloging the patterns generated by simple lattices. Our strategy is twofold, not only do we extend the analysis presented in the previous chapter, but we conduct an experiment to verify that assumptions made for the flat sheet still hold in this new topology. After working out the pairwise interaction in this topology, we examine the equilibrium configurations of three simple lattices.

1.4.2 Smectics!

Chiral smectics introduce a new complication into the theory of elasticity. Not only do geometric constraints effect the morphology of the smectic texture, frustration between layers and chirality can induce defects to proliferate. As we shall discover in Chapter 5, the TGB phase is not the only stable "mixed" phase of chiral smectics, the helical nanofilament phase of bent core liquid crystals employs a hierarchical structure composed of a hexagonal lattice of coherently rotating, homochiral helical bundles, each containing $5-7$ layers [46, 73]. Single helical bundles are an absolute minimizer of the Landau-de Gennes free energy. However, the radially increasing compression energy limits the radius of the single bundle. The assembly of these bundles into a lattice completes the bulk texture, with the caveat that such assemblies must include defects.

Although the smectic free energy looks remarkably similar to the equations for electromagnetism or superconductors, the additional constraint enforcing both the nematic director and the surface normal to be unit vectors introduces intrinsic nonlinearities. A powerful

technique used to calculate the energetics and relative stability of different smectic phases assumes a topology for the smectic layers and utilizes differential geometric techniques to determine the morphology of the resulting smectic phase [53, 51, 26, 27, 54, 85, 86].

In the case of smectics dominated by bending energy, the energetic cost comes from the diverging compression energy due to the defect cores. The bending energy is therefore minimized by a minimal surface of the correct topology. In Chapter 6, we consider the smectic containing two screw dislocations of opposite handedness which has the topology of Riemann's minimal surface. Analysis of Riemann's minimal surface, a one parameter family of surfaces foliated by circles, demonstrates that the corresponding smectic contains two screw dislocations of opposite charge. In order to maintain flat layers at infinity, the dislocation cores are forced to bend. The amplitude of the waves increases as the average separation of the defect cores decreases.

Chapter 7 is primarily concerned with the opposite limit, in which the penalty for compressing equally spaced layers dominates over the cost bending the layers. Focal conic domains, *the* ubiquitous smectic texture, result from enforcing the condition of equally spaced layers [34, 33, 11]. As with Riemann's minimal surfaces, focal conic textures are also controlled by their set of singularities. We are obliged to ask the question: what types of singularities can form in a system of equally spaced layers? To gain insight into this question, it behooves us to first understand the conditions under which equally spaced layers can exist. Instead of working within the bounds of three dimensional space, viewing equally spaced layers as projections of level sets of surfaces in one higher dimension. In particular, d dimensional equally spaced layers are described by null hypersurfaces in $(d+1)$ Minkowsi space, $\mathbb{R}^{d,1}$. Upon recalling that null separated objects remain invariant under Lorentz transformations, all focal conic domains are merely toric focal conics in their "rest frame" as viewed by an observer in a different frame. This perspective enables us to study many complicated focal conic textures, including the *treillis à réseaux* texture along with Friedel's law of corresponding cones and the tilt grain boundary phase [4].

Chapter 2

In Which We are Presented with the Theory of Linear Elasticity and We Discover an Instability

2.1 Linear Elasticity Theory

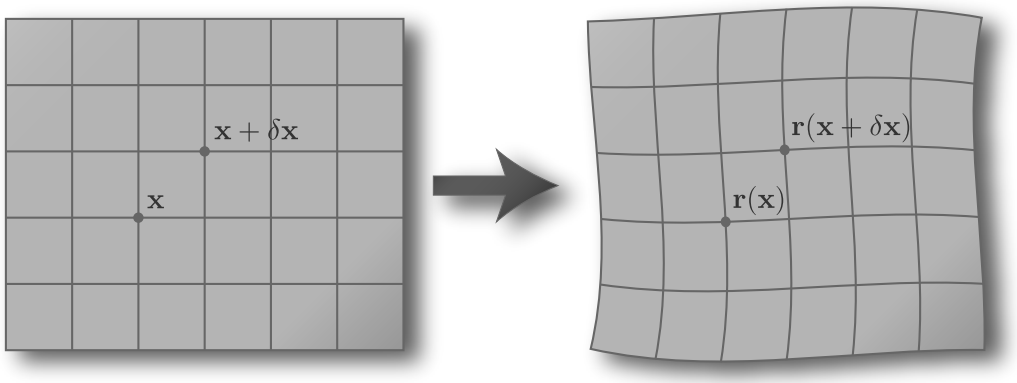

Figure 2.1: A two dimensional flat elastic medium undergoes a deformation, taking points $\mathbf{x}$ and $\delta\mathbf{x}$ in the undeformed material to points $\mathbf{r}(\mathbf{x})$ and $\mathbf{r}(\mathbf{x}+\delta\mathbf{x})$ in the deformed material.

The theory of linear elasticity describes the deformation and energetics of a solid body under external force or load. While this theory was originally developed over a century ago and has been presented time and again [70, 63, 39, 42], this brief tutorial will illuminate a few salient features as well as familiarize the reader to our notation. The goal is to develop the framework for a generalization of Hooke's Law for solid three dimensional bodies. When a solid is deformed, the displacement of every point, $\mathbf{x}$ is described by the vector $\mathbf{u}$, such that its final positions are given by $\mathbf{r}(\mathbf{x}) = \mathbf{x} + \mathbf{u}(\mathbf{x})$. Let us first consider two points separated by $ds = \sqrt{\mathbf{dx}\cdot\mathbf{dx}}$ that are very close together. After being deformed, their separation becomes ds', where $ds'^2 = (dx_i + du_i)^2$ using the Einstein summation convention. By

noting $du_i = (\partial u_i/\partial x_k)dx_k$, we may rewrite this as

$$\begin{aligned} ds'^2 &= ds^2 + \sum_{ik}\left(\frac{\partial u_i}{\partial x_k} + \frac{\partial u_k}{\partial x_i} + \frac{\partial u_i}{\partial x_k}\frac{\partial u_k}{\partial x_i}\right) dx_i dx_k \\ &= ds^2 + 2\sum_{ik} u^L_{ik} dx_i dx_k, \end{aligned} \tag{2.1}$$

where u^L_{ik} is the Lagrangian strain tensor. However, for small deformations we need only consider terms linear in $\partial u_i/\partial x_k$ and the linearized strain tensor is

$$u_{ik} = \frac{1}{2}\left(\frac{\partial u_i}{\partial x_k} + \frac{\partial u_k}{\partial x_i}\right). \tag{2.2}$$

In the spirit of Hooke's Law, there is an energy cost associated with displacing every point from its equilibrium position. While the general form is quite complicated, to first order the energy can be constructed from the linear strain tensor. Because the strain tensor is a symmetric rank two tensor, the only two possible scalar invariants that can be constructed are $(u_{ii})^2$ and $(u_{ik})^2$. Because these terms are invariants of the system, they cannot depend on coordinate system. From this we deduce the form of the energy density

$$\epsilon = \frac{1}{2}\left(\lambda {u_{ii}}^2 + 2\mu {u_{ik}}^2\right), \tag{2.3}$$

where λ and μ are Lamé coefficients. Since any deformation may be written in terms of uniform or hydrostatic compression and pure shear, we rewrite the strain tensor, $u_{ik} = \frac{1}{3}\delta_{ik}u_{ll} + (u_{ik} - \frac{1}{d}\delta_{ik}u_{ll})$. The hydrostatic compression is given by the first term, as it involves only the trace of u_{ik}. And the second term describes pure shear because its trace is zero. In terms of these quantities, the energy becomes

$$\epsilon = \frac{1}{2}\left(K {u_{ll}}^2 + 2\mu\left(u_{ik} - \tfrac{1}{d}\delta_{ik}u_{ll}\right)^2\right), \tag{2.4}$$

where the bulk modulus $K = \lambda + \frac{1}{d}\mu$, and μ is the shear modulus.

When a body is deformed, the displaced internal elements experience forces which tend to restore them to their equilibrium positions. The volume element bounded by the surfaces $x = x_0$, $x = x_0 + \delta x$, $y = y_0$, $y = y_0 + \delta y$, $z = z_0$, and $z = z_0 + \delta z$ experiences a force along

any surface with normal $\mathbf{n}$, $f_i = \sigma_{ik} n_k$, where σ_{ik} is the stress tensor and

$$F_i^{\text{ext}} = \oint dA\, \sigma_{ik}\, n_k = \int dV \frac{\partial \sigma_{ik}}{\partial x_k}. \tag{2.5}$$

In equilibrium, the internal stresses of the system must balance the external forces exerted upon it; thus, the equilibrium condition for the system is

$$\frac{\partial \sigma_{ik}}{\partial x_k} - f_i^{\text{ext}} = 0. \tag{2.6}$$

If the system is deformed an infinitesimal amount δu_i, the work done by the change in internal stresses is the force times the displacement, $W = \int dV\, (\partial \sigma_{ik}/\partial x_i) \delta u_k$. When integrated by parts, the work is

$$\begin{aligned} W &= \oint dA\, \sigma_{ik}\, n_k\, \delta u_i - \int dV \sigma_{ik} \frac{\partial \delta u_i}{\partial x_k} \\ &= -\frac{1}{2} \int dV \sigma_{ik} \left(\frac{\partial \delta u_k}{\partial x_i} + \frac{\partial \delta u_i}{\partial x_k} \right) \\ &= -\int dV \sigma_{ik}\, du_{ik}. \end{aligned} \tag{2.7}$$

Note that the surface integral vanishes because $\sigma_{ik} = 0$ at infinity. Thus, $dE = \sigma_{ik}\, \delta u_{ik}$. By taking the total differential of equation (2.4), $dE = K\, u_{ll}\, du_{ll} + 2\mu(u_{ik} - \frac{1}{d}\delta_{ik} u_{ll}) d(u_{ik} - \frac{1}{d}\delta_{ik} u_{ll}) = \left(K\, u_{ll}\, \delta_{ik} + 2\mu(u_{ik} - \frac{1}{d}\delta_{ik} u_{ll}) \right) du_{ik}$, we can rewrite the stress tensor in terms of the strain tensor, $\sigma_{ik} = K \delta_{ik} u_{ll} - 2\mu \left(u_{ik} - \frac{1}{d}\delta_{ik} u_{ll} \right)$, or conversely, the strain in terms of the stress, $u_{ik} = \frac{1}{d^2 K} \delta_{ik} \sigma_{ll} + \frac{1}{2\mu} \left(\sigma_{ik} - \frac{1}{d} \delta_{ik} \sigma_{ll} \right)$.

Similarly, it is instructive to consider a homogeneous deformation, which has constant stain tensor everywhere in the volume. For a d-dimensional solid, uniform pressure is applied to the faces with normals in the $\pm\hat{z}$ directions. In 3-dimensions, for example, we consider the simple compression of a rod. This implies that $\sigma_{zi} n_i = p$, or $\sigma_{zz} = p$. Thus, all off diagonal components of the strain tensor are zero, and the diagonal components are $u_{ll} = p(\frac{1}{dK} - \frac{1}{2\mu})/d$, for all $l \neq z$, and $u_{zz} = p(\frac{1}{dK} + \frac{d-1}{\mu})/d$. The relative longitudinal compression is given by $u_{zz} = p/Y_d$, where

$$Y_d = \frac{2d^2 K \mu}{2\mu + (d^2 - d)K} \tag{2.8}$$

is the d-dimensional Young's modulus. The ratio of transverse extension to longitudinal compression is given by the Poisson ratio $\gamma = -u_{ll}/u_{zz} = (dK - 2\mu)/((d^2 - d)K + 2\mu)$. Conversely, the bulk and shear moduli written in terms of the Young's modulus and Poisson ratio are, respectively, $K = \frac{1}{d}Y_d/(1 - (d-1)\gamma)$ and $\mu = \frac{1}{2}Y_d/(1+\gamma)$. The stress tensor is given in terms of the strain tensor by,

$$\sigma_{ik} = \frac{Y_d}{1+\gamma}\left(u_{ik} + \frac{\gamma}{1-(d-1)\gamma}\delta_{ik}u_{ll}\right), \tag{2.9}$$

and the converse by,

$$u_{ik} = \frac{1}{Y_d}\left((1+\gamma)\sigma_{ik} - \gamma\delta_{ik}\sigma_{ll}\right). \tag{2.10}$$

The conventional form of the energy is given in terms of Y_d and γ,

$$E = \frac{Y_d}{2(1+\gamma)}\int d^d x \left({u_{ik}}^2 + \frac{\gamma}{1-(d-1)\gamma}{u_{ll}}^2\right). \tag{2.11}$$

Now that we have derived the relations between the stress and strain tensors, the equilibrium condition may be recast in terms of the displacement vector,

$$\frac{Y_d}{2(1+\gamma)}\left(\frac{\partial^2 u_i}{\partial x_k^2} + \frac{1-(d-3)\gamma}{1-(d-1)\gamma}\frac{\partial^2 u_l}{\partial x_i \partial x_l}\right) - f_i = 0. \tag{2.12}$$

If the force only acts through the surface, then f_i vanishes in the bulk and we recover the result that $\nabla^2\nabla\cdot\mathbf{u} = 0$ from which it follows that $\nabla^4\mathbf{u} = 0$.

In the following, we will rely upon orthogonal coordinates, ξ_μ, with the diagonal metric $ds^2 = h_\alpha^2 d\alpha^2 + h_\beta^2 d\beta^2 = \sum_\mu (h_\mu d\xi_\mu)^2$ [1]. In general, the orthogonal coordinates are nonholonomic but the benefit of orthogonality outweighs this complication. What is the linearized Lagrangian strain tensor in our new coordinates? By definition

$$ds'^2 - ds^2 = 2u^L_{\mu\nu} h_\mu d\xi_\mu h_\nu d\xi_\nu \tag{2.13}$$

and

$$ds'^2 = \sum_i \left(dx_i + \frac{\partial u_i}{\partial x_k}dx_k\right)\left(dx_i + \frac{\partial u_i}{\partial x_j}dx_j\right) \tag{2.14}$$

[1] We use the convention x_i to represent the i^{th} component of a Cartesian coordinate system, where the subscript can be any Roman letter. Components of another orthogonal coordinate system are denoted by ξ_μ, for any Greek subscript.

Since $\mathbf{u}$ is a vector, we may write it in either coordinate system:

$$\mathbf{u} = u_i \hat{x}_i = u_\mu \hat{\xi}_\mu \tag{2.15}$$

from which we have $u_i = \sum_\mu u_\mu \hat{\xi}_\mu \cdot \hat{x}_i$. In order to calculate the direction cosines, we note that if $x_i = x_i(\xi_\mu)$, then

$$\hat{\xi}_\mu = \frac{1}{\sqrt{\sum_j \left(\frac{\partial x_j}{\partial \xi_\mu}\right)^2}} \sum_i \frac{\partial x_i}{\partial \xi_\mu} \hat{x}_i \tag{2.16}$$

We recognize the radicand in the denominator as h_μ^2 and we have

$$\left(dx_i + \frac{\partial u_i}{\partial x_k} dx_k\right) = \left[\frac{\partial x_i}{\partial \xi_\mu} + \frac{\partial}{\partial \xi_\mu}\left(\frac{u_\rho}{h_\rho}\frac{\partial x_i}{\partial \xi_\rho}\right)\right] d\xi_\mu \tag{2.17}$$

Using orthogonality, $\sum_i \frac{\partial x_i}{\partial \xi_\mu}\frac{\partial x_i}{\partial \xi_\nu} = h_\mu^2 \delta_{\mu\nu}$, it is straightforward to find

$$\begin{aligned} u_{\mu\nu} \;=\; \sum_{i\rho} \Bigg[& h_\mu \frac{\partial u_\mu}{\partial \xi_\nu} + h_\nu \frac{\partial u_\nu}{\partial \xi_\mu} + \frac{\partial}{\partial \xi_\mu}\left(\frac{1}{h_\rho}\frac{\partial x_i}{\partial \xi_\rho}\right)\frac{\partial x_i}{\partial \xi_\nu} u_\rho \\ & + \frac{\partial}{\partial \xi_\nu}\left(\frac{1}{h_\rho}\frac{\partial x_i}{\partial \xi_\rho}\right)\frac{\partial x_i}{\partial \xi_\mu} u_\rho \Bigg] / (2 h_\mu h_\nu), \end{aligned} \tag{2.18}$$

where we only sum over the repeated indices i and ρ, not μ or ν associated with the scale factor h. In the following we will adopt the Einstein summation convention and, only when there is ambiguity, will we specify which indices are to be implicitly summed.

2.2 Elasticity in *Flatland* [1]

Our ultimate goal is to study the effects of uniform tension on a thin sheet of elastic material with a square lattice of circular holes cut in it, as it models an elastic sheet that is uniformly swollen. In general, the resulting deformations are constant across the thickness of the sheet and may be considered to be purely longitudinal. This is because forces act primarily in the plane of the film, yielding the boundary condition $\sigma_{ik} n_k = 0$. In the nanoscale experimental system [103] the elastic membrane was on a substrate, which suppresses out of plane buckling. Henceforth, we will only consider two dimensional systems with planar deformations.

Let us pause for a minute to derive the equilibrium conditions of this system. Since the deformations are constant throughout the thickness of the sheet, we may assume that $u_{zz} =$

0, and thus $\sigma_{zz} = \sigma_{iz} = 0$. We are left with the two equilibrium equations $h\partial\sigma_{ik}/\partial x_k = -p_i$, where $i, k = x, y$, and h is the thickness of the film. When no external body forces are present the equations of equilibrium reduce to $\partial\sigma_{ik}/\partial x_k = 0$ or,

$$\frac{\partial\sigma_{xx}}{\partial x} + \frac{\partial\sigma_{xy}}{\partial y} = 0, \quad \frac{\partial\sigma_{xy}}{\partial x} + \frac{\partial\sigma_{yy}}{\partial y} = 0. \tag{2.19}$$

Viewing these both as equations of the form $\nabla \cdot \mathbf{A} = 0$, we know that $\sigma_{xi} = \epsilon_{ik}\partial_k\phi_y$ and $\sigma_{jy} = \epsilon_{jk}\partial_k\phi_x$ and it follows that $\partial_x\phi_y + \partial_y\phi_x = \sigma_{xy} - \sigma_{xy} = 0$ (where ϵ_{ik} is the totally antisymmetric tensor). Thus $\phi_m = \epsilon_{mn}\partial_n\chi$ for some scalar χ, known as the Airy stress function. We thus have $\sigma_{ik} = \epsilon_{im}\epsilon_{kn}\partial_m\partial_n\chi$. Moreover, since $u_{ik} = (\partial_i u_k + \partial_k u_i)/2$, we have $\epsilon_{im}\epsilon_{kn}\partial_i\partial_k u_{mn} = 0$. The relation between stress and strain, (2.9) implies that

$$\epsilon_{im}\epsilon_{kn}\frac{\partial^2\sigma_{mn}}{\partial x_i\partial x_k} = \frac{Y_d}{1+\gamma}\left(0 + \frac{\gamma}{1-(d-1)\gamma}\nabla^2\nabla\cdot\mathbf{u}\right) = 0 \tag{2.20}$$

As a result, we deduce that the stress function satisfies the biharmonic equation, $\nabla^4\chi = 0$. In orthogonal coordinates, we recast the components of the stress tensor in terms of the Airy stress function by taking advantage of Eq. (2.22) and reexpressing σ_{ij} in terms of $\sigma_{\mu\nu}$,

$$\sigma_{\mu\nu} = \sum_{\rho\lambda}\epsilon_{\mu\lambda}\frac{1}{h_\lambda}\left[\epsilon_{\nu\rho}\frac{\partial}{\partial\xi_\lambda}\left(\frac{1}{h_\rho}\frac{\partial\chi}{\partial\xi_\rho}\right) + \epsilon_{\mu\rho}\frac{1}{h_\mu h_\nu}\frac{\partial h_\rho}{\partial\xi_\mu}\frac{\partial\chi}{\partial\xi_\nu}\right], \tag{2.21}$$

where $\epsilon_{\alpha\beta} = 1$ because $\{\hat{\boldsymbol{\alpha}}, \hat{\boldsymbol{\beta}}\}$ is a right-handed orthonormal basis. Equations (2.21) are solutions to the equilibrium equations, Eq. (2.23), and the Airy stress function solves the biharmonic equation in *orthogonal* coordinates.

In curvilinear coordinates, this entire discussion can be repeated and the stress tensor in these coordinates is merely a transformation of the stress tensor in Cartesian coordinates:

$$\sigma_{\mu\nu} = \frac{1}{h_\mu}\frac{1}{h_\nu}\sum_{ik}\frac{\partial x_i}{\partial\xi_\mu}\frac{\partial x_k}{\partial\xi_\nu}\sigma_{ik}, \tag{2.22}$$

where, again, there is no sum over μ or ν. The equilibrium conditions become

$$\begin{aligned}\sum_{i\nu\lambda}\frac{1}{h_\nu}\frac{\partial}{\partial\xi_\nu}\left(\frac{1}{h_\lambda}\frac{\partial x_i}{\partial\xi_\lambda}\right)\left[\frac{1}{h_\mu}\frac{\partial x_i}{\partial\xi_\mu}\sigma_{\nu\lambda} + \frac{1}{h_\nu}\frac{\partial x_i}{\partial\xi_\nu}\sigma_{\mu\lambda}\right] \\ + \frac{1}{h_\nu}\frac{\partial\sigma_{\mu\nu}}{\partial\xi_\nu} - f_\mu^{\text{ext}} = 0.\end{aligned} \tag{2.23}$$

where we have followed the same procedure as in the derivation of $u_{\mu\nu}$ which requires expanding the tensor in both the $\hat{x}_i$ and $\hat{\xi}_\mu$ frames.

2.2.1 Identities in Orthogonal Coordinates

We include these for completeness. These were necessary for us to study the Airy stress formalism in orthogonal coordinates and we did not find these, presumably known identities, in any reference.

Consider the general set of orthogonal coordinates, $\{\alpha(x,y), \beta(x,y)\}$. The new basis preserves length of the differential line element, $ds^2 = dx^2 + dy^2 = h_\alpha^2 d\alpha^2 + h_\beta^2 d\beta^2 = h_\alpha^2 \left(\frac{\partial\alpha}{\partial x}dx + \frac{\partial\alpha}{\partial y}dy\right)^2 + h_\beta^2 \left(\frac{\partial\beta}{\partial x}dx + \frac{\partial\beta}{\partial y}dy\right)^2$, defining the scale functions $h_\alpha^{-2} = \left(\frac{\partial\alpha}{\partial x}\right)^2 + \left(\frac{\partial\alpha}{\partial y}\right)^2$ and $h_\beta^{-2} = \left(\frac{\partial\beta}{\partial x}\right)^2 + \left(\frac{\partial\beta}{\partial y}\right)^2$. However, it is often more useful to consider Cartesian coordinates as functions of the new orthogonal ones, $\{x(\alpha,\beta), y(\alpha,\beta)\}$, which yield an equivalent statement of the scale functions $h_\alpha^2 = \left(\frac{\partial x}{\partial\alpha}\right)^2 + \left(\frac{\partial y}{\partial\alpha}\right)^2$ and $h_\beta^2 = \left(\frac{\partial x}{\partial\beta}\right)^2 + \left(\frac{\partial y}{\partial\beta}\right)^2$. By transforming from orthogonal back to Cartesian coordinates, the differential line element gives $h_\alpha^2 \left(\frac{\partial x}{\partial\alpha}\right)^2 + h_\beta^2 \left(\frac{\partial x}{\partial\beta}\right)^2 = 1$ and $h_\alpha^2 \left(\frac{\partial y}{\partial\alpha}\right)^2 + h_\beta^2 \left(\frac{\partial y}{\partial\beta}\right)^2 = 1$; from which, we obtain the first set of identities:

$$\begin{aligned} \frac{\partial x}{\partial\alpha} &= h_\alpha^2 \frac{\partial\alpha}{\partial x}, \quad \frac{\partial y}{\partial\alpha} = h_\alpha^2 \frac{\partial\alpha}{\partial y} \\ \frac{\partial x}{\partial\beta} &= h_\beta^2 \frac{\partial\beta}{\partial x}, \quad \frac{\partial y}{\partial\beta} = h_\alpha^2 \frac{\partial\beta}{\partial y}. \end{aligned} \tag{2.24}$$

2.2.2 Linear Elasticity in Bipolar Coordinates

For clarity's sake, we take a moment to explicitly write out the useful equations in bipolar coordinates. From equations (2.18), we simply read off the components of the strain tensor

$$\begin{aligned} u_{\alpha\alpha} &= \frac{1}{h}\frac{\partial u_\alpha}{\partial\alpha} + \frac{1}{h^2}\frac{\partial h}{\partial\beta}u_\beta, \quad u_{\beta\beta} = \frac{1}{h}\frac{\partial u_\beta}{\partial\beta} + \frac{1}{h^2}\frac{\partial h}{\partial\alpha}u_\alpha, \\ 2u_{\alpha\beta} &= \frac{\partial}{\partial\alpha}\left(\frac{u_\beta}{h}\right) + \frac{\partial}{\partial\beta}\left(\frac{u_\alpha}{h}\right). \end{aligned} \tag{2.25}$$

The stress tensor may be written as a function of the Airy stress function χ, from equation (2.21)

$$\begin{aligned}
\sigma_{\alpha\alpha} &= \frac{1}{h}\frac{\partial}{\partial\beta}\left(\frac{1}{h}\frac{\partial\chi}{\partial\beta}\right)+\frac{1}{h^3}\frac{\partial h}{\partial\alpha}\frac{\partial\chi}{\partial\alpha},\\
\sigma_{\beta\beta} &= \frac{1}{h}\frac{\partial}{\partial\alpha}\left(\frac{1}{h}\frac{\partial\chi}{\partial\alpha}\right)+\frac{1}{h^3}\frac{\partial h}{\partial\beta}\frac{\partial\chi}{\partial\beta},\\
\sigma_{\alpha\beta} &= -\frac{1}{h^2}\left(\frac{\partial^2\chi}{\partial\alpha\partial\beta}-\frac{1}{h}\frac{\partial h}{\partial\beta}\frac{\partial\chi}{\partial\alpha}-\frac{1}{h}\frac{\partial h}{\partial\alpha}\frac{\partial\chi}{\partial\beta}\right)\\
&= -\frac{1}{2}\left[\frac{\partial}{\partial\alpha}\left(\frac{1}{h^2}\frac{\partial\chi}{\partial\beta}\right)+\frac{\partial}{\partial\beta}\left(\frac{1}{h^2}\frac{\partial\chi}{\partial\alpha}\right)\right].
\end{aligned} \tag{2.26}$$

or in terms of the relative displacement vector, from Eq. (2.9)

$$\begin{aligned}
\sigma_{\alpha\alpha} &= \frac{Y_2}{1-\sigma^2}\left(u_{\alpha\alpha}+\sigma u_{\beta\beta}\right),\\
\sigma_{\beta\beta} &= \frac{Y_2}{1-\sigma^2}\left(u_{\beta\beta}+\sigma u_{\alpha\alpha}\right),\\
2\sigma_{\alpha\beta} &= \frac{Y_2}{1+\sigma}u_{\alpha\beta}.
\end{aligned} \tag{2.27}$$

At first glance, it seems an insurmountable goal to solve the differential equations for the displacements in terms of the Airy stress function. However, following [50], they become much more tractable if one considers the terms

$$\begin{aligned}
\sigma_{\alpha\alpha}+\sigma_{\beta\beta} &= \frac{Y_2}{1-\sigma}\frac{1}{h^2}\left(\frac{\partial(hu_\alpha)}{\partial\alpha}+\frac{\partial(hu_\beta)}{\partial\beta}\right)\\
&= \frac{1}{h^2}\left(\frac{\partial^2\chi}{\partial\alpha^2}+\frac{\partial^2\chi}{\partial\beta^2}\right),
\end{aligned} \tag{2.28}$$

$$\begin{aligned}
\sigma_{\alpha\alpha}-\sigma_{\beta\beta} &= \frac{Y_2}{1+\sigma}\left(\frac{\partial}{\partial\alpha}\left(\frac{u_\alpha}{h}\right)-\frac{\partial}{\partial\beta}\left(\frac{u_\beta}{h}\right)\right)\\
&= -\frac{\partial}{\partial\alpha}\left(\frac{1}{h^2}\frac{\partial\chi}{\partial\alpha}\right)+\frac{\partial}{\partial\beta}\left(\frac{1}{h^2}\frac{\partial\chi}{\partial\beta}\right)
\end{aligned} \tag{2.29}$$

or, equivalently, we arrange equations to obtain,

$$\frac{\partial}{\partial\alpha}\left(\frac{\partial\chi}{\partial\alpha}-\frac{Y_2(hu_\alpha)}{1-\sigma}\right)+\frac{\partial}{\partial\beta}\left(\frac{\partial\chi}{\partial\beta}-\frac{Y_2(hu_\beta)}{1-\sigma}\right)=0, \tag{2.30}$$

from $\sigma_{\alpha\alpha}+\sigma_{\beta\beta}$ and $\sigma_{\alpha\alpha}-\sigma_{\beta\beta}$, respectively. There exists a function G which satisfies equation (2.30) for which $\frac{\partial G}{\partial\beta}=\frac{\partial\chi}{\partial\alpha}-\frac{Y_2}{1-\sigma}hu_\alpha$ and $\frac{\partial G}{\partial\alpha}=-\frac{\partial\chi}{\partial\beta}+\frac{Y_2}{1-\sigma}hu_\beta$. Using these

equations, we eliminate u_α and u_β from equation (2.29)

$$\frac{\partial^2}{\partial\alpha\partial\beta}\left(\frac{G}{h}\right) = -\frac{h}{1+\sigma}\left(\sigma_{\alpha\alpha}-\sigma_{\beta\beta}\right), \tag{2.31}$$

the left hand side of this equation may be written in this manner because $\frac{\partial^2}{\partial\alpha\partial\beta}\frac{1}{h}=0$. Thus, the relative displacement vectors are given by

$$\begin{aligned} u_\alpha &= \frac{1-\sigma}{Y_2}\frac{1}{h}\left(\frac{\partial\chi}{\partial\alpha}-\frac{\partial G}{\partial\beta}\right) \\ u_\beta &= \frac{1-\sigma}{Y_2}\frac{1}{h}\left(\frac{\partial\chi}{\partial\beta}+\frac{\partial G}{\partial\alpha}\right). \end{aligned} \tag{2.32}$$

Due to the nature of problems in the theory of linear elasticity theory, the most useful identities involve the directional cosines relating the $\{\alpha,\beta\}$ to the $\{x,y\}$ coordinates. The unit vectors in the new system are given by $\hat{\boldsymbol{\alpha}}=\frac{1}{h_\alpha}\left(\frac{\partial x}{\partial\alpha}\hat{\mathbf{x}}+\frac{\partial y}{\partial\alpha}\hat{\mathbf{y}}\right)$ and $\hat{\boldsymbol{\beta}}=\frac{1}{h_\beta}\left(\frac{\partial x}{\partial\beta}\hat{\mathbf{x}}+\frac{\partial y}{\partial\beta}\hat{\mathbf{y}}\right)$. The orthogonality condition $\hat{\boldsymbol{\alpha}}\cdot\hat{\boldsymbol{\beta}}=0$ implies $\frac{\partial x}{\partial\alpha}\frac{\partial x}{\partial\beta}+\frac{\partial y}{\partial\alpha}\frac{\partial y}{\partial\beta}=0$. The directional cosines are related because $h_\alpha^2=\left(\frac{\partial x}{\partial\alpha}\right)^2\left(1+\left(\frac{\partial y}{\partial\alpha}/\frac{\partial x}{\partial\alpha}\right)^2\right)=\left(\frac{\partial x}{\partial\alpha}\right)^2\left(1+\left(-\frac{\partial x}{\partial\beta}/\frac{\partial y}{\partial\beta}\right)^2\right)=h_\beta^2\left(\frac{\partial x}{\partial\alpha}\right)^2\left(\frac{\partial y}{\partial\beta}\right)^{-2}$, or

$$\frac{1}{h_\alpha}\frac{\partial x}{\partial\alpha}=\frac{1}{h_\beta}\frac{\partial y}{\partial\beta},\quad \frac{1}{h_\alpha}\frac{\partial y}{\partial\alpha}=-\frac{1}{h_\beta}\frac{\partial x}{\partial\beta}, \tag{2.33}$$

where the sign is chosen such that both $\{\hat{\mathbf{x}},\hat{\mathbf{y}},\hat{\mathbf{z}}\}$ and $\{\hat{\boldsymbol{\alpha}},\hat{\boldsymbol{\beta}},\hat{\mathbf{z}}\}$ form right-handed orthonormal triads. Thus, under the change of coordinates $\{x,y,z\}\to\{\alpha,\beta,z\}$, a rank-2 tensor $A_{ij}=a_{ij}\hat{\mathbf{x}}_i\hat{\mathbf{x}}_j$ transforms as $A_{\mu\nu}=a_{\mu\nu}\hat{\boldsymbol{\xi}}_\mu\hat{\boldsymbol{\xi}}_\mu=a_{ij}\left(\hat{\boldsymbol{\xi}}_\mu\cdot\hat{\mathbf{x}}_i\right)\hat{\boldsymbol{\xi}}_\mu\left(\hat{\boldsymbol{\xi}}_\nu\cdot\hat{\mathbf{x}}_j\right)\hat{\boldsymbol{\xi}}_\nu$, which may be written as

$$a_{\mu\nu}=\frac{1}{h_\mu h_\nu}\frac{\partial x_i}{\partial\xi_\mu}\frac{\partial x_j}{\partial\xi_\nu}a_{ij}. \tag{2.34}$$

The derivatives of the directional cosines can be made from linear combinations of derivatives of the orthogonality condition $\frac{\partial x}{\partial\alpha}\frac{\partial x}{\partial\beta}+\frac{\partial y}{\partial\alpha}\frac{\partial y}{\partial\beta}=0$ and the scale functions. For example, to find $\frac{\partial}{\partial\alpha}\left(\frac{1}{h_\alpha}\frac{\partial x}{\partial\alpha}\right)$, first note there are two ways of obtaining this derivative; directly,

$$\frac{\partial}{\partial\alpha}\left(\frac{1}{h_\alpha}\frac{\partial x}{\partial\alpha}\right)=-\frac{1}{h_\alpha^2}\frac{\partial h_\alpha}{\partial\alpha}\frac{\partial x}{\partial\alpha}+\frac{1}{h_\alpha}\frac{\partial^2 x}{\partial\alpha^2}, \tag{2.35}$$

and by taking the derivative of the product of α scale function and orthogonality condition

with respect to α

$$\begin{aligned}\frac{\partial}{\partial\alpha}\left(\frac{1}{h_\alpha}\frac{\partial x}{\partial\alpha}\right)\frac{\partial x}{\partial b} &= \frac{1}{h_\alpha}\left(\frac{1}{h_\alpha}\frac{\partial h_\alpha}{\partial\alpha}\frac{\partial y}{\partial\alpha}\frac{\partial y}{\partial\beta}-\frac{\partial^2 y}{\partial\alpha^2}\frac{\partial y}{\partial\beta}-\frac{\partial^2 x}{\partial\alpha\partial\beta}\frac{\partial x}{\partial\alpha}-\frac{\partial^2 y}{\partial\alpha\partial\beta}\frac{\partial y}{\partial\alpha}\right)\\ &= \frac{1}{h_\alpha^2}\frac{\partial h_\alpha}{\partial\alpha}\frac{\partial y}{\partial\alpha}\frac{\partial y}{\partial\beta}-\frac{1}{h_\alpha}\frac{\partial^2 y}{\partial\alpha^2}\frac{\partial y}{\partial\beta}-\frac{\partial h_\alpha}{\partial\beta},\end{aligned} \tag{2.36}$$

where we have made use of the definition $\frac{\partial h_\alpha}{\partial\beta}=\frac{\partial^2 x}{\partial\alpha\partial\beta}\frac{\partial x}{\partial\alpha}+\frac{\partial^2 y}{\partial\alpha\partial\beta}\frac{\partial y}{\partial\alpha}$. Next multiplying Eqn. 2.35 by $\frac{\partial x}{\partial\beta}$ and Eqn. 2.36 by $\left(\frac{\partial y}{\partial\beta}\right)^2$ and taking their sum, this becomes

$$\begin{aligned}h_\beta^2\frac{\partial}{\partial\alpha}\left(\frac{1}{h_\alpha}\frac{\partial x}{\partial\alpha}\right) &= \frac{1}{h_\alpha^2}\frac{\partial h_\alpha}{\partial\alpha}\frac{\partial y}{\partial\beta}\left(\frac{\partial y}{\partial\alpha}\frac{\partial x}{\partial\beta}-\frac{\partial y}{\partial\beta}\frac{\partial x}{\partial\alpha}\right)-\frac{\partial h_\alpha}{\partial\beta}\frac{\partial x}{\partial\beta}\\ &+ \frac{1}{h_\alpha^2}\frac{\partial y}{\partial\beta}\left(\frac{\partial y}{\partial\beta}\frac{\partial^2 x}{\partial\alpha^2}-\frac{\partial x}{\partial\beta}\frac{\partial^2 y}{\partial\alpha^2}\right)\\ &= \frac{1}{h_\alpha^2}\frac{\partial h_\alpha}{\partial\alpha}\frac{\partial y}{\partial\beta}\frac{h_\beta}{h_\alpha}-\frac{\partial h_\alpha}{\partial\beta}\frac{\partial x}{\partial\beta}-\frac{1}{h_\alpha}\frac{\partial y}{\partial\beta}\frac{h_\beta}{h_\alpha}\frac{\partial h_\alpha}{\partial\alpha}.\end{aligned} \tag{2.37}$$

By following a the same procedure, the formulæ for the derivatives of the directional cosines are

$$\begin{aligned}\frac{\partial}{\partial\alpha}\left(\frac{1}{h_\alpha}\frac{\partial x_i}{\partial\alpha}\right) &= -\frac{1}{h_\beta^2}\frac{\partial h_\alpha}{\partial\beta}\frac{\partial x_i}{\partial\beta},\quad \frac{\partial}{\partial\beta}\left(\frac{1}{h_\alpha}\frac{\partial x_i}{\partial\alpha}\right)=\frac{1}{h_\alpha h_\beta}\frac{\partial h_\beta}{\partial\alpha}\frac{\partial x_i}{\partial\beta},\\ \frac{\partial}{\partial\alpha}\left(\frac{1}{h_\beta}\frac{\partial x_i}{\partial\beta}\right) &= \frac{1}{h_\alpha h_\beta}\frac{\partial h_\alpha}{\partial\beta}\frac{\partial x_i}{\partial\alpha},\quad \frac{\partial}{\partial\beta}\left(\frac{1}{h_\beta}\frac{\partial x_i}{\partial\beta}\right)=-\frac{1}{h_\alpha^2}\frac{\partial h_\beta}{\partial\alpha}\frac{\partial x_i}{\partial\alpha},\end{aligned} \tag{2.38}$$

where $i=1,2$ and $x_1=x$ and $x_2=y$. Note that the cross partial derivatives of the directional cosines are equal,

$$\begin{aligned}\frac{\partial}{\partial\beta}\left(\frac{\partial}{\partial\alpha}\left(\frac{1}{h_\alpha}\frac{\partial x_i}{\partial\alpha}\right)\right)-\frac{\partial}{\partial\alpha}\left(\frac{\partial}{\partial\beta}\left(\frac{1}{h_\alpha}\frac{\partial x_i}{\partial\alpha}\right)\right) &= 0,\\ \frac{\partial}{\partial\beta}\left(\frac{\partial}{\partial\alpha}\left(\frac{1}{h_\beta}\frac{\partial x_i}{\partial\beta}\right)\right)-\frac{\partial}{\partial\alpha}\left(\frac{\partial}{\partial\beta}\left(\frac{1}{h_\beta}\frac{\partial x_i}{\partial\beta}\right)\right) &= 0,\end{aligned} \tag{2.39}$$

which leads to our final identity

$$\frac{\partial}{\partial\beta}\left(\frac{1}{h_\beta}\frac{\partial h_\alpha}{\partial\beta}\right)+\frac{\partial}{\partial\alpha}\left(\frac{1}{h_\alpha}\frac{\partial h_\beta}{\partial\alpha}\right)=0. \tag{2.40}$$

2.3 I'm Fixing a Hole

2.3.1 *I'm Fixing a Hole (Demo)*

The simplest system to study is an infinite elastic sheet with a circular hole, of radius R, cut in it under uniform tension $P\hat{\mathbf{x}}$. This problem naturally lends itself to polar coordinates,

for which the equations for the stress function become,

$$\begin{aligned}\sigma_{rr} &= \frac{1}{r}\frac{\partial\chi}{\partial r}+\frac{1}{r^2}\frac{\partial^2\chi}{\partial\phi^2}, \quad \sigma_{\phi\phi}=\frac{\partial^2\chi}{\partial\phi^2},\\ \sigma_{r\phi} &= -\frac{\partial}{\partial r}\left(\frac{1}{r}\frac{\partial\chi}{\partial\phi}\right).\end{aligned} \tag{2.41}$$

A standard procedure for solving such problems is to solve first for the deformation of a continuous sheet under the proper forces. Secondly, we solve a for a second stress function respecting the symmetry broken by the force with boundary conditions $\sigma_{ik}(r=\infty)=0$. The final stress function is given by the sum of the two stress functions, where the matching condition is given by the stress free boundary condition at the edge of the hole.

The components of the stress tensor for a continuous elastic sheet under uniform tension $P\hat{\mathbf{x}}$ are $\sigma^{(0)}_{xx}=P$ and $\sigma^{(0)}_{yy}=\sigma^{(0)}_{xy}=0$, which, by integrating Eqs. (2.19) yield the stress function

$$\chi^{(0)}=Py^2/2=Pr^2(\sin^2\phi)/2=Pr^2(1-\cos 2\phi)/4 \tag{2.42}$$

from which it follows that the components of the stress tensor are $\sigma^{(0)}_{rr}(r)=P(1+\cos 2\phi)/2$, $\sigma^{(0)}_{\phi\phi}(r)=P(1-\cos 2\phi)/2$, and $\sigma^{(0)}_{r\phi}(r)=P(\sin 2\phi)/2$. Clearly, rotational symmetry is broken in the $\hat{\mathbf{x}}$-direction.

In order for the second stress function to respect the broken symmetry of the system, it must have the form $\chi^{(1)}=f(r)+g(r)\cos 2\phi$. Since the stress function satisfies the biharmonic equation, we can easily integrate to find

$$\begin{aligned}f(r) &= ar^2\log r+br^2+c\log r\\ g(r) &= sr^2+tr^4+u/r^2+v\end{aligned} \tag{2.43}$$

The first boundary conditions $\sigma^{(1)}_{ik}(r=\infty)=0$ dictate that $a=b=s=t=0$, leaving

$$\begin{aligned}\sigma^{(1)}_{rr}(r) &= c/r^2-\left(6u/r^4+4v/r^2\right)\cos 2\phi\\ \sigma^{(1)}_{\phi\phi}(r) &= -c/r^2+6(u/r^4)\cos 2\phi\\ \sigma^{(1)}_{r\phi}(r) &= -\left(6u/r^4+4v/r^2\right)\sin 2\phi\end{aligned} \tag{2.44}$$

Using the final boundary conditions, $\sigma^{(1)}_{\mu\nu}(R)=-\sigma^{(0)}_{r\phi}(R)$ the remaining constants are found

to be $c = -PR^2/2$, $u = -PR^4/4$, and $v = PR^2/2$. Note that even though there are only two equations for three unknowns, this system is not underdetermined because the constant c cannot depend on ϕ. Assembling this, the components of the stress tensor are given by

$$\begin{aligned}
\sigma_{rr}(r) &= \frac{P}{2}\left[1 - \frac{R^2}{r^2} + \left(1 - \frac{4R^2}{r^2} + \frac{3R^4}{r^4}\right)\cos 2\phi\right], \\
\sigma_{\phi\phi}(r) &= \frac{P}{2}\left[1 + \frac{R^2}{r^2} - \left(1 + \frac{3R^4}{r^4}\right)\cos 2\phi\right] \\
\sigma_{r\phi}(r) &= -\frac{P}{2}\left(1 + \frac{2r^2}{r^2} - \frac{3R^4}{r^4}\right)\sin 2\phi.
\end{aligned} \tag{2.45}$$

which may be rewritten, using equation (2.10), as components of the strain tensor

$$\begin{aligned}
u_{rr} &= \frac{1}{Y_2}(\sigma_{rr} - \gamma\sigma_{\phi\phi}) \\
u_{\phi\phi} &= \frac{1}{Y_2}(\sigma_{\phi\phi} - \gamma\sigma_{rr}) \\
u_{r\phi} &= \frac{1+\gamma}{Y_2}\sigma_{r\phi}.
\end{aligned} \tag{2.46}$$

Recall, the strain tensor is the relative displacement of every element from its equilibrium position. In polar coordinates we have $u_{rr} = \partial u_r/\partial r$, $u_{\phi\phi} = (\partial u_\phi/\partial\phi)/r + u_r/r$, and $2u_{r\phi} = \partial u_\phi/\partial r + (\partial u_r/\partial\phi) - u_\phi/r$, from which it follows that the displacement vector is

$$\begin{aligned}
u_r &= \frac{P}{2Y_2}\left[(1-\gamma)r + \frac{(1+\gamma)R^2}{r} + \left((1+\gamma)\left(r - \frac{R^4}{r^3}\right) + \frac{4R^2}{r}\right)\cos 2\phi\right] \\
u_\phi &= -\frac{P}{2Y_2}\frac{(R^2+r^2)^2 + \gamma(R^2-r^2)^2}{r^3}\sin 2\phi.
\end{aligned} \tag{2.47}$$

However, if we repeat the above process for an infinite sheet under hydrostatic compression (or expansion), to linear order the rotational symmetry of this system is not broken. Consider an annulus of inner radius R_0 and outer radius R_1 under uniform hydrostatic compression with boundary conditions given by $\sigma^{(0)}_{rr} = -P$ and $\sigma^{(0)}_{\phi\phi} = \sigma^{(0)}_{r\phi} = 0$. Clearly, the displacements are purely radial, and we need only solve $\nabla^4\mathbf{u} = 0$, subject to the boundary conditions $\sigma_{rr}(r = R_1) = -P$ and $\sigma_{rr}(r = R_0) = 0$. The displacements are given by $u_r(r) = a/r + br$; from which it follows $\sigma_{rr} = \frac{Y_2}{1-\gamma^2}\left[-(1-\gamma)a/r^2 + (1+\gamma)b\right]$. The boundary conditions determine the values of the constants $a = -\frac{P}{Y_2}(1+\gamma)\frac{R_0^2R_1^2}{R_1^2-R_0^2}$ and

$b = -\frac{P}{Y_2}(1-\gamma)\frac{R_1^2}{R_1^2-R_0^2}$. The solution to an annulus under hydrostatic compression is

$$u_r(r) = \frac{P}{Y_2}\frac{R_1^2}{R_1^2 - R_0^2}\left((1+\gamma)\frac{R_0^2}{r} + (1-\gamma)r\right), \tag{2.48}$$

with the components of the stress tensor given by

$$\begin{aligned}
\sigma_{rr}(r) &= -P\frac{R_1^2}{R_1^2+R_0^2}\frac{r^2-R_0^2}{r^2} \\
\sigma_{\phi\phi}(r) &= -P\frac{R_1^2}{R_1^2+R_0^2}\frac{r^2+R_0^2}{r^2} \\
\sigma_{r\phi}(r) &= 0.
\end{aligned} \tag{2.49}$$

In the case of a finite sheet or a pipe under hydrostatic compression, there is the well known von Mises buckling instability at a critical pressure where the circular hole deforms into an ellipse whose major axis is chosen at random [100]. This critical pressure scales with the ratio of the system size to the hole radius and, thus, diverges for large systems. The system we are studying, on the other hand, has an underlying lattice which breaks the rotational symmetry of each hole. A superposition of the above solutions would not account for the interaction between holes.

2.3.2 *I'm Fixing a Hole (Take 2)*

Understanding the elastic interaction between holes in an elastic sheet was, during the first half of the last century, the subject of much research [50, 47, 48, 38, 95, 66]. Most of which was dedicated to finding the maximum stress felt along the perimeter of each hole. While linear elasticity may provide reasonable solutions to such analysis, we will demonstrate that linear theory breaks down upon further investigation.

The simplest system accounting for the interaction between holes is an infinite elastic sheet containing two holes of radius R, whose centers are separated by distance $2d$. This sheet is then subjected to uniform tension P. The analysis of this system will closely follow that of Ling [66]. Bipolar coordinates, defined by

$$x = \frac{a\sinh\alpha}{\cosh\alpha - \cos\beta}, \quad y = \frac{a\sin\beta}{\cosh\alpha - \cos\beta}, \tag{2.50}$$

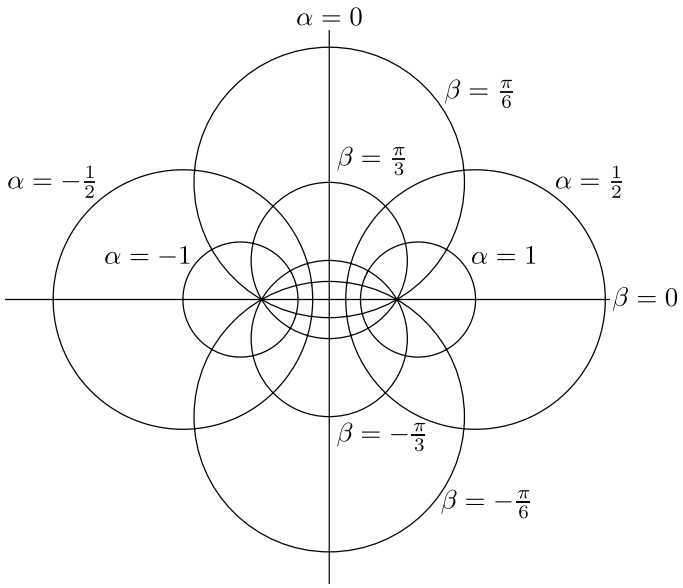

Figure 2.2: Curves of constant α and β are circles in bipolar coordinates.

for $\beta \in [0, 2\pi), \alpha \in (-\infty, \infty)$, are the natural choice for this problem, as lines of constant α or β are circles in the xy-plane defined by $x^2+(y-a\cot\beta)^2 = a^2\csc^2\beta$ and $(x-a\coth\alpha)^2+y^2 = a^2\mathrm{csch}^2\alpha$. The system of two equal holes corresponds to $\alpha = \pm s$, $s = \cosh^{-1}(d/R)$, and $a^2 = d^2 - R^2$. When the system is under uniform tension P, the components of the stress tensor are $\sigma_{xx} = P$, $\sigma_{yy} = P$, and $\sigma_{xy} = 0$. By integrating the Eqs. (2.19), the stress function for an infinite system under uniform tension is

$$\chi^{(0)} = \frac{P}{2}(x^2 + y^2) = \frac{Pa^2}{2}\frac{\cosh\alpha + \cos\beta}{\cosh\alpha - \cos\beta}. \tag{2.51}$$

Using the method outlined in the previous section, we undertake the tedious calculation, detailed in section 2.2.2, to find the equilibrium configuration of this system. The results for uniform compression and tension are displayed in Figure 2.3. Upon further analysis of the compressed system, large enough values of P yield overlapping solutions for the displacement vectors, signaling the breakdown of the linear theory.

Recall, χ is the solution to the biharmonic equation $\nabla^4\chi = 0$ with respect to the symmetries in our system. The biharmonic equation when written in terms of the function

χ/h has the simplified form,

$$\left(\frac{\partial^4}{\partial\alpha^4}+\frac{\partial^4}{\partial\beta^4}+2\frac{\partial^4}{\partial\alpha^2\partial\beta^2}-2\frac{\partial^2}{\partial\alpha^2}+2\frac{\partial^2}{\partial\beta^2}+1\right)\frac{\chi}{h}=0. \tag{2.52}$$

Similarly, the components of the stress tensor are given by,

$$\begin{aligned}
\sigma_{\alpha\alpha} &= \left[\frac{1}{h}\frac{\partial^2}{\partial\beta^2}-\frac{\sinh\alpha}{a}\frac{\partial}{\partial\alpha}-\frac{\sin\beta}{a}\frac{\partial}{\partial\beta}+\frac{\cosh\alpha}{a}\right]\frac{\chi}{h}\\
\sigma_{\beta\beta} &= \left[\frac{1}{h}\frac{\partial^2}{\partial\alpha^2}-\frac{\sinh\alpha}{a}\frac{\partial}{\partial\alpha}-\frac{\sin\beta}{a}\frac{\partial}{\partial\beta}+\frac{\cos\beta}{a}\right]\frac{\chi}{h}\\
\sigma_{\alpha\beta} &= -\frac{1}{h}\frac{\partial^2}{\partial\alpha\partial\beta}\left(\frac{\chi}{h}\right).
\end{aligned} \tag{2.53}$$

Our system, while undergoing uniform hydrostatic compression, is described by the stress function in equation (2.51),

$$\frac{\chi^{(0)}}{h}=\frac{Pa}{2}\left(\cosh\alpha+\cos\beta\right),$$

or, equivalently, is given by the components of the stress tensor

$$\sigma^{(0)}_{\alpha\alpha}=\sigma^{(0)}_{\beta\beta}=P,\quad \sigma^{(0)}_{\alpha\beta}=0. \tag{2.54}$$

We aim to find solutions to the biharmonic equation that are even in both α and β. Thus, the Airy stress function is given by

$$\frac{\chi^{(1)}}{h} = C\left(\cosh\alpha-\cos\beta\right)\log\left(\cosh\alpha-\cos\beta\right)+\sum_{n=1}^{\infty}\phi_n(\alpha)\cos n\beta, \tag{2.55}$$

where $\phi_n(\alpha)=A_n\cosh(n+1)\alpha+B_n\cosh(n-1)\alpha$. The components of the stress tensor

corresponding to this Airy stress function are

$$\begin{aligned}
\sigma^{(1)}_{\alpha\alpha} &= -\frac{C}{2a}\left(\cosh 2\alpha - 2\cosh\alpha\cos\beta + \cos 2\beta\right) + \frac{1}{a}\phi_1(\alpha) \\
&\quad + \frac{1}{2a}\sum_{n=1}^{\infty}\frac{1}{n}\left[f_{n+1}(\alpha) - 2\cosh\alpha f_n(\alpha) + f_{n-1}(\alpha) - 2\sinh\alpha g_n(\alpha)\right]\cos n\beta \qquad (2.56) \\
\sigma^{(1)}_{\beta\beta} &= \frac{C}{2a}\left(\cosh 2\alpha - 2\cosh\alpha\cos\beta + \cos 2\beta\right) + \frac{1}{a}\phi_1(\alpha) - \frac{1}{2a}\phi_1''(\alpha) \\
&\quad - \sum_{n=1}^{\infty}\left[\phi''_{n+1}(\alpha) - 2\cosh\alpha\phi''_n(\alpha) + \phi''_{n-1}(\alpha) + (n+2)\phi_{n+1}(\alpha)\right. \\
&\quad \left. + 2\sinh\alpha\phi'_n(\alpha) + (n-2)\phi_{n-1}(\alpha)\right]\cos n\beta \qquad (2.57) \\
\sigma^{(1)}_{\alpha\beta} &= -\frac{C}{a}\sinh\alpha\sin\beta - \frac{1}{2a}\sum_{n=1}^{\infty}\left[g_{n+1}(a) - 2\cosh\alpha g_n(\alpha) + g_{n-1}(\alpha)\right]\sin n\beta, \qquad (2.58)
\end{aligned}$$

where $f_n(\alpha) = (n+1)n(n-1)\phi_n(\alpha)$ and $g_n(\alpha) = n\phi'_n(\alpha)$. The boundary conditions require there be no stress at infinity ($\alpha = 0$), hence

$$\sum_{n=1}^{\infty}\left[A_n + B_n\right] = 0, \qquad (2.59)$$

and the normal and tangential stresses must vanish along the edges of the holes, located at $\alpha = \pm s$. Thus, the constants A_n, B_n and C must satisfy the following recurrence relations for $n \geq 2$

$$\begin{aligned}
f_{n+1}(s) - 2\cosh s f_n(s) + f_{n-1}(s) &= 2\sinh s g_n(s), \qquad (2.60) \\
g_{n+1}(s) - 2\cosh s g_n(s) + g_{n-1}(s) &= 0, \qquad (2.61)
\end{aligned}$$

subject to the conditions

$$\begin{aligned}
2\phi_1(s) &= -2\frac{P}{a} - C\cosh 2s, \qquad (2.62) \\
f_2(s) - 2\sinh s g_1(s) &= 2\cosh s, \qquad (2.63) \\
s - 2\cosh s f_2(s) + f_3(s) &= 2\sinh s g_2(s) + 2C, \qquad (2.64) \\
2\cosh s g_1(s) - g_2(s) &= 2C\sinh s. \qquad (2.65)
\end{aligned}$$

Using equation (2.61), we find $g_n(s) = c_1\lambda_1^n + c_2\lambda_2^n$, where λ_1 and λ_2 are roots of the characteristic polynomial $t^{n+1} - 2\cosh s t^n + t^{n-1} = 0$, yielding $g_n(s) = c_1 e^{-ns} + c_2 e^{ns}$. However, the stress must be finite everywhere, thus, $c_2 = 0$. Equation (2.65) completes the relation

for $g_n(s)$ as $c_1 = 2C\sinh s$. Because, equation (2.60) is a non-linear recurrence relation, we must consider $f_{n+2} - 2\cosh s f_{n+1} s + f_n s - \frac{g_{n+1}}{g_n}\left(f_{n+1}(s) - 2\cosh s f_n(s) + f_{n-1}(s)\right) = 0$. Two of the roots of the characteristic polynomial for this equation are degenerate, the equation is $f_n(s) = d_1 e^{-ns} + d_2 n e^{-ns} + d_3 e^{ns}$. From the boundary conditions, we determine $f_n(s) = -2K\left(\cosh s + n\sinh s\right)e^{-ns}$. From the definitions of $f_n(\alpha)$ and $g_n(\alpha)$, we find that the coefficients A_n, B_n and C satsify,

$$\begin{aligned} A_n &= 2C\frac{e^{-ns}\sinh ns + ne^{-s}\sinh s}{n(n+1)\left(\sinh 2ns + n\sinh 2s\right)}, \\ B_n &= -2C\frac{e^{-ns}\sinh ns + ne^{s}\sinh s}{n(n-1)\left(\sinh 2ns + n\sinh 2s\right)}, \\ &\text{with} \quad B_1 = \frac{C}{2}\tanh s\cosh 2s + P, \end{aligned} \tag{2.66}$$

and

$$C = -P\left\{\frac{1}{2} + \tanh s\sinh^2 s - 4\sum_{n=2}^{\infty}\left[\frac{e^{-ns}\sinh ns + n\sinh s\left(n\sinh s + \cosh s\right)}{n(n^2-1)\left(\sinh 2ns + n\sinh 2s\right)}\right]\right\}^{-1}. \tag{2.67}$$

Now that we have equations for the stresses everywhere, we may now solve for the field of relative displacement vectors. Recall, our function G is given by,

$$\frac{\partial\chi}{\partial\alpha} = h\left(\sinh\alpha(-Ph\cos\beta + C) - \sum_{n=1}^{\infty}\left[\frac{h}{a}\phi_n(\alpha)\sinh\alpha - \phi_n'(\alpha)\right]\cos n\beta\right) \tag{2.68}$$

$$\frac{\partial\chi}{\partial\beta} = h\left(\sin\beta(-Ph\cosh\alpha + C) - \sum_{n=1}^{\infty}\phi_n(\alpha)\left[\frac{h}{a}\sin\beta\cos n\beta + n\sin n\beta\right]\right) \tag{2.69}$$

$$\frac{\partial G}{\partial\alpha} = -\frac{2h}{1+\sigma}\left(C\left(\pi\frac{h}{a}\sinh\alpha\cos\beta + \sin\beta\right) + \sum_{n=1}^{\infty}\left[\frac{h}{a}\psi_n(\alpha)\sinh\alpha - \psi_n'(\alpha)\right]\sin n\beta\right) \tag{2.70}$$

$$\frac{\partial G}{\partial\beta} = -\frac{2h}{1+\sigma}\left(C\left(\pi\frac{h}{a}\cosh\alpha\sin\beta - \sinh\alpha\right) + \sum_{n=1}^{\infty}\psi_n(\alpha)\left[\frac{h}{a}\sin\beta\sin n\beta - n\cos n\beta\right]\right). \tag{2.71}$$

These equations, together with Eqs. (2.32), complete our description of the system of two holes under hydrostatic compression, which may be seen in Fig. 2.3. It should be noted that in the compressed system there is an instability for large enough values of P wherein

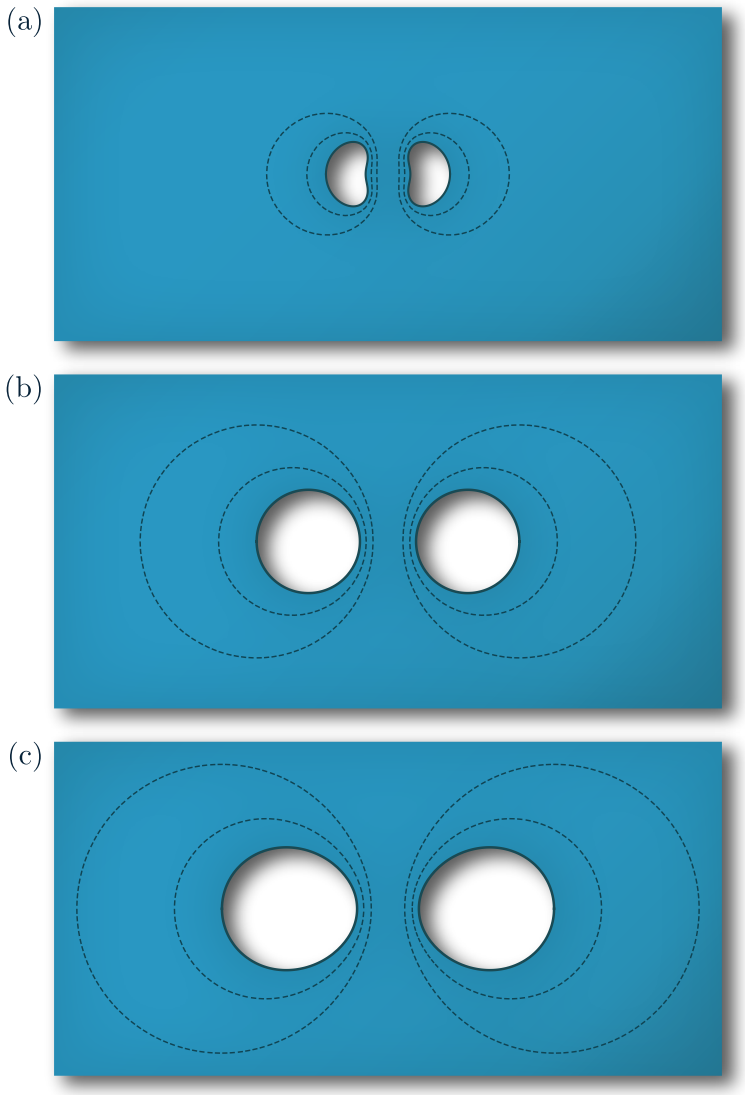

Figure 2.3: An elastic sheet with two circular holes cut out (a) is subjected to uniform tension (b) and compression (c). The dark blue curves are the the boundary of the holes. The other curves show deformations of the circles in (a) to aid the eye.

the displacements intersect each other, causing overlap in the system.

Chapter 3

In Which Dislocation Dipoles Interact and a Diamond Plate Emerges

3.1 The Linear Theory of Nonlinear Elasticity

Even were there no instability in the linear theory of two elastic holes, the sheer complexity of the equations would make analytic calculations of increasing numbers of holes a nearly impossible task, and understanding the mechanism by which the holes collapse and the shapes they form requires a nonlinear theory of elasticity. Thus, we turn to the theory of cracks for inspiration. In the linear theory of elasticity, cracks can be described by a continuous distribution of parallel dislocations [63, 44]. The stresses in a body due to a crack are the same as the stresses in an isotropic body with a distribution of dislocations with the same height profile as that of the crack. As a first approximation, we model each of the collapsed holes as a pair of oppositely charged dislocations, known as a dislocation dipole [17]. This formalism allows us to recover the same physics by the simple numerical minimization of algebraic equations, once described by a complex system of coupled differential equations.

In continuum elasticity theory, a dislocation dipole models an infinitesimally thin bit of material inserted into (or removed from) the bulk medium in along the dipole vector $\mathbf{d}_i(\mathbf{x})$. This causes relatively large displacements in the immediate vicinity of the dislocation, which rapidly relax. However the effects of such a deformation are felt far away from the dislocation. Consider any closed contour γ which surrounds one end of the dislocation dipole. As this circuit is traversed, the displacement vector changes incrementally by the Burgers vector $\mathbf{b}$, a finite amount given by $b_i = -\oint_\gamma du_i = -\oint_\gamma \frac{\partial u_i}{\partial x_k} dx_k$. [63] A dislocation dipole connects a pair of antiparallel Burgers vectors of the same magnitude.

In our system, the elastic sheet itself can be accurately modeled by linear elasticity

theory; however, the free boundaries of the holes do not. Thus, we consider the stresses in the system not to be caused by the details of the deformation at the boundary, but by vacancies described by dislocation dipoles whose centers coincide with the centers of the original holes. Such deformations in continuum systems are more readily described by a continuous distribution of dislocations denoted by the tensor ρ_{ik}. As more parallel dislocations are added, their profile begins to form the outline of a macroscopic vacancy (or inclusion), $h_i(\mathbf{x}) = \int^{\mathbf{x}} \rho_{ik} dx_k$.

3.1.1 The Theory of Dislocations

The notion of topological defects is most easily demonstrated by considering crystals. Let us consider a two dimensional square lattice, with equilibrium positions defined by $\mathbf{u} = (m + 1/2)a\hat{\mathbf{x}} + na\hat{\mathbf{y}}$, $\forall m, n \in \mathbb{Z}$, where a is the lattice spacing. Now, we add extra row of points along the y-axis, $\delta\mathbf{u} = -na\delta(x)\hat{\mathbf{y}}$, $n \geq 0$, and allow the system to elastically relax. Far away from the defect, the line integral around a closed circuit of lattice points enclosing the defect is not zero, but $\oint d\mathbf{u} = -a\hat{\mathbf{x}}$. Every dislocation can be described by a Burgers vector $\mathbf{b}$, a constant vector which measures the elastic displacement caused by a defect and is defined by the line integral around the defect core, $b_i = \oint du_i = \oint \frac{\partial u_i}{\partial x_k} dx_k$. When the Burgers vector is perpendicular to the axis of the line integral, as in our example, the is known as an "edge dislocation." When the two vectors are parallel, the defect is a "screw dislocation."

The Burgers vector formalism extends beyond the simple case of crystals to isotropic bodies. We follow Ref. [17] to derive the energy of a distribution of defects. It is often more convenient to deal with the tensor $w_{ik} = \partial u_i / \partial x_k$ when dealing with the energetics of dislocations. By Stokes' theorem, $\oint dx_k w_{ik} = \oint d^2x \epsilon_{lk} \partial w_{ik} / \partial x_l = \sum_n b_{in}(\mathbf{x})$, where $b_i = \epsilon_{lk} \partial w_{ik} / \partial x_l$ is the dislocation density. To calculate the energy of a distribution of dislocations, we relate this description involving w_{ik} to the Airy stress function. Recall the stress tensor is given by $\sigma_{ik} = \epsilon_{ij}\epsilon_{kl}\partial^2\chi/(\partial x_j \partial x_l)$. We can express the strain tensor, and therefore the energy as $u_{ik} = \big((1+\sigma)\sigma_{ik} - \sigma\delta_{ik}\sigma_{ll}\big)/Y_2 = \big((1+\sigma)\epsilon_{ij}\epsilon_{kl}\partial^2\chi/(\partial x_j \partial x_l) - \sigma\delta_{ik}\nabla^2\chi\big)/Y_2$. Similarly the strain tensor may be separated into continuous and singular

components, $u_{ik} = (w_k i - w_i k)/2 + w_i k$. By applying the operator $\epsilon_{ij}\epsilon_{kl}\partial^2/(\partial x_j \partial x_l)$ to both definitions of u_{ik}, we find that

$$\begin{aligned} \frac{1}{Y_2}\nabla^4\chi &= \frac{1}{2}\epsilon_{ij}\epsilon_{kl}\frac{\partial^2}{\partial x_j \partial x_l}(w_{ki} - w_{ik}) + \epsilon_{ij}\epsilon_{kl}\frac{\partial^2 w_{ik}}{\partial x_j \partial x_l} \\ &= -\frac{1}{2}\left(\epsilon_{ij}\frac{\partial b_i}{\partial x_j} - \epsilon_{kl}\frac{\partial b_k}{\partial x_l}\right) - \epsilon_{ij}\frac{\partial b_i}{\partial x_j}. \end{aligned} \tag{3.1}$$

We now plug this into the energy functional, $E = \frac{1}{2}\int d^2x \sigma_{ik} u_{ik}$,

$$E = \frac{1}{2Y_2}\int d^2x \left[\left(\nabla^2\chi\right)^2 + 2\left(1+\sigma\right)\epsilon_{ij}\epsilon_{kl}\frac{\partial^2}{\partial x_j \partial x_l}\left(\frac{\partial\chi}{\partial x_i}\frac{\partial\chi}{\partial x_l}\right)\right]. \tag{3.2}$$

However, the second term is a boundary term which integrates to zero if the system has no net dislocation charge. Thus, in Fourier space, the contribution to the energy from the dislocations is given by

$$E = \frac{Y_2}{2}\int \frac{d^2q}{(2\pi)^2}\frac{\delta_{ik} - \hat{q}_i\hat{q}_k}{q^2} b_i(q) b_k(-q). \tag{3.3}$$

3.2 I'm Filling a Crack

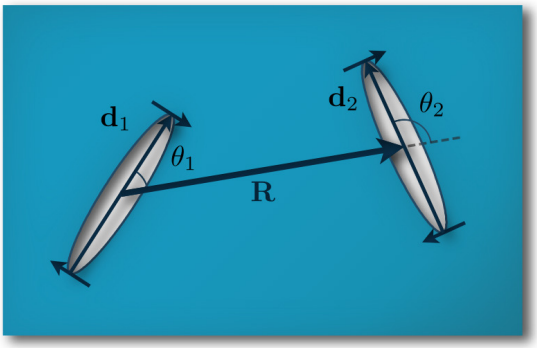

Figure 3.1: Two dipoles of strengths $\mathbf{d}_1$ and $\mathbf{d}_2$ are separated by $\mathbf{R}$.

Our model system consists of an isotropic solid where each collapsed hole is represented by a thin line of material that has been taken out of the system, or a dislocation dipole. The Burgers vector for a dislocation dipole of strength b with dipole vector $\mathbf{d}$ located at $\mathbf{r}$ is

$$\mathbf{b}\left(\mathbf{x}\right) = \hat{\mathbf{z}} \times \hat{\mathbf{d}}\, b\left[-\delta^2\left(\mathbf{x} - \frac{\mathbf{d}}{2} - \mathbf{r}\right) + \delta^2\left(\mathbf{x} + \frac{\mathbf{d}}{2} - \mathbf{r}\right)\right], \tag{3.4}$$

or in Fourier space,

$$\begin{aligned}\mathbf{b}\,(\mathbf{q}) &= 2ib\hat{\mathbf{z}}\times\hat{\mathbf{d}}\,e^{iqr\cos\theta}\sin\left[\frac{qd}{2}\cos(\theta-\theta_0)\right]\\ &\approx ibq\hat{\mathbf{z}}\times\mathbf{d}\,e^{iqr\cos\theta}\cos(\theta-\theta_0).\end{aligned}\tag{3.5}$$

where θ is angle of $\mathbf{q}$ and θ_0 is the direction of the dipole with respect to the $\mathbf{r}$-axis and we have, in the spirit of the dipole approximation, taken the lowest order term in $d=|\mathbf{d}|$.

The interaction energy between two dipoles $\mathbf{d}_1 = iqb(\hat{\mathbf{z}}\times\mathbf{d}_1)\cos(\theta-\theta_1)$ located at the origin and $\mathbf{d}_2 = iqb(\hat{\mathbf{z}}\times\mathbf{d}_2)e^{iqR\cos\theta}\cos(\theta-\theta_2)$ located at $\mathbf{R}$ is given by

$$E=\frac{Y_2b^2}{(2\pi)^2}\int d^2q\frac{\big[\mathbf{q}\times(\hat{\mathbf{z}}\times\mathbf{d}_1)\big]\cdot\big[\mathbf{q}\times(\hat{\mathbf{z}}\times\mathbf{d}_2)\big]}{q^4}\big(iq\cos(\theta-\theta_1)\big)\Big(-iqe^{-iqR\cos\theta}\cos(\theta-\theta_2)\Big).$$

$$=\frac{Y_2b^2d_1d_2}{(2\pi)^2}\int_0^\infty q\,dq\int_0^{2\pi}d\theta\,\cos\big(-q\,R\,\cos(\theta)\big)\cos^2(\theta-\theta_1)\cos^2(\theta-\theta_2),\tag{3.6}$$

This integral becomes tractable by first expanding the trigonometric functions in the integrand, $\cos^2(\theta-\theta_1)\cos^2(\theta-\theta_2)=\frac{1}{8}\big(1+2\cos\theta_-+4\cos2\theta\cos\theta_+\cos\theta_-+4\sin2\theta\sin\theta_+\cos\theta_-+\cos4\theta\cos2\theta_++\sin4\theta\sin2\theta_+\big)$, where $\theta_+=\theta_1+\theta_2$ and $\theta_-=\theta_1-\theta_2$, and secondly by recalling the Bessel function definition, $\int_0^{2\pi}dt\cos(nt)\cos\big(z\cos(t)\big)=2\pi i^nJ_n(z)$. Due to symmetry, the terms with $\sin n\theta$ are identically zero, leaving three terms contributing to the θ integral,

$$E=\frac{Y_2b^2d_1d_2}{16\pi}\int_0^\infty q\Big(J_0(qR)(1+2\cos\theta_-)-4J_2(qR)\cos\theta_+\cos\theta_-+J_4(qR)\cos2\theta_+\Big).\tag{3.7}$$

Finally employing the Bessel function identity, $\int_0^\infty z^{m-1}J_n(z)=\frac{2^{m-1}}{\Gamma\left(\frac{2-m+n}{2}\right)}\Gamma\left(\frac{m+n}{2}\right)$, allows us to complete the integral. The interaction energy between two dislocation dipoles is

$$E=-\frac{Y_2}{\pi}\frac{b^2\,d_1\,d_2}{R^2}\left(\cos(\theta_1+\theta_2)\sin\theta_1\sin\theta_2+\frac{1}{4}\right).\tag{3.8}$$

The angular dependence of the pairwise dipole interaction, shown in Figure 3.2, favors $\theta_1=\theta_2=\frac{\pi}{6}$. Note that the interaction energy is invariant under $\theta_1\to\theta_1+\pi$ and $\theta_2\to\theta_2+\pi$, which reaffirms each collapsed hole is represented by a line, not a vector. The total interaction energy of an array of dislocation dipoles is merely a sum of all pairwise interactions, because we are using linear theory. The centers of the initial holes set the position of each dislocation dipole, but they are allowed to rotate freely. The equilibrium

state minimizes the free energy over the angle each dipole makes with respect to a fixed axis.

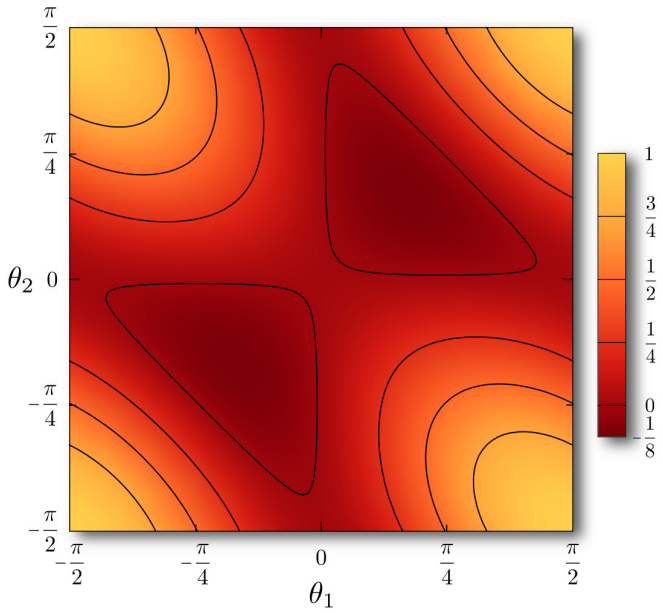

Figure 3.2: A contour plot of the angular dependence of the interaction energy, Eq. (3.8), between two dislocation dipoles.

The 2×2 Diamond Plate Plaquette

The simplest case consists of four holes located at $\{\pm a/2, \pm a/2\}$. Because all four holes have the same radius, their dipole vectors should have the same magnitude. We minimize the energy functional, composed of the sum of six pairwise terms,

$$\begin{aligned} E_{2\times 2} &= -\frac{Y_2 b^2 d^2}{\pi a^2}\left[\cos(\theta_1+\theta_2)\sin\theta_1\sin\theta_2+\cos(\theta_3+\theta_4)\sin\theta_3\sin\theta_4\right. \\ &+ \cos(\theta_1+\theta_3-\pi)\sin(\theta_1-\tfrac{\pi}{2})\sin(\theta_3-\tfrac{\pi}{2}) \\ &+ \cos(\theta_2+\theta_4-\pi)\sin(\theta_2-\tfrac{\pi}{2})\sin(\theta_4-\tfrac{\pi}{2}) \\ &+ \tfrac{1}{2}\cos(\theta_1+\theta_4-\tfrac{\pi}{2})\sin(\theta_1-\tfrac{\pi}{4})\sin(\theta_4-\tfrac{\pi}{4}) \\ &+ \left.\tfrac{1}{2}\cos(\theta_2+\theta_3-\tfrac{3\pi}{2})\sin(\theta_2-\tfrac{3\pi}{4})\sin(\theta_3-\tfrac{3\pi}{4})\right], \end{aligned} \tag{3.9}$$

over each of the angles, which are measured with respect to the x-axis. Minimizing with respect to the four angles we find $\theta_1 = \theta_4$ and $\theta_2 = \theta_3$ by symmetry and

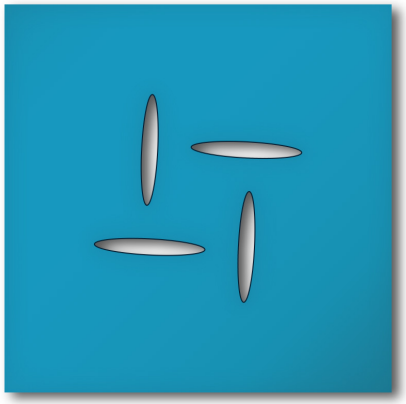

Figure 3.3: The groundstate orientation of the 2×2 plaquette.

$$\begin{aligned} \sin 4\theta_1 - \cos 2\theta_1 - 4\sin 2(\theta_1 + \theta_2) &= 0 \\ \sin 4\theta_2 + \cos 2\theta_2 - 4\sin 2(\theta_1 + \theta_2) &= 0. \end{aligned} \tag{3.10}$$

The minimum is

$$\theta_1 = \frac{1}{2}\sin^{-1}\left(\frac{1}{10}\right) = \theta_2 - \frac{\pi}{2}. \tag{3.11}$$

While one might have postulated that the lowest energy configuration would have $\theta_1 = 0$ and $\theta_2 = \pi/2$, it turns out that the energy is slightly lowered if these angles are slightly shifted. This is due to the finite size of our system – as we shall see, for larger systems the dipoles align along the crystal axes and there is a boundary effect which distorts the dipole directions at the edges.

3.2.1 We Had to Count Them All

One might wonder how we can study larger and larger systems since the interaction only falls off as $1/R^2$. Because the interactions is between dipoles, the interaction energy at large distances decreases because the angle of the dipoles rotates around the circle. Indeed, consider the interaction of a single dipole at the origin with $N^2 - 1$ other dipoles in an $Na \times Na$ lattice. The angular dependence in (3.8) will wash out the power law if the dipoles rotate through 2π uniformly. As we will see in the next section, this is precisely

what happens as shown in Fig. 3.4.

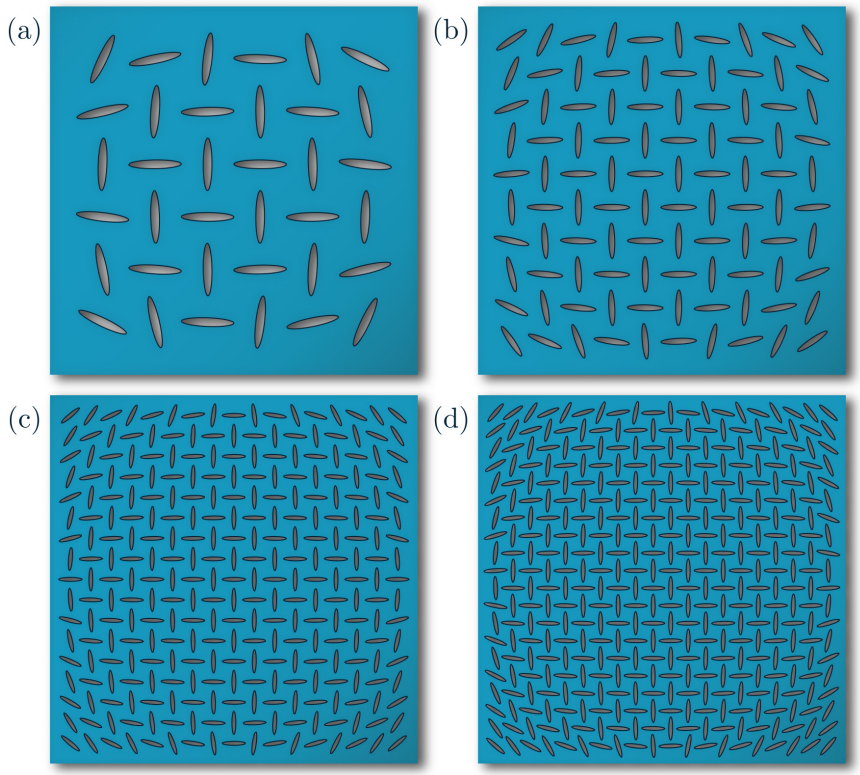

Figure 3.4: The groundstate orientations for square lattices of 6×6 (a), 10×10 (b), 17×17 (c), and 20×20 (d).

For these larger arrays of holes, the sheer number of coupled equations makes it impractical to find solutions by hand, and we use Mathematica to solve the many coupled nonlinear equations. We find the orientations of the ground state of each lattice. We find that the diamond plate order of the 2×2 plaquette persists for larger and larger samples with increasing alignment along the lattice directions.

It might seem counterintuitive that a diamond plate lattice forms from an interaction that favors both dipoles to be at angle $\pi/6$ with respect to the vector connecting them, and, indeed, a diamond plate texture is not the only texture to form. $M \times N$ lattices where $M \gg N$ demonstrate the diamond plate pattern to be a result of the boundary. The regions near the beginning and end of the lattice are dominated by a diamond plate pattern. However, the region in the center consists primarily of dipoles at angle $\theta \sim \frac{\pi}{6}$.

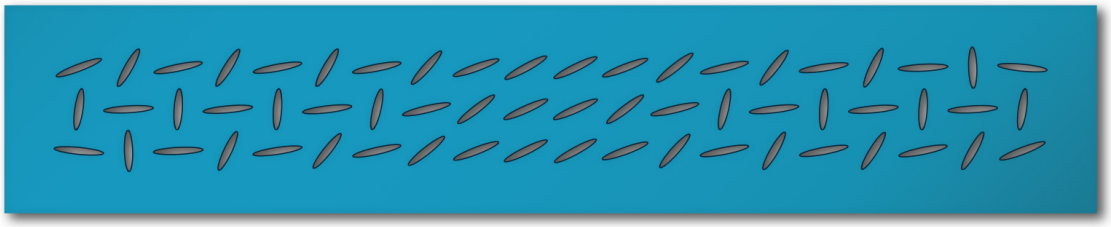

Figure 3.5: The groundstate orientations for square lattices of 3×20.

3.2.2 Stretching the Lattice

In experimental systems [103], the elastic sheet was stretched in a specific direction before allowing it to swell, leading to a background stress $\sigma_{xx} = T\cos\phi$, $\sigma_{yy} = T\sin\phi$. To calculate the coupling energy between the stretching and the dipole angle, we will rotate the system, such that the **x**-axis is defined by the direction of stretching, or $\sigma_{xx} = T$ and the dipole is located at the origin, or

$$\mathbf{b}(\mathbf{q}) = ibq\hat{\mathbf{z}} \times \mathbf{d}\cos(\theta - \theta_0 + \phi). \tag{3.12}$$

It is most appropriate to use the energy functional $E = \frac{1}{2Y_2}\int d^2x \left(\nabla^2\chi\right)^2$. In Fourier space, the dipole term is given by $\nabla^2\chi = i\epsilon_{ik}\frac{q_k}{q^2}b_i(q)$ [17] and the stretching term by $\nabla^2\chi = T\frac{\delta(q)}{q}\delta(\theta)$. The energy is

$$\begin{aligned} E &= \frac{1}{2Y_2}\int \frac{d^2q}{(2\pi)^2}\left(T\frac{\delta(q)}{q}\delta(\theta) - bd\cos^2(\theta - \theta_0 + \phi)\right) \\ &\times \left(-T\frac{\delta(q)}{q}\delta(\theta) + bd\cos^2(\theta - \theta_0 + \phi)\right), \end{aligned} \tag{3.13}$$

from which the coupling energy is

$$\begin{aligned} E_{\text{stretch}} &= -\frac{Tbd}{Y_2(2\pi)^2}\int qdq\int d\theta\frac{\delta(q)}{q}\delta(\theta)\cos^2(\theta - \theta_0 + \phi) \\ &= -\frac{Tbd}{Y_2(2\pi)^2}\cos^2(\phi - \theta_0) \end{aligned} \tag{3.14}$$

The new term causing the dislocation dipoles to align with the direction of stretching competes with original interaction energy, favoring the diamond plate pattern. Following the same minimization procedure as before, we find that for small tensions the diamond

plate pattern is only slightly perturbed, and for large tensions, the dislocation dipoles align along the direction of stretching, which may be seen in Figure 3.6, which are in qualitatively good agreement with experiments [103, 104] [1].

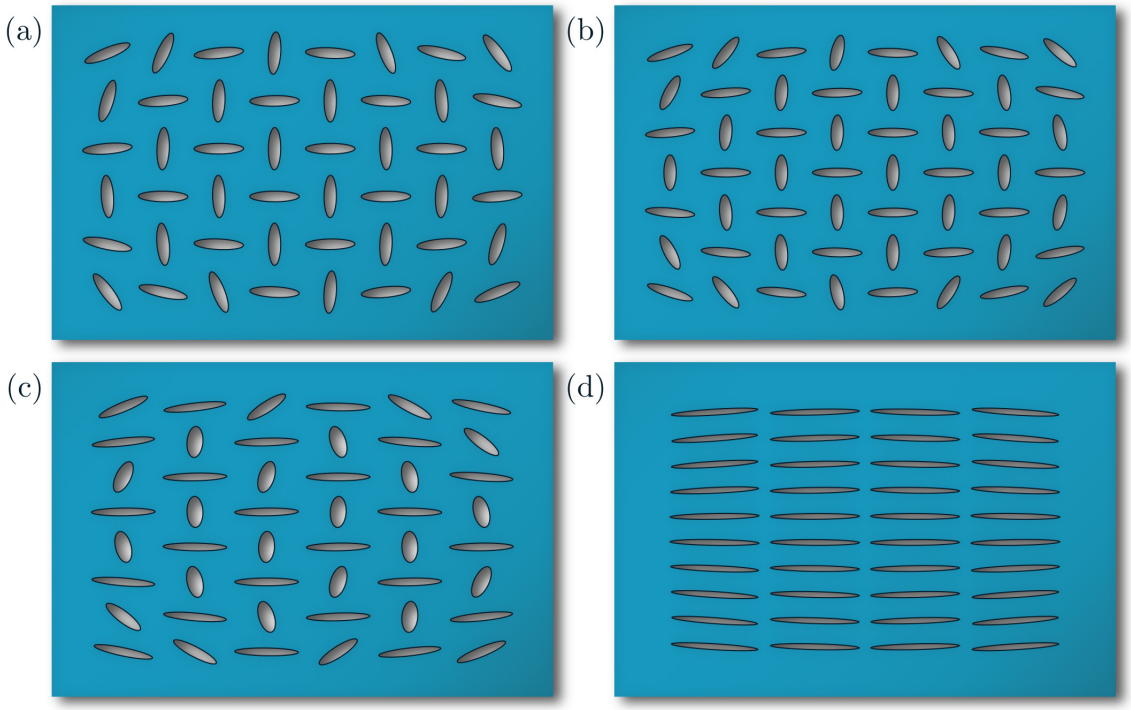

Figure 3.6: The results of the energy minimization for a square lattice of dipoles undergoing a strain of (a) 10%, (b) 25%, (c) 50%, and (d) 75% along one of the principal axes of the lattice. These patterns qualitatively match experiments [103, 104].

3.2.3 Why We Can Ignore Higher Order Terms

Our goal is to prove that we need only consider the first order dipole-dipole term when considering collapsed holes. For simplicity sake, we will study an elongated shape that is symmetric about both its semi-major and semi-minor axes, (see Figure 3.7). Here, we consider only shapes for which the ratio of minor and major axes $a/d_0 \ll 1$.

In the theory of cracks, the height profile of a crack $h(x)$ may be constructed from

[1] In Figure 3.6, the images are drawn with each dislocation dipole represented by an ellipse of aspect ratio 1 : 4, where the orientation of the major axis is calculated from the minimization of the dipole energy. However, because the membranes shown here have undergone uniaxial strain, the boundaries of the ellipses must undergo the identical transformation, $u_x = x + Tx(\cos^2\phi - \sigma\sin^2\phi)x + \frac{1}{4}Ty\sin 2\phi$, $u_y = y + Ty(\sin^2\phi - \sigma\cos^2\phi) + \frac{1}{4}Tx\sin 2\phi$.

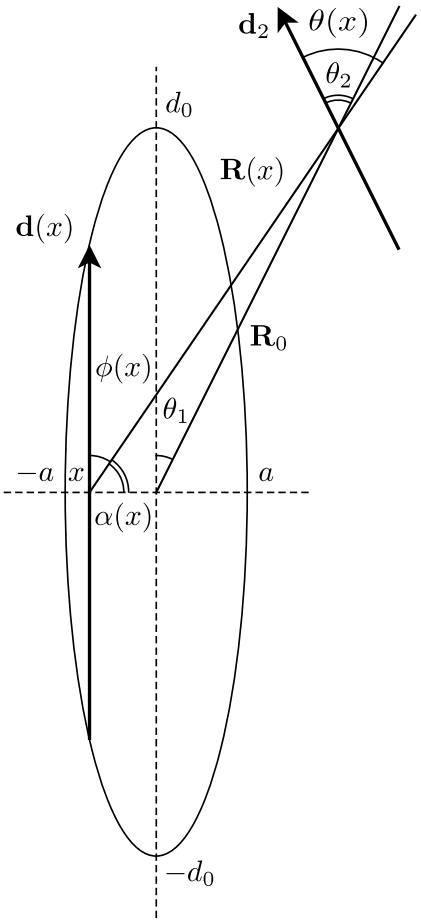

Figure 3.7: Set up for dipole expansion of an elongated shape symmetric about both the x- and y-axes, in this case, an ellipse.

a continuous distribution of finite parallel edge dislocations. A finite edge dislocation of length ℓ can be thought of as a two infinite edge dislocations of the same strength but opposite charge which is given by Burgers vectors situated at $\mathbf{b}_+ = b_0\,\delta(\mathbf{x} - \boldsymbol{\ell}/2)$ and $\mathbf{b}_- = -b_0\,\delta(\mathbf{x} + \boldsymbol{\ell}/2)$, in other words, a dislocation dipole. Given the height profile of a shape, it is trivial to construct it from such dislocation dipoles, $h(x) = d(x)$. Thus, the interaction energy between such a shape made from dislocation dipoles and a single dislocation dipole $\mathbf{d}_2$ located a distance $\mathbf{R}_0$ away is given by:

$$E = -\frac{Y_2 b^2 d_2}{\pi}\int_{-a}^{a} dx \frac{d(x)}{R^2(x)}\left(\cos\left(\phi(x)+\theta(x)\right)\sin\left(\phi(x)\right)\sin\left(\theta(x)\right)+\frac{1}{4}\right). \tag{3.15}$$

By repeated application of the law of cosines, the functional forms of $R(x)$, $\phi(x) = \pi/2 - \alpha(x)$, and $\theta(x)$ are:

$$R^2(x) = R_0^2 + x^2 - 2R_0 x\cos\left(\frac{\pi}{2} + \theta_1\right) = R_0^2 + x^2 + 2R_0 x\sin\theta_1 \tag{3.16}$$

$$\alpha(x) = \cos^{-1}\left(\frac{x + R_0\sin\theta_1}{\sqrt{R_0^2 + x^2 + 2R_0 x\sin\theta_1}}\right) \tag{3.17}$$

$$\theta(x) = \theta_2 - \theta_1 - \alpha(x) + \pi/2. \tag{3.18}$$

The energy density is

$$f = -\frac{f_0 d(x)}{R_0^2 + x^2 + 2R_0 x\sin\theta_1}\left(\frac{1}{4} - \cos(\tilde{\theta} - 2\,\alpha(x))\cos(\alpha(x))\cos(\tilde{\theta} - \alpha(x))\right), \tag{3.19}$$

where $f_0 = Y_2 b^2 d_2/\pi$ and $\tilde{\theta} = \theta_2 - \theta_1$. This may be vastly simplified by expanding the angular terms:

$$\cos(\tilde{\theta} - 2\alpha(x)) = \frac{\cos\tilde{\theta}(x + R_0\sin\theta_1)^2 R_0^2\cos^2\theta_1 + 2\sin\tilde{\theta}\,(x + R_0\sin\theta_1)\,R_0\cos\theta_1}{R_0^2 + x^2 + 2R_0 x\sin\theta_1} \tag{3.20}$$

$$\cos(\tilde{\theta} - \alpha(x)) = \frac{\cos\tilde{\theta}\,(x + R_0\sin\theta_1) + \sin\tilde{\theta}R_0\cos\theta_1}{\sqrt{R_0^2 + x^2 + 2R_0 x\sin\theta_1}}. \tag{3.21}$$

The energy density becomes:

$$\begin{aligned} f &= -\frac{f_0 d(x)}{\left(R_0^2 + x^2 + 2R_0 x\sin\theta_1\right)^3}\left(\frac{\left(R_0^2 + x^2 + 2R_0 x\sin\theta_1\right)^2}{4} - \sum_{n=1}^{4} c_n (x + A)^n\right) \\ &= -\frac{f_0 d(x)}{\left(R_0^2 + x^2 + 2R_0 x\sin\theta_1\right)^3}\sum_{n=0}^{4} c_n \sum_{m=0}^{n}\frac{n!}{m!(n-m)!}A^{n-m}x^m \end{aligned} \tag{3.22}$$

where $A = R_0\sin\theta_1$ and $B = R_1\cos\theta_1$, and the coefficients c_n are given by $c_0 = B^4/4$, $c_1 = B^3\cos\tilde{\theta}\sin\tilde{\theta}$, $c_2 = B^2(\cos^2\tilde{\theta} - 2\sin^2\tilde{\theta}) + B^2/2$, $c_3 = -3B\cos\tilde{\theta}\sin\tilde{\theta}$, and $c_4 = -\cos^2\tilde{\theta} + 1/4$. While the above energy is for general shape of dislocations, we choose a shape to do the actual calculation. For simplicity sake, we choose an ellipse of semi major axis d_0 and semi minor axis a. Thus, $d(x) = 2d_0\sqrt{1 - x^2/a^2}$. With the change of variables, $y = x/a$, our energy integral becomes:

$$E = -\frac{2f_0}{R_0^6}\int_{-1}^{1} dy \frac{d_0 a\sqrt{1 - y^2}}{\left(1 + (\frac{a}{R_0}y)^2 + 2\frac{a}{R_0}y\sin\theta_1\right)^3}\sum_{n=0}^{4} c_n \sum_{m=0}^{n}\frac{n!}{m!(n-m)!}A^{n-m}(ay)^m. \tag{3.23}$$

Expanding the denominator for $\frac{a}{R_0} \ll 1$, we find, $\left(1 + (\frac{a}{R_0}y)^2 + 2\frac{a}{R_0}y\sin\theta_0\right)^{-3}$

$\approx \left(1 - 6\frac{a}{R_0}\sin\theta_0 y + 3\left(\frac{a}{R_0}\right)^2(8\sin^2\theta_0 - 1)y^2 + \cdots\right)$. Now we need only do the integral $\int_{-1}^{1} dy\sqrt{1-y^2}y^n = 2(1-(-1)^n)\int_0^1 \sqrt{1-y^2}y^n$, for, since $\sqrt{1-y^2}$ is even, this integral is zero for odd integer n This is very simple using beta functions, which we may see by the change of variables $t = y'^2$:

$$\begin{aligned} 2\int_0^1 dy'\sqrt{1-y'^2}y'^n &= \int_0^1 \frac{dt}{\sqrt{t}}\sqrt{1-t}t^{n/2} = \int_0^1 dt t^{(n+1)/2-1}(1-t)^{3/2-1} \\ &\equiv B\Big(\frac{1+n}{2},\frac{3}{2}\Big) = \frac{\Gamma\left(\frac{1+n}{2}\right)\Gamma\left(\frac{3}{2}\right)}{\Gamma\left(2+\frac{n}{2}\right)} = \frac{\pi(1+(-1)^n)}{2^{\frac{n}{2}+1}}\frac{(n-1)!!}{(\frac{n}{2}+1)!} \end{aligned} \quad (3.24)$$

The interaction energy is thus:

$$\begin{aligned} E &= -\frac{2f_0d_0a}{R_0^6}\sum_{n=0}^{4}\sum_{m=0}^{n} c_n\frac{n!}{m!(n-m)!}A^{n-m}a^m\frac{\pi}{2^{m/2+2}}\left((1+(-1)^m)\left(2\frac{(m-1)!!}{(\frac{m}{2}+1)!}\right.\right. \\ &+ \left.\left. 3\frac{a^2}{R_0^2}\left(8\sin^2\theta_0 - 1\right)\frac{(m+1)!!}{(\frac{m}{2}+2)!}\right) - 6\frac{a}{R_0}\sin\theta_1\sqrt{2}(1-(-1)^m)\frac{m!!}{(\frac{m+1}{2}+1)!}\right). \end{aligned} \quad (3.25)$$

While this appears to be a complicated expression, let us, for the moment consider only the first order term in a:

$$\begin{aligned} E_0 &= -\frac{\pi f_0 d_0 a}{2R_0^6}\sum_{n=0}^{4} c_n A^n = -\frac{Y_2 b^2 d_2 d_0 a}{4R_0^6}\left(\frac{B^4}{4} + AB^3\cos\tilde{\theta}\sin\tilde{\theta}\right. \\ &+ \left. A^2B^2\left(\cos^2\tilde{\theta} - 2\sin^2\tilde{\theta} + \frac{1}{2}\right) - 3A^3B\cos\tilde{\theta}\sin\tilde{\theta} + A^4\left(\frac{1}{4} - \cos^2\tilde{\theta}\right)\right) \\ &= -\frac{\pi f_0 d_0 a}{2R_0^2}\left(\frac{\cos^4\theta_1}{4} + \left(\cos^3\theta_1\sin\theta_1 - 3\sin^3\theta_0\cos\theta_1\right)\cos\tilde{\theta}\sin\tilde{\theta}\right. \\ &+ \left. \cos^2\theta_1\sin^2\theta_1\left(\cos^2\tilde{\theta} - 2\sin^2\tilde{\theta} + \frac{1}{2}\right) + \sin^4\theta_1\left(\frac{1}{4} - \cos^2\tilde{\theta}\right)\right). \end{aligned} \quad (3.26)$$

This does not appear to have the same functional form as the original energy. However, with the help of some trigonometric identities, we begin to simplify the energy:

$$\cos^4\theta_1 + \sin^4\theta_1\left(1 - 4\cos^2\tilde{\theta}\right) = \frac{1}{2}\sin^2 2\theta_1\cos 2\tilde{\theta} + 1 - 4\sin^2\theta_1\cos^2\tilde{\theta} \quad (3.27)$$

$$\left(\cos^3\theta_1\sin\theta_1 - 3\sin^3\theta_1\cos\theta_1\right)\cos\tilde{\theta}\sin\tilde{\theta} = \frac{1}{4}(2\cos 2\theta_1 - 1)\sin 2\theta_1\sin 2\tilde{\theta} \quad (3.28)$$

$$\left(\cos^2\tilde{\theta} - 2\sin^2\tilde{\theta} + \frac{1}{2}\right)\cos^2\theta_1\sin^2\theta_1 = \frac{3}{8}\cos 2\tilde{\theta}\sin^2 2\theta_1. \quad (3.29)$$

We now use these identities in the energy to find:

$$\begin{aligned} E_0 &= -\frac{\pi f_0 d_0 a}{8R_0^2}\Big(\frac{1}{2}\sin^2 2\theta_1 \cos 2\tilde{\theta} + 1 - \sin^2\theta_1 \cos^2\tilde{\theta} + (2\cos 2\theta_1 - 1)\sin 2\theta_1 \sin 2\tilde{\theta} \\ &+ 3\cos 2\tilde{\theta}\sin^2 2\theta_1\Big) \\ &= -\frac{\pi f_0 d_0 a}{8R_0^2}\Big(2\sin 2\theta_1\Big(\sin 2\theta_1\cos 2\tilde{\theta} - \frac{\sin 2\tilde{\theta}}{2} + \cos 2\theta_1 \sin 2\tilde{\theta}\Big) - \sin^2\theta_1\cos^2\tilde{\theta} + 1\Big). \end{aligned} \tag{3.30}$$

Now we substitute $\tilde{\theta} = \theta_2 - \theta_1$ to find,

$$\begin{aligned} E_0 &= -\frac{\pi f_0 d_0 a}{2R_0^2}\left(\frac{1}{2}\sin 2\theta_1 \sin 2\theta_2 - \sin^2\theta_1\cos^2\tilde{\theta} - \sin\theta_1\cos\theta_1\sin\tilde{\theta}\cos\tilde{\theta} + \frac{1}{4}\right) \\ &= -\frac{Y_2 b^2 d_2 d_0 a}{4R_0^2}\left(\cos(\theta_1+\theta_2)\sin\theta_1\sin\theta_2 + \frac{1}{4}\right). \end{aligned} \tag{3.31}$$

So we have found that to first order in a/R_0 an ellipse of semi major axis d and semi minor axis a interacts with a dislocation dipole of strength d_2 a distance R_0 away like a dislocation dipole with effective dipole strength $\tilde{d} = \pi d_0 a/2$. Higher order terms contain more powers of a/R_0, which can be neglected for very thin shapes or for dipoles that are very far away.

3.3 Conclusion

We have created a model system for an elastic sheet with a square lattice circular holes cut out of it. When the sheet is swollen, or, equivalently, subjected to uniform tension, the holes snap shut. Their major axes align into a diamond plate pattern with long ranged order. While other methods of calculating the orientational order of the holes rely upon nonlinear elasticity theory and finite element simulations, we use simple linear elasticity theory to obtain the same results. Our system also corroborates experimental results of the sheet under external forces. It is difficult to extend it to an infinite lattice, since the minimization would then be over an infinite number of angles. An Ewald type summation may be used for an infinite system whose unit cell is the 2×2 plaquette. However, this is unlikely to lead to new insight, as the diamond plate order is clearly maintained for large systems. Moreover, as we show in the appendix, the dipole interactions are the dominant terms even for more general elliptical holes. This method may easily extended to holes

on other lattices and other geometries. We have demonstrated that the our linear theory captures the dominant piece of the orientational ordering of the collapsed holes and can be used fruitfully to rationally design and prototype new structures.

Chapter 4

In Which Cylinders Complicate the Interaction and New Patterns are Formed

The rational design of complex patterns in two dimensions presents a unique problem. Although fluctuations destroy crystalline order in two dimensional systems above zero temperature, long ranged elastic interactions can help to overcome this complication. By exploiting an elastic instability in a mechanically compressed perforated elastic sheet, a diamond plate pattern featuring long ranged order emerges [77, 103].

In two dimensions there exist only five distinct Bravais lattices, and therefore only a finite number of possible patterns lattices of circular holes in two dimensions can produce. The classification of patterns is additionally complicated by the long ranged interaction between two holes. This prohibits us from using mean field theories and lattice models to find a generic solution to this problem, as the total energy must include contributions from all possible pairwise terms.

In order to expand the library of patterns created by a lattice of holes on a two dimensional elastic sheet, we change the topology of the interaction. Nontrivial solutions to this problem exist on a cylinder due to the long ranged nature of the interactions. The nature of the emergent patterns not only depends upon the underlying lattice defining the position of the holes, but also on the relative orientations of the principal axes of that lattice and the periodic direction of the cylinder.

4.1 The Experiment

The buckling instability caused by hydrostatic compression of a perforated elastic sheet is an extremely robust phenomenon. It can occur at length scales from $< 1\mu \sim >$ 1cm [77, 103], and even homemade samples effortlessly reproduce the signature diamond plate pattern. Pattern transformations in cylindrical samples are equally reliable.

We used commercially available foam tubes designed for insulating canned beverages. The cylinders have dimensions $7\,1/2''$ in inner circumference, $9\,1/2''$ in outer circumference, and $4''$ in height. Upon transferring a template lattice onto the cylinder, holes were excised from the foam cylinder using a $1/2''$ leather punch and hammer. In this case, we used a square lattice with principal axes rotated by $\pm\pi/4$ from the cylinder axis, of lattice constant $a = 7/8''$, 10 lattice sites in circumference and 7 sites high.

The greatest technological challenge we faced was preventing the cylinder from buckling when compressed, as commercially available rigid, transparent tubing was unobtainable in the diameters we required. This problem was solved by supporting the inside of the cylinder with a $6''$ section of $2\,3/8''$ diameter PVC pipe, and the entire apparatus was subsequently enclosed in a glass 24 oz Smuckers™ peanut butter jar. Friction prevents accurate measurements of the the material properties and rigorous numeric measurements of the stress-strain curve of this particular sample.

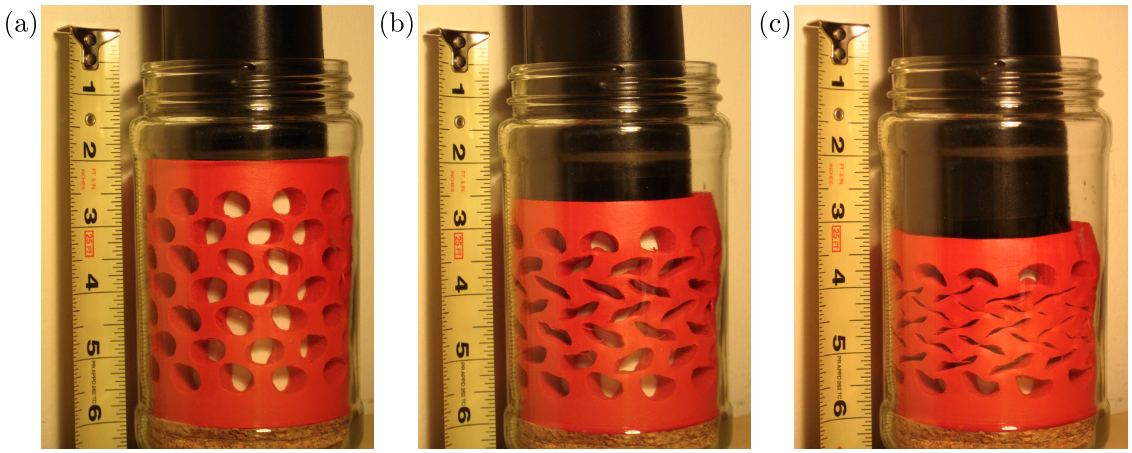

Figure 4.1: (a) The experimental setup for the cylinder with a square lattice of circular holes. (b) Under a compressive strain of $\sim 12.5\%$ the circular symmetry of the holes has clearly been broken. The pattern of collapsed holes, alternating angles $\pm\theta$ with respect to horizontal, has begun to emerge. (c) The fully compressed cylinder under a strain of $\sim 25\%$ clearly displays the final pattern. The central three rows have average angles of $\theta_1 = 0.360$, $\theta_2 = -0.339$, $\theta_3 = 0.366$ from the bottom up, respectively.

Under uniaxial compression parallel to the axis of the cylinder, the initial linear response has little effect on the shape of the holes. However, after reaching a critical strain, symmetry

is broken by the elastic buckling instability and a pattern begins to emerge, which we can see in Figure 4.1. Upon maximum compression, the central three rows of collapsed holes form angles with the horizontal averaging $\theta_1 = 0.360$, $\theta_2 = -0.339$, $\theta_3 = 0.366$ radians from the bottom, middle, and top rows respectively.

4.2 The Model

The introduction of curvature immediately complicates the system. Not only must the elastic energy for the membrane change to include curvature terms, the concept of a lattice is no longer well defined. By adopting the topology of a cylinder, we may bypass these complications. Because the cylinder is isometric to the plane, it has zero Gaussian curvature. We may neglect additional bending energy if the thickness of the membrane is much less than all other relevant length scales.

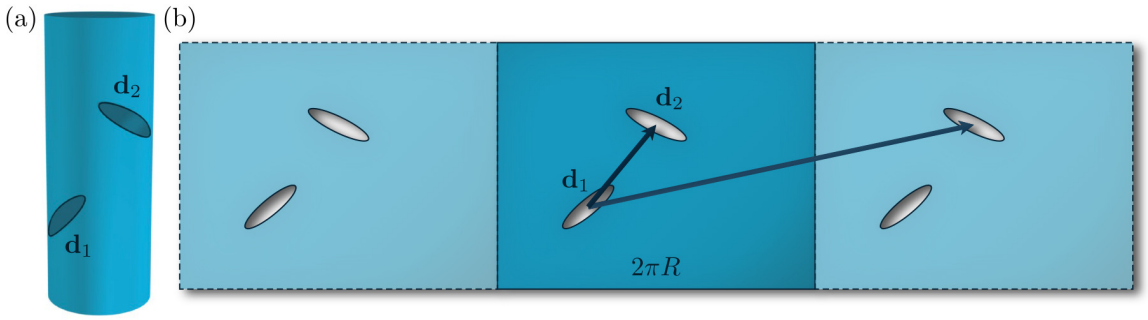

Figure 4.2: (a) A cylinder of radius R with two dislocation dipoles $\mathbf{d}_1$ and $\mathbf{d}_2$. (b) The unrolled version of the cylinder with the first two image cylinders at $2\pi n R\hat{\mathbf{x}}$, $n = \pm 1$.

Consider an infinite elastic cylindrical shell of radius R with its axis parallel to $\hat{\mathbf{z}}$ passing through the origin with two dislocation dipoles on it. To calculate the interaction energy, one could either repeat the integral in equation 3.6 on a cylindrical manifold, or compute the flat version of the interaction with the proper boundary conditions. Imagine cutting the cylinder along the line $r = R$, $\theta = 0$, and unrolling it onto the plane such that $x = R\theta$, $y = z$. The two dipoles are now located at $\mathbf{d}_1 = \{x_1, y_1\}$ and $\mathbf{d}_2 = \{x_2, y_2\}$. They interact not only through the shortest path and the first two replicas located at $\mathbf{d}_i \pm 2\pi R\hat{\mathbf{x}}$, as they would if one simply considered periodic boundary conditions, but, due to the range of the potential, the interaction must also include terms from each of the infinite number of "image" holes.

Note that the calculation on a cylinder is the same as the calculation on an infinite elastic sheet with a copy of the unrolled cylinder located every $2\pi nR$ along the $\hat{\mathbf{x}}$ direction (see Figure 4.2). Therefore, the interaction between two dislocation dipoles on a cylinder is given by,

$$E = -\frac{Y_2}{\pi}\frac{b^2 d_1 d_2}{R^2}\sum_{n=-\infty}^{\infty}\frac{\cos\big(\theta_1+\theta_2-2\theta_n\big)\sin\big(\theta_1-\theta_n\big)\sin\big(\theta_2-\theta_n\big)+\frac{1}{4}}{\big(X+2\pi n\big)^2+Y^2}, \tag{4.1}$$

where $X=\frac{x_2-x_1}{R}$, $Y=\frac{y_2-y_1}{R}$, and $\theta_n=\tan^{-1}\left(\frac{Y}{X-2\pi n}\right)$ is the angle between dipole 1 and the n^{th} image of dipole 2. Upon expanding the trigonometric functions in equation (4.1), the energy consists of 5 terms, each of which may be summed,

$$E = -\frac{Y_2}{\pi}\frac{b^2 d_1 d_2}{R^2}\sum_{n=-\infty}^{\infty}\sum_{k=0}^{4}a_k(\theta_1,\theta_2)\frac{Y^{4-k}\big(X+2\pi n\big)^k}{\big[(X+2\pi n)^2+Y^2\big]^3}, \tag{4.2}$$

where the $a_k(\theta_1,\theta_2)$ are given by, $a_0(\theta_1,\theta_2) = -\cos(\theta_1+\theta_2)\cos\theta_1\cos\theta_2$, $a_1(\theta_1,\theta_2) = -\frac{1}{2}\big(\sin 2\theta_1+\sin 2\theta_2+2\sin 2(\theta_1+\theta_2)\big)$, $a_2(\theta_1,\theta_2)=\frac{1}{2}\big(3\cos 2(\theta_1+\theta_2)-1\big)$, $a_3(\theta_1,\theta_2) = -\frac{1}{2}\big(\sin 2\theta_1+\sin 2\theta_2-2\sin 2(\theta_1+\theta_2)\big)$, $a_4(\theta_1,\theta_2)=\cos(\theta_1+\theta_2)\sin\theta_1\sin\theta_2$. In order to calculate the five sums in equation (4.2), we first note that $s_0(p,q)=\sum_{n=-\infty}^{\infty}\frac{1}{(p+2\pi n)^2+q^2}=\frac{\sinh q}{2q(\cosh q-\cos p)}$. The five sums are given by:

$$\begin{aligned}
\sum_{n=-\infty}^{\infty}\frac{1}{\big[(X+2\pi n)^2+Y^2)\big]^3} &= \frac{1}{8Y}\frac{\partial}{\partial Y}\left(\frac{1}{Y}\partial_y s_0(X,Y)\right)\\
\sum_{n=-\infty}^{\infty}\frac{X+2\pi n}{\big[(X+2\pi n)^2+Y^2)\big]^3} &= \frac{1}{8Y}\partial^2_{XY}s_0(X,Y)\\
\sum_{n=-\infty}^{\infty}\frac{(X+2\pi n)^2}{\big[(X+2\pi n)^2+Y^2)\big]^3} &= \frac{1}{8}\partial^2_X s_0(X,Y)-\frac{1}{8Y}\partial_Y s_0(X,Y)\\
\sum_{n=-\infty}^{\infty}\frac{(X+2\pi n)^3}{\big[(X+2\pi n)^2+Y^2)\big]^3} &= -\frac{Y}{8}\partial^2_{XY}s_0(X,Y)-\frac{1}{2}\partial_X s_0(X,Y)\\
\sum_{n=-\infty}^{\infty}\frac{(X+2\pi n)^4}{\big[(X+2\pi n)^2+Y^2)\big]^3} &= -\frac{Y^2}{8}\partial^2_X s_0(X,Y)+\frac{5Y}{8}\partial_Y s_0(X,Y)+s_0(X,Y).
\end{aligned} \tag{4.3}$$

Combining these we arrive at a final, albeit complicated, expression for the pairwise inter-

action of two dislocation dipole on a cylinder,

$$\begin{aligned} E &= -\frac{Y_2 b^2 d_1 d_2}{4R^2}\frac{\pi}{H^3}\Bigg[\frac{2H^2\sinh Y}{Y} + 2H\sin X\sinh Y\big(\sin 2\theta_1 + \sin 2\theta_2 - \sin 2(\theta_1+\theta_2)\big) \\ &+ \big(3H + \cos X\cosh 2Y - \cos 2X\cosh Y\big)\big(\cos 2\theta_1 + \cos 2\theta_2 - \cos 2(\theta_1+\theta_2)\big) \\ &+ Y\big((\cos 2X - 3)\sinh Y + \cos X\sinh 2Y\big)\cos 2(\theta_1+\theta_2) \\ &+ Y\big((\cosh 2Y - 3)\sin X + \cosh Y\sin 2X\big)\cos 2(\theta_1+\theta_2)\Bigg], \end{aligned} \tag{4.4}$$

where $H = \cos X - \cosh Y$.

The effect of long ranged elastic interactions serves to reinforce the same angular dipole interaction seen in the flat case for dipole pairs located at the same height on the cylinder, $E(X, Y=0) = -\frac{Y_2 b^2 d_1 d_2 \pi^2}{R^2}\cos(\theta_1+\theta_2)\sin\theta_1\sin\theta_2$.

4.2.1 Three Simple Lattices

Our ultimate goal is to be able to find the arrangement of holes that generates a specific pattern. Before we can attempt this, we must first get acquainted with the library of complex patterns that can be generated by simple lattices in this cylindrical topology. All lattices that can be written down on the plane are transferrable to a cylinder with the appropriate periodicity.

The Square Lattice

We begin with perhaps the most obvious choice, the square lattice, defined by primitive vectors $\mathbf{a}_1 = \{a, 0\}$, $\mathbf{a}_2 = \{0, a\}$, N holes around the circumference and M holes high. For $N \times 1$ square lattices, all of the dislocation dipoles make the angle $\theta_i = \pi/6$ with respect to the **x**-axis. All pairwise terms in this configuration have $Y = 0$, and therefore have the angular dependence of the flat interaction $\cos(\theta_i + \theta_j)\sin\theta_i\sin\theta_j$, which has a minimum at $\theta_i = \theta_j = \pi/6$. However, for $N \times M$ square lattices, with $M, N \geq 3$, the dipoles in top and bottom rows all orient in the same direction and the all rest of the dipoles point along a slightly different angle. There is weak dependence on N for both of these angles, $\theta_{1,M} = 0.5582 + 0.03270N^{-2} + O(N^{-4})$ and $\theta_{[2,M-1]} = 0.5885 + 0.0504N^{-2} + O(N^{-4})$. Although for practical purposes, all of the dipoles point in the same direction $\theta \approx 0.5802$

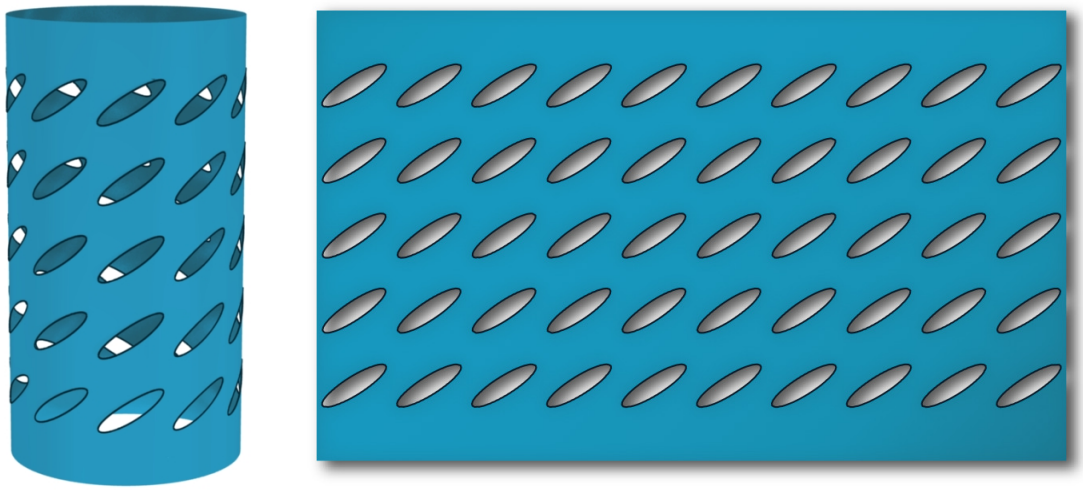

Figure 4.3: *left:* (Video online) A typical representative of the pattern generated by the square lattice on a cylinder. *right:* The pattern generated by a 10×5 square lattice shown on the unwrapped cylinder. All of the collapsed holes form the angle $\theta \approx 0.58$ radians with respect to the **x**-axis.

radians. An example of this pattern is shown in Figure 4.3 both a video[1] of the cylinder and a flattened, unwrapped version of the cylinder.

The Triangular Lattice

The triangular lattice, $\mathbf{a}_1 = \{a, 0\}$, $\mathbf{a}_2 = \{\frac{a}{2}, \frac{\sqrt{3}a}{2}\}$, also produces fairly universal patterns. All the dipoles in each row point in the same direction, alternating between $\pm\theta$ each row, see Figure 4.4. As with the square lattice, the top and bottom rows serve as a boundary layer with slightly different average angle than the rest, and the magnitudes of these angles have weak dependence on the circumference, $|\theta_{1,M}| = 0.5075 - 0.0170N^{-2} + O(N^{-4})$ and $|\theta_{[2,M-1]}| = 0.4959 - 0.02567N^{-2} + O(N^{-4})$.

The Honeycomb Lattice

The next simple lattice we consider is the honeycomb lattice, a triangular lattice, $\mathbf{a}_1 = \{2a, 0\}$, $\mathbf{a}_2 = \{a, \sqrt{3}a\}$, with a basis of two sites $\mathbf{b}_1 = \{0, 0\}$, $\mathbf{b}_2 = \{a, \frac{a}{\sqrt{3}}\}$. This produces a pattern qualitatively similar to the square lattice, but the overall angle is different, see

[1] All videos in this section may not play unless viewed with Adobe Acrobat Reader version 9.0 or later.

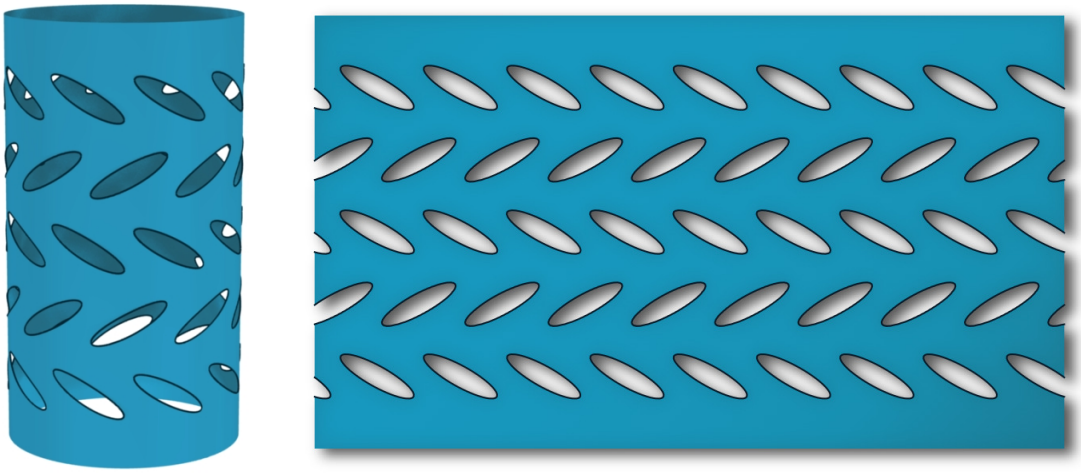

Figure 4.4: *left:* (Video online) A sample ground state configuration of a triangular lattice on a cylinder. *right:* The unwrapped pattern made by a 9×5 triangular lattice. Dipoles alternate sign between rows, taking the values $\theta \approx \pm 50$.

Figure 4.5. All of the dipoles in the lattice point in approximately the same direction. There is a weak angular dependence on both dimensions of the lattice, $\theta = -0.3260 + 0.0498N^{-2} - 0.1431M^{-1} + O(M^{-2}) + O(N^{-4})$.

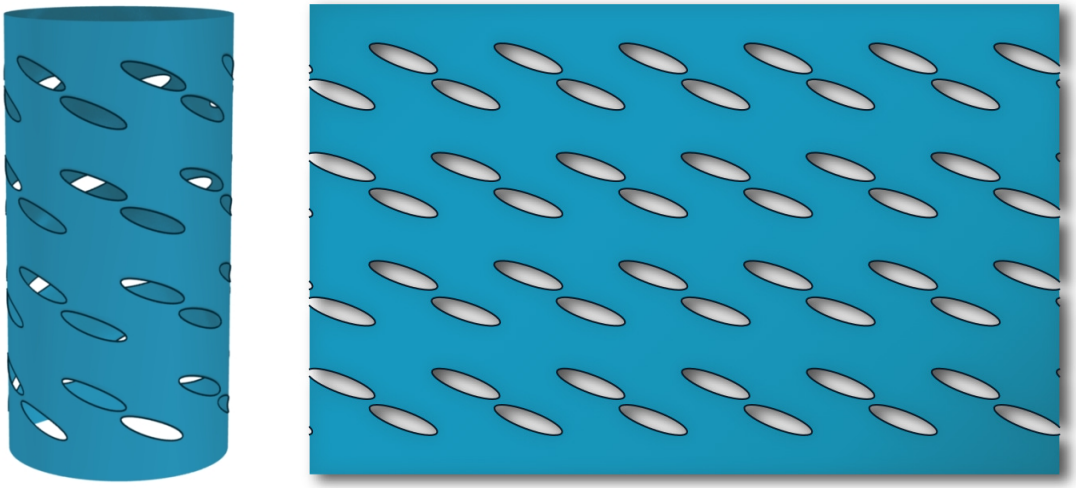

Figure 4.5: *left:* (Video online) An example pattern resulting from a honeycomb lattice of 6×8 holes on a cylinder. *right:* The flattened cylinder shows all dipoles all aligned with angle $\theta \approx -0.32$ radians.

Although neither of the patterns generated by the square lattice nor the honeycomb

lattice likely have much appeal for devices, they both exhibit chiral symmetry breaking. Both underling achiral lattices produce macroscopically chiral phases, albeit with different pitch. By tuning the ratio of values of the principal lattice vectors, we hope to gain excellent control over the exact pitch.

4.2.2 Another Look at the Lattices

The three simple lattices we have chosen certainly yield patterns not achievable in a flat geometry; unfortunately, neither the patterns generated by the square lattice nor the honeycomb lattice likely have much appeal for devices. The way in which the lattices are wrapped around the cylinder introduces a new degree of freedom which can be used to control the formation of complex patterns. All three of the previous lattices have been wrapped such that one of their principal axes points perpendicular to the axis of the cylinder. Respecting the periodicities of both the lattice and the cylinder constrains the ways in which the lattices can be wrapped around the cylinder. The shape of the top and bottom rows of the lattice may also have a profound impact on the ground state pattern. In the following, we intentionally minimize this effect by considering only cases where the symmetry of the lattice is commensurate with the circumference of the cylinder, and the boundary rows are always perpendicular to the cylinder axis.

The Other Square Lattice

The second square lattice, $\mathbf{a}_1 = \{\frac{a}{\sqrt{2}}, \frac{a}{\sqrt{2}}\}$, $\mathbf{a}_2 = \{\frac{a}{\sqrt{2}}, -\frac{a}{\sqrt{2}}\}$, we consider has principal axes rotated by $\pi/4$ away from the axis of the cylinder. Notice that we have truncated the boundary such that it lies perpendicular to the cylinder axis. This square lattice forms a pattern that is similar to the diamond plate pattern, except that the dipoles are not aligned with the two principal axes of the lattice, see Figure 4.6. Instead of the alternating pattern of angles $\theta = 0$, $\theta = \pi/2$ seen in the diamond plate lattice, the angles created by the square lattice are oriented at $\theta \approx \pm 0.35 \approx \pm\pi/9$ with respect to the $\mathbf{x}$-axis. The weak dependence on the lattice size is as follows, $|\theta| = 0.3461 - 0.1946N^{-2} - 0.0563M^{-1} + O(M^{-2}) + O(N^{-4})$.

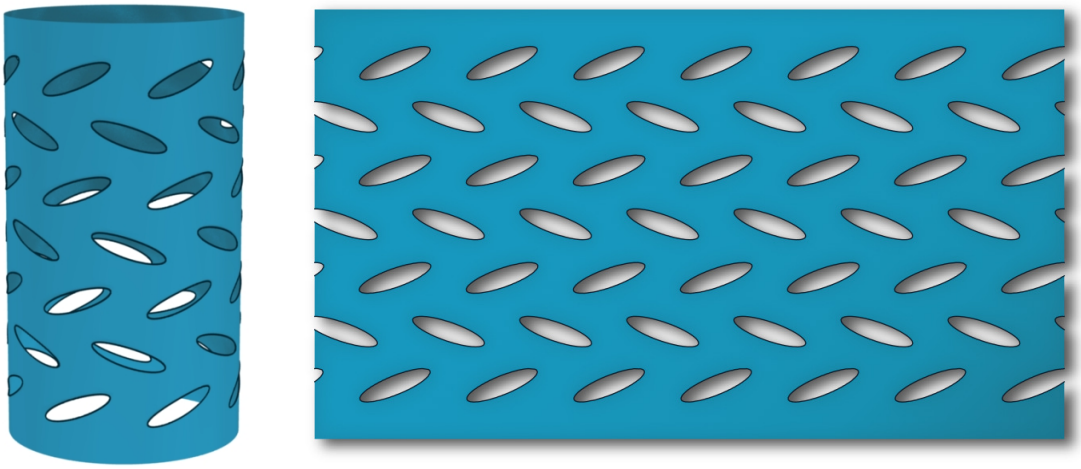

Figure 4.6: *left:* (Video online) By changing the alignment of the principal axes to $\pm\pi/4$ away from the axis of the cylinder, this square lattice produces a radically different patterns from the initial version. *right:* This pattern generated by a tilted square lattice of 7×7 holes features alternating rows of dipoles sitting at angle $|\theta| \approx 0.35 \approx \pi/9$ radians.

The Triangular Lattice *(take 2)*

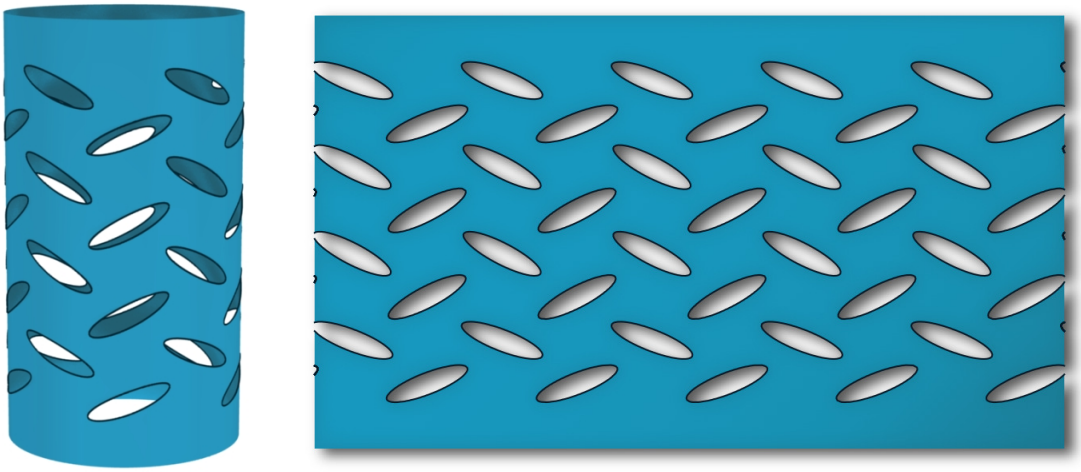

Figure 4.7: *left:* (Video online) The rotated triangular lattice is the third example of a rectangular lattice with a basis. The aspect ratio of the unit cell controls the average dipole angles of the "twisted" diamond plate pattern. *right:* This pattern generated by a rotated triangular lattice with 10×4 holes features alternating rows of dipoles sitting at angle $\theta \sim \pm 0.4904$ radians

The rotated version of the triangular lattice, $\mathbf{a}_1 = \{\frac{\sqrt{3}a}{2}, \frac{a}{2}\}$, $\mathbf{a}_2 = \{0, a\}$, appears to

have stripes, alternating columns of dipoles at $\theta \approx \pm 0.4904$. There is very little spread in angle as the number of holes around the circumference increases; while the angles depend more strongly on the height of the lattice, $|\theta| = 0.4866 - 0.2787M^{-1} + O(M^{-2})$.

Notice that both of the triangular lattices and the rotated square lattice are actually rectangular lattices with a basis located midway through the unit cell. By changing the aspect ratio of the rectangular unit cell control the relative orientations of the dipoles in these "twisted" diamond plate lattices.

The Honeycomb Lattice Redux

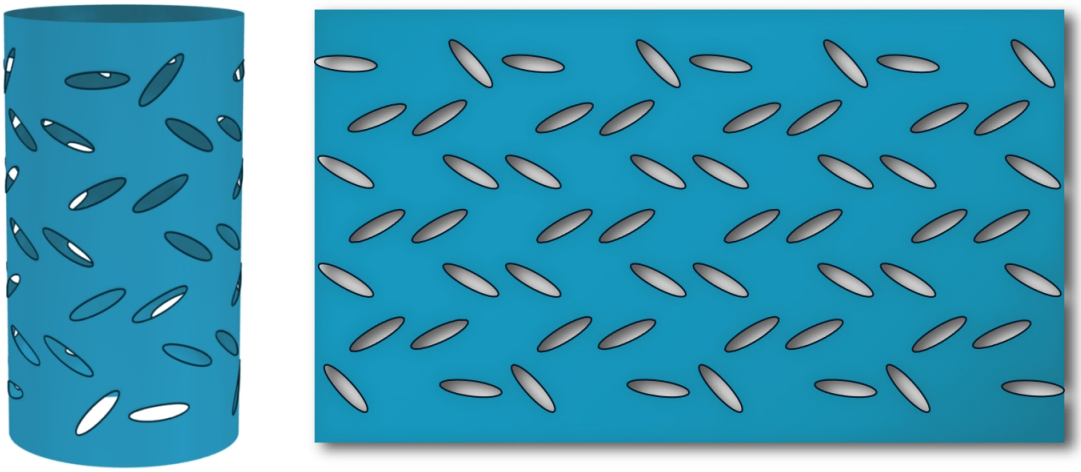

Figure 4.8: *left:* (Video online) A new type of pattern forms from a rotated honeycomb lattice of holes on a cylinder. *right:* This pattern generated by 8×7 holes on the rotated honeycomb lattice features pairs of dipoles, both at the same angle, which.

The alternate honeycomb lattice, $\mathbf{a}_1 = \{\sqrt{3}a, a\}$, $\mathbf{a}_2 = \{0, 2a\}$, with basis vectors $\mathbf{b}_1 = \{0, 0\}$, $\mathbf{b}_2 = \{\frac{a}{\sqrt{3}}, a\}$, is the first lattice to yield a truly new pattern. In the interior of the pattern, neighboring horizontal pairs of dipoles orient in the same direction. As with the familiar rectangular lattice with a basis, these pairs alternate direction with respect to the pairs in the neighboring column or row, $\theta \approx \pm 0.495$, as shown in Figure 4.8. These angles are fairly insensitive to the width of the lattice. The angular dependence on height is also an "odd-even" effect; the lattices with an odd number of rows approach the limiting angle $|\theta| \approx 0.4966$ more rapidly than those with an even number of rows, $|\theta_{\text{odd}}| = 0.4966 -$

$0.0721M^{-2} + O(M^{-3})$, $|\theta_{\text{even}}| = 0.4966 - 0.0125M^{-1} - 0.0852M^{-2} + O(M^{-3})$.

The top and bottom rows form a different pattern than the interior, alternating between nearly flat $\theta \approx -0.123$ radians and sharply tilted $\theta \approx -0.845$. The boundary layer displays an "odd-even" effect, much more striking than the interior, see Figure 4.9. For lattices with an odd number of rows, the order of the pairs (flat and tilted) is reversed from the bottom to the top row. Whereas, when there are an even number of rows, the order remains the same, but the angles reverse sign.

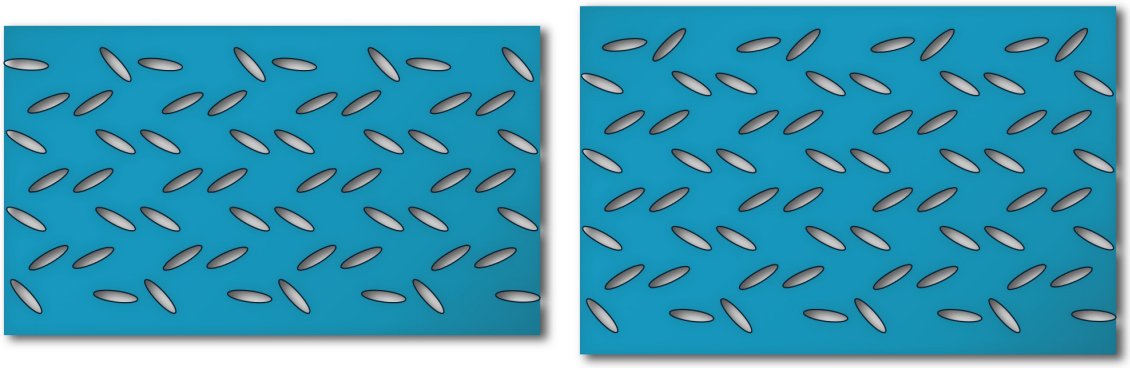

Figure 4.9: The top and bottom rows of the honeycomb lattice form a boundary layer with a distinctly different pattern than the interior. The pattern of these rows exhibits an "odd-even" effect depending on the number of rows of holes. As they encircle the cylinder, the dipoles on the bottom row alternate between $\theta \approx -0.123$ and $\theta \approx -0.845$. However, the dipoles on the top row alternate between $\theta \approx -0.845$ and $\theta \approx -0.123$ for cylinders with an odd number of rows (left) and $\theta \approx 0.123$ and $\theta \approx 0.845$ for cylinders with an even number of rows (right).

By changing the aspect ratio of either the overall unit cell of the honeycomb lattice, or the relative position of the bases points, we expect to gain exquisite control over the exact orientations of the holes.

4.2.3 Complex Lattices Lead to Complex Patterns

A systematic study of variations of the aforementioned simple lattices will yield very precise control over the exact orientations of the dislocation dipoles for a few classes of patterns. As variations on a theme, they can only add incrementally to our library of patterns. We must turn to increasingly complex lattices in order to broaden the range of accessible patterns.

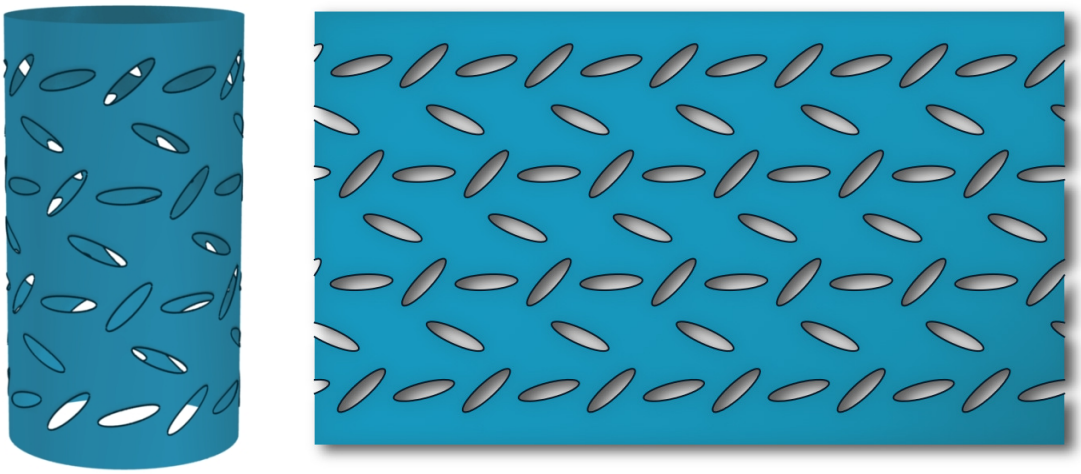

Figure 4.10: *left:* (Video online) As the complexity of the lattice increase so too does the intricacy of the pattern it can generate. The kagome lattice of holes in a cylindrical elastic sheet produces this complicated pattern. *right:* This kagome lattice, six unit cells wide and three unit cells tall, each containing three holes, generates a complex pattern.

The kagome lattice represents a perfect case study, as it has recently gained popularity in the condensed mater literature for its novel mechanical and vibrational properties [96, 93, 72]. The kagome lattice consists of a triangular lattice $\mathbf{a}_1 = \{2a, 0\}\, \mathbf{a}_2 = \{a, \sqrt{3}a\}$ with a basis of three points $\mathbf{b}_1 = \{0, 0\}$, $\mathbf{b}_2 = \{a, 0\}$, $\mathbf{b}_3 = \{\frac{a}{2}, \frac{\sqrt{3}a}{2}\}$. The resulting pattern retains remnants of the symmetry of the underlying lattice, as shown in Figure 4.10.

4.3 Conclusion

Unlike the diamond plate lattice on a flat membrane, the patterns on cylinders are sensitive to the number of holes both in circumference and in height. This immediately begs the question: how do we create extensive patterns? Because cylinders are isometric to the plane, curvature will not effect our ability to transfer patterns onto a flat substrate. By capitalizing on the periodicity of the cylinder, we can upgrade from the contact printing method outlined in [103] to a rolling printer. By filling the interior of the cylinder with a viscous solvent, the exact orientation and position of the holes may be transferred to a flat substrate of any dimension, see Figure 4.11.

By changing the topology of the perforated elastic membrane from a flat plane to a

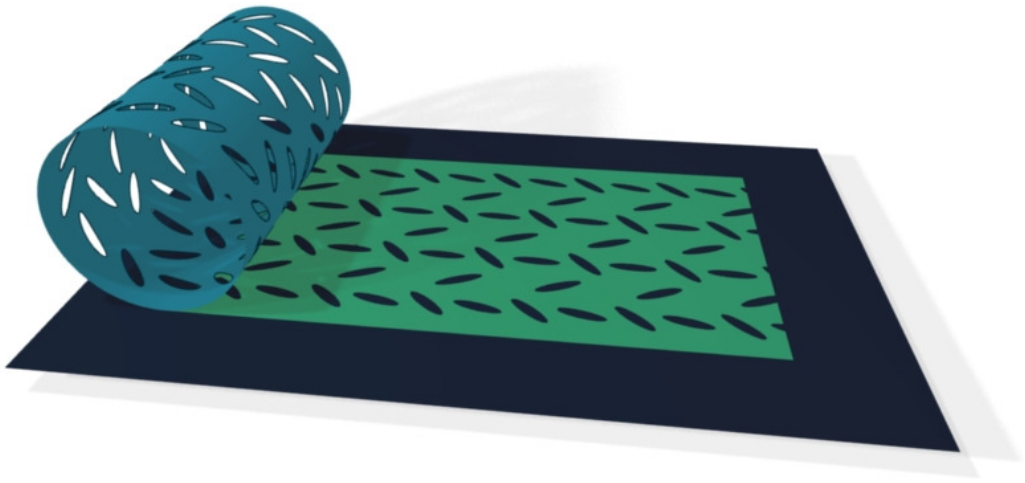

Figure 4.11: (Video online) An example application uses the pattern generated by the Kagome lattice on a cylinder as a rolling printer onto a flat substrate.

cylinder, we may further exploit the long ranged nature of the elastic interactions to create a vast library of new patterns. Using a simple approximation and linear elasticity theory, we are able to rapidly predict the types of patterns generated by a large variety of lattices both on flat and cylindrical membranes. Although any computational methods, such as finite element simulations, the prohibitive time cost per simulation makes these methods unappealing to design patterns. As of the writing of this chapter, an algorithm for determining the distribution of holes in an elastic membrane given a specific pattern does not yet exist. Such an algorithm would use our simple linear mode in conjunction with a steepest descent algorithm to find the exact locations of the holes.

Chapter 5

In Which Chirality Frustrates Layers and a Screw is Born

5.1 Introduction

Nearly four decades ago, the analogy between chiral smectics and superconductors first entered the standard smectic lore, equating their equilibrium phases, phase transitions, material parameters, and topological defects [24]. Remarkably similar free energy functionals both feature a Landau expansion in a complex scalar order parameter, minimal coupling of the order parameter to an internal vector field and a frustrating surface term. The Ginzburg parameter κ_G, the ratio of two natural lengthscales, determines the phase behavior of both systems. In type I materials characterized by $\kappa_G < 1/\sqrt{2}$, spontaneous symmetry breaking differentiates between the high and low temperature phases. Known as the Meissner effect, the superconducting phase expels magnetic field, breaking gauge symmetry. Likewise, flat smectic A layers suppress twist and break rotational symmetry. Type II materials $\kappa_G > 1/\sqrt{2}$ exhibit a mixed phase wherein a proliferation of defects admit quantized units of the external field into the sample, mediating the intrinsic frustration. Just as the lattice of flux vortices in the Abrikosov phase of type II superconductors allow magnetic field to penetrate the sample, so too grain boundaries of parallel screw dislocations enable twist to propagate through the layered structure of the twist-grain-boundary phase. The preexisting superconducting literature detailing the Abrikosov vortex lattice phase [3, 59] fascilitated the prediction of the twist-grain-boundary TGB phase [84]. From the first observation of the TGB phase [36, 37], an industry formed devoted to characterizing it [94, 92, 91, 79, 31, 85, 86]. This immensely successful superconductor analogy finally reached its limit with the discovery of the helical nanofilament (HN) phase, which has no superconducting equivalent [46, 73].

The HN phase, like the TGB, phase originates from the intrinsic frustration between equally spaced layered smectic phase and macroscopic chirality. In systems of achiral bent-core liquid crystals and mixtures of achiral bent-core and rod-like molecules, chiral phases often arise from spontaneous symmetry breaking [67, 28, 29, 97]. Macroscopic homochiral domains populate the sample, with both handednesses occurring with equal probability. Unlike the B2 and B3 bent core phases, where molecular tilt with respect to the smectic layers admits chirality through the spontaneous breaking of mirror symmetry, the HN phase, a smectic A phase, allows the director to twist with respect to the layers [89, 88, 99, 81].

Although initially considered to have the same morphology as the TGB, the hierarchical structure of the HN phase exhibits a distinctively different morphology. Upon cooling from a high temperature fluid phase, helical bundles consisting of approximately five nested smectic layers, nucleate. These homochiral, coherently rotating filaments form the basis of the hierarchical HN phase. They assemble, with axes aligned, into a hexagonal lattice producing a nanoporous bulk structure. From freeze fracture experiments on the bulk HN texture, an archetypal Bouligand texture [12, 68] reveals an underlying cholesteric texture with the pitch direction parallel to the center of the filaments [46]. The HN phase accommodates chirality by forming helicoidal layers that locally match a cholesteric texture at the expense of long ranged ordering of the layers. Alternatively, the TGB phase locally prefers flat layers, only admitting chirality across grain boundaries, thus allowing the layer normal to rotate by a fixed angle.

The Landau-de Gennes free energy provides the appropriate framework for analyzing all chiral smectic A phases. Despite not accounting for all of the intricacies of bent-core mesogens, this minimal model produces a texture with the same morphology and properties observed in the HN phase. The minimizer for this energy functional in a small cylinder locally resembles an individual helical smectic bundle. Bulk textures formed from lattices of bundles feature coherently rotating filaments and a nanoporous structure. A comparison of lattices establishes the hexagonal lattice as the most energetically favorable. It is relatively trivial to show that the HN phase is stable over both the smectic A and cholesteric phases, calculating the relative stability of the TGB phase requires a full stability analysis

of the free energy functional and reveals the innate difference between chiral smectics and superconductors.

5.2 The Landau-de Gennes Free Energy

Landau-de Gennes theory has proven exceedingly powerful in understanding the phase behavior of smectics, particularly the nematic to smectic A transition (NA) [24]. The onset of smectic order is characterized by the development of a mass density wave locally modulating the molecular positions. In mean-field theory, a non-zero value for the complex smectic order parameter $\psi = \psi_0 e^{iq_{\rm sm}\phi}$ indicates both the emergence of smectic order and the location of smectic layers denoted by level sets of the phase field $\phi = na$, where $a = 2\pi/q_{\rm sm}$ is the layer spacing. Gauge-like minimal coupling of the nematic director field $\mathbf{n}$ to the smectic order parameter, reminiscent of the Landau-Ginzburg theory for superconductors, penalizes deviations of the director field from the layer normal $\mathbf{N}$. The low energy deformations to the nematic director field still cost energy in the smectic phase. This phenomenology is captured by the Landau-de Gennes free energy,

$$\begin{aligned} F_{\text{L-dG}} &= \int d^3\mathbf{x}\left[C|(\nabla - iq_{\rm sm}\mathbf{n})\psi|^2 + t|\psi|^2 + \frac{u}{2}|\psi|^4 + f_{\rm Frank}\right] \\ f_{\rm Frank} &= \frac{1}{2}\Big[K_1(\nabla\cdot\mathbf{n})^2 + K_2(\mathbf{n}\cdot\nabla\times\mathbf{n} - q_0)^2 + K_3\big((\mathbf{n}\cdot\nabla)\mathbf{n}\big)^2\Big], \end{aligned} \tag{5.1}$$

where $t \sim T/T_{\rm NA} - 1$ is the reduced temperature, q_0 is the chirality of the high temperature cholesteric phase and the three terms of the Frank free energy describe the splay, twist, and bend deformations of the nematic field. Further discussion shall be restricted to the London limit [69] (unless otherwise specified), where gradients in the magnitude of the smectic order may be neglected.

The ratio of two natural lengthscales, $\kappa_G = \lambda/\xi$, the twist Ginzburg parameter, governs the phase behavior of chiral smectics: the twist penetration depth is the maximum length the director can deviate from the layer normal, twist penetration depth $\lambda = (K_2/B)^{1/2}$, where $B = 2Cq_{\rm sm}^2\psi_0^2$ is the compression modulus, and the coherence length $\xi = (C/t)^{1/2}$ is the distance over which ψ_0 decays to zero. Type I materials ($\kappa_G < \frac{1}{\sqrt{2}}$) completely expel chirality from the smectic phase. In the smectic phase $\psi_0 \neq 0$, the free energy density attains

its minimal value $f_{\mathrm{sm_A}} = \frac{-t^2}{2u} + \frac{K_2 q_0^2}{2}$ corresponding to the order parameter $\psi_0 = (-r/u)^{1/2}$, and the cholesteric phase becomes favorable above the thermodynamic critical chirality $q_{\mathrm{th}} = t/(K_2 u)^{1/2}$.

The TGB phase, an intermediate phase featured in type II materials ($\kappa_G > \frac{1}{\sqrt{2}}$) admits chirality into the smectic via grain boundaries formed from an infinite row of parallel screw dislocations. Each grain boundary joins two regions of smectic A together by rotating the layer normals through an angle $\alpha = 2\tan^{-1}(a/\ell_d)$, which depends on the separation between defects ℓ_d. A lattice of parallel grain boundaries separated by ℓ_b enable the smectic normals to approximately follow an underlying cholesteric with the average chirality $\bar{q} = \alpha/\ell_b$. The transition between smectic A and TGB occurs at $q_{c_1} = \frac{\ln \kappa_G}{\sqrt{2}\kappa_G} q_{\mathrm{th}}$ when the energy gain from introducing twist outweighs cost of introducing a single defect. Calculating boundary between the TGB and cholesteric phases requires an examination of the stability operator $M(\mathbf{x}, \mathbf{x}') = \dfrac{\delta F(\mathbf{x})}{\delta\psi^*(\mathbf{x})\delta\psi(\mathbf{x}')}$. The onset of order coincides with the first eigenvalue of the stability operator going negative, in this case, at $q_{c_2} = \sqrt{2}\kappa_G q_{\mathrm{th}}$. [84]

5.2.1 Chirality and Frustration and the Screw Dislocation

Let us for the moment consider regions of constant, non-zero smectic order. The energy of such a system,

$$F = \frac{1}{2}\int d^3x \Big[B\big|\nabla\phi - \mathbf{n}\big|^2 + K_1\big(\nabla\cdot\mathbf{n}\big)^2 + K_2\big(\mathbf{n}\cdot\nabla\times\mathbf{n} + q_0\big)^2 + K_3\big[(\mathbf{n}\cdot\nabla)\mathbf{n}\big]^2\Big], \quad (5.2)$$

clearly displays the frustration in the system. The compression term $B|\nabla\phi - \mathbf{n}|^2$ prefers equally spaced layers with normals parallel to the nematic director field. However, because $\nabla\times\nabla\phi = 0$, this identification can never minimize the chiral term of the Frank free energy, $\frac{K_2}{2}(\mathbf{n}\cdot\nabla\times\mathbf{n} + q_0)^2$.

Chiral smectics often turn to the screw dislocation to alleviate frustration with layers. Despite the layers themselves not contributing to the chiral energy, a singularity in the compression energy requiring the smectic order to vanish near the divergence allows the cholesteric to admit chirality into the system.

5.3 The Structure of the Helical Nanofilament Phase

The Helical Nanofilament phase represents a new solution to the chiral Landau-de Gennes free energy. It occurs at higher chirality and lower reduced temperature than the TGB phase. For this reason, we abandon the usual assumption that the director field is be given by the smectic layer normal, $\mathbf{n} = \dfrac{\nabla\phi}{|\nabla\phi|} = \mathbf{N}$, in favor of the *ansatz* that the director field is given by the standard cholesteric texture $\mathbf{n}^* = \cos(q_0 z)\mathbf{e}_x + \sin(q_0 z)\mathbf{e}_y$. This identification is an absolute minimizer of the chiral Frank free energy. As we shall discover, a smectic texture grown from this background chiral field minimizes the chiral Landau-de Gennes free energy.

5.3.1 Phase Fields and the Screw Dislocation

The phase field description of the smectic introduces an ambiguity to this problem. Two phase fields that describe the same set of layers do not necessarily have the same energetics. Consider the free energy functional for an achiral smectic A ($\mathbf{n} = \mathbf{N}$),

$$F = \frac{1}{2}\int d^3x \Big[B\big((\nabla\phi)^2 - 1\big)^2 + K_1(\nabla\cdot\mathbf{N})^2 \Big], \tag{5.3}$$

which consists of a compression energy term, which has been made nonlinear here for ease of calculation, and a bending term which is proportional to the mean curvature $H = \frac{1}{2}\nabla\cdot\mathbf{N}$ of the smectic layers. The phase field for a screw dislocation is given by a helicoid, a minimal surface $H = 0$,

$$\phi = z - \frac{b}{2\pi}\tan^{-1}\left(\frac{y}{x}\right), \tag{5.4}$$

where $b = 2d$, corresponds to a single screw dislocation and the notation is adopted from the Burgers' vector notation of dislocations in crystals. Near the origin, the compression energy from Eq. 5.3 diverges as $\sim r^{-2}$.

The location of these compression singularities depends on the exact form of the phase field. The choice that the layer normal at $x, y = \infty$ is $\mathbf{n} = \hat{\mathbf{z}}$, implying the phase field $\phi = z - \frac{d}{\pi}\tan^{-1}(y/x) = 0$, forces the singularity to the axis of the helicoid. On the other

hand, the phase field,

$$\phi = x\cos\left(\frac{\pi z}{d}\right) - y\sin\left(\frac{\pi z}{d}\right) = 0, \tag{5.5}$$

which gives an identical surface, minimizes the compression energy along the axis and diverges as $x, y \to \infty$. Level sets of these two phase field reveal the underlying cause for the discrepancy. Level sets of the phase field in Eq. 5.4 all intersect along the line $x = 0$, $y = 0$. Whereas, level sets of the phase field in Eq. 5.5 describe nested helicoids, which eventually intersect when too many of them fill in the space between half periods of the central $\phi = 0$ helicoid.

5.3.2 A Single Bundle

We seek a high chirality solution in which the director retains its high temperature cholesteric form, $\mathbf{n} = \cos(q_0 z)\mathbf{e}_x + \sin(q_0 z)\mathbf{e}_y$, and the smectic phase field is then chosen to minimize the compression energy for this choice of director. Since $\nabla \times \mathbf{n} = -q_0\mathbf{n}$, there is no phase field for which $\nabla\phi = \mathbf{n}$ everywhere, however, we can construct a phase field that agrees on a lower dimensional set of points. To this end, we consider the local phase field

$$\phi^{\rm loc} = x\cos(q_0 z) + y\sin(q_0 z) = r\cos(q_0 z - \theta), \tag{5.6}$$

where in the final equality we have employed cylindrical polar coordinates. The compression is $|\nabla\phi^{\rm loc} - \mathbf{n}|^2 = q_0^2 r^2 \sin^2(q_0 z - \theta)$ and vanishes everywhere on the two-dimensional surface of the helicoid $\theta = \{q_0 z, q_0 z + \pi\}$. This texture, therefore, locally attains the absolute minimum of the Landau-de Gennes free energy and represents the optimum local configuration for a chiral smectic. The smectic layers (Figure 5.1) are themselves helicoids, the level sets of $\phi^{\rm loc}$, that intersect the zero compression surface orthogonally. Consequently the compression of the layers grows quadratically with their radial size so that they are naturally confined to a finite region; the texture is only local and does not fill space. The free energy per unit length of a cylindrical region of radius R is $\pi B q_0^2 R^4/8$. A comparison with the free energy per unit length of an equal volume region of the smectic-A texture, $\pi K_2 q_0^2 R^2/2$ suggests a natural size of $R_* = \sqrt{2}\lambda$.

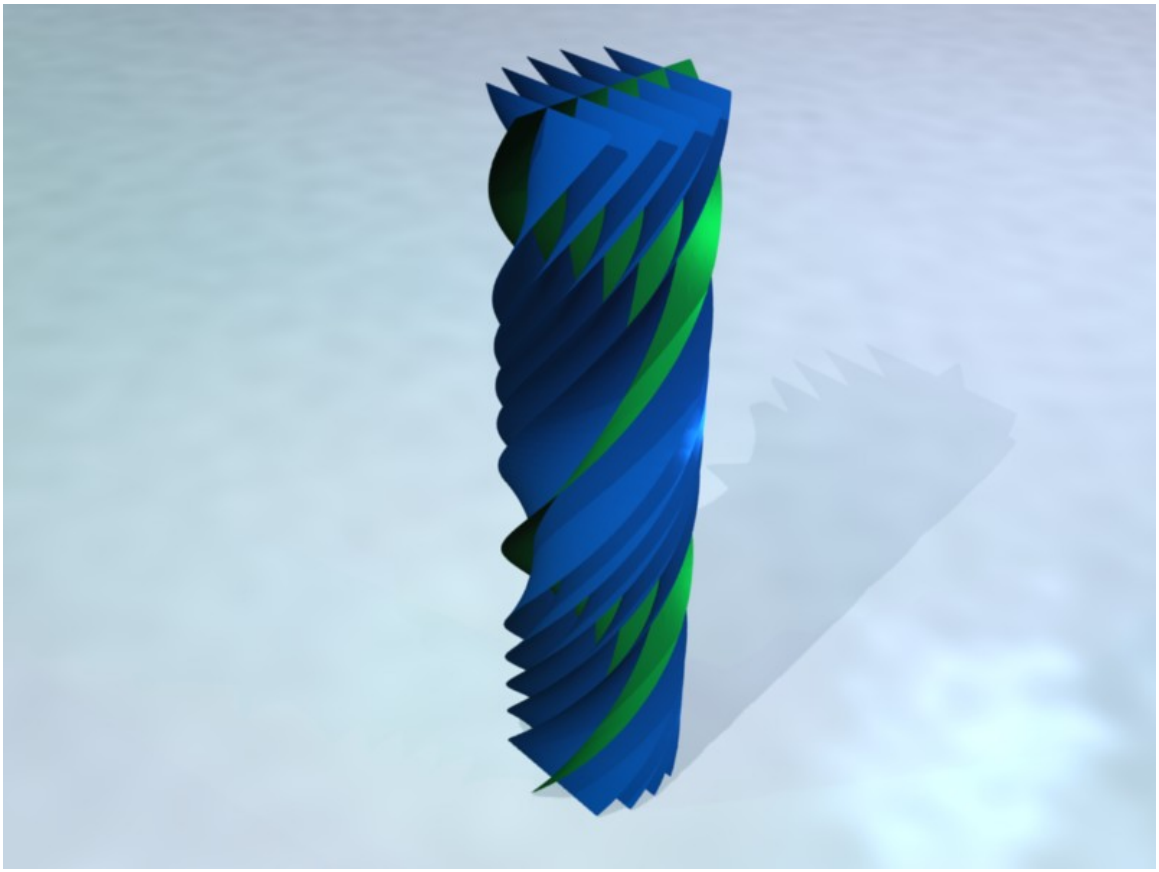

Figure 5.1: A single bundle of helicoidal layers locally attains the absolute minimum of the chiral Landau-de Gennes free energy. The compression energy vanishes on the surface shown here in green.

5.3.3 Complex Analysis and Smectic Topology

This type of local construction is reminiscent of double twist cylinders in the blue phases [102]: there too the absolute minimum of the free energy density is attained only locally, on the axes of the double twist cylinders. Space filling textures, the cubic blue phases, are constructed by repeating this local texture in a periodic manner at the expense of incorporating topologically required disclination lines. We seek an analogous construction for a bulk texture of our helical smectic bundles. Just as in the blue phases, such a state will be stable if the benefit gained from the locally favored bundles outweighs the cost of any associated defects.

It is natural to consider two-dimensional arrangements of bundles since then they can

all be supported by a common underlying cholesteric director field – such a construction automatically incorporates the macroscopic "phase coherence" evidenced by the Bouligand texture of the experiment [46]. The smectic phase field can be obtained by constraining its form to match the rotation of the director along the z-direction and considering only variations with respect to x, y. The constrained Euler-Lagrange equation is then $\nabla_\perp \cdot (\psi_0^2 \nabla\phi) = \nabla_\perp \cdot (\psi_0^2 \mathbf{n})$, so that in the London approximation where ψ_0 is constant almost everywhere ϕ is harmonic in x, y and we propose the general *ansatz* for the phase field $\phi = \mathrm{Re}[\Theta(w)\mathrm{e}^{-iq_0 z}]$, where Θ is an analytic function of $w = x + iy$. The compression energy functional $F_{\mathrm{comp}} = \frac{B}{2}\int d^3x |\nabla\phi - \mathbf{n}|^2$ for this choice of phase field, after integrating out the periodic modulation along z, simplifies to

$$\frac{F_{\mathrm{comp}}}{L} = \frac{B}{2}\int_\Omega d^2w \left\{ \frac{q_0^2}{2}\left|\Theta(w)\right|^2 + \left|\partial_w \Theta(w) - 1\right|^2 \right\}, \tag{5.7}$$

where Ω encloses the region containing nonzero smectic order.

The local optimum configuration, Eq. (5.6), is recovered when $\Theta \sim w$ is linear. A bulk texture will therefore correspond to an analytic function with a large number of simple zeros in the complex plane, as each defines the axis of a helical bundle. Lattice configurations of simple zeros can be easily constructed with the aid of elliptic functions, in particular the doubly periodic Weierstrass $\wp$-function,

$$\wp\big(z;\omega_1,\omega_2\big) := \frac{1}{z^2} + \sum_{(m,n)\neq(0,0)} \left(\frac{1}{(z + m\omega_1 + n\omega_2)^2} - \frac{1}{(m\omega_1 + n\omega_2)^2} \right), \tag{5.8}$$

with complex periods ω_1 and ω_2 [101]. This meromorphic function has double poles at the lattice points defined by $L = \{m\omega_1 + n\omega_2 : m, n \in \mathbb{Z}\}$. By Cauchy's argument principle, there must be either two simple zeros or a zero of multiplicity two within the fundamental parallelogram defined by the two periods. The phase field

$$\phi = \mathrm{Re}\big[\wp^{-1/2}(x + iy;\omega_1,\omega_2)e^{-iq_0 z}\big], \tag{5.9}$$

defines a smectic with helical bundles centered at the lattice points of L with requisite defects adjoining neighboring bundles.

The following analysis will primarily rely upon an alternate, but equivalent, Jacobian

representation of elliptic functions. Before proceeding, we briefly review a few salient properties of elliptic functions. The Weierstass $\wp$-function satisfies the differential equation,

$$\big(\wp'(z)\big)^2 = 4\wp^3(z) - g_2\wp(z) - g_3 = 4\big(\wp(z) - e_1\big)\big(\wp(z) - e_2\big)\big(\wp(z) - e_3\big), \tag{5.10}$$

where the $\wp$-function can be described interchangeably by the elliptic invariants g_2 and g_3 or the roots of the characteristic polynomial which are the half-period values $\wp(\omega_1/2) = e_1$, $\wp(-\omega_1/2 - \omega_2/2) = e_2$, and $\wp(\omega_2/2) = e_3$, which satisfy $e_1 + e_2 + e_3 = 0$. The Weierstrass $\wp$-function may be re-expressed in terms of Jacobi elliptic functions

$$\wp(z) = e_3 + \frac{e_1 - e_3}{\mathrm{sn}^2\big(z\sqrt{e_1 - e_3}, m\big)}, \tag{5.11}$$

where $m = (e_2 - e_3)/(e_1 - e_3)$, is the square of the elliptic modulus. Jacobi elliptic functions, generalizations of trigonometric functions, arise as solutions to the real pendulum problem $\ddot{\theta} - \omega^2 \sin(\theta) = 0$. The The quarter-periods of the Jacobi elliptic functions are $K(m)$ and $iK(1-m)$, where $K(m) = \int_0^{\pi/2} \frac{dt}{\sqrt{1 - m\sin^2(t)}}$, $m \in [0, 1]$, is the complete elliptic integral of the first kind. Consider the minimal rectangle in the complex plane with vertices $\{0,\, K(m),\, K(m) + iK(1-m),\, iK(1-m)\}$, labeled by s, c, d, and n, respectively. The elliptic function $\mathrm{pq}(z, m)$, where p,q can be any two of the letters s, c, d, and n, has a simple zero at p, a simple pole at q and the difference between p and q is half-period. Jacobi elliptic functions become trigonometric functions in the limit the elliptic modulus goes to zero, $\mathrm{sn}(z, 0) = \sin(z)$, $\mathrm{cn}(z, 0) = \cos(z)$ and $\mathrm{dn}(z, 0) = 1$. A few useful identities satisfied by Jacobi elliptic functions include: representation through other Jacobi elliptic functions,

$$\mathrm{sn}^2(z, m) + \mathrm{cn}^2(z, m) = 1,\ \mathrm{dn}^2(z, m) + m\mathrm{sn}^2(z, m) = 1; \tag{5.12}$$

rotation formulæ,

$$\mathrm{sn}(iz, m) = i\mathrm{sn}(z, 1-m),\ \mathrm{cn}(iz, m) = \mathrm{nc}(z, 1-m),\ \mathrm{dn}(iz, m) = \mathrm{dc}(z, 1-m); \tag{5.13}$$

addition formulæ and complex expansions,

$$\begin{aligned}\mathrm{sn}(u+v,m) &= \frac{\mathrm{sn}(u,m)\mathrm{cn}(v,m)\mathrm{dn}(v,m)+\mathrm{sn}(v,m)\mathrm{cn}(u,m)\mathrm{dn}(u,m)}{1-m\mathrm{sn}^2(u,m)sn^2(v,m)},\\ \mathrm{sn}(u+iv,m) &= \frac{\mathrm{sn}(u,m)\mathrm{dn}(v,1-m)+i\mathrm{cn}(u,m)\mathrm{dn}(u,m)\mathrm{cn}(v,1-m)\mathrm{sn}(v,1-m)}{\mathrm{cn}^1(v,1-m)+m\mathrm{sn}^2(u,m)\mathrm{sn}^2(v,1-m}\end{aligned} \tag{5.14}$$

the rest of which may be derived from Eqs. 5.12 and 5.13. [2, 101]

5.3.4 A Bulk Texture and the Helical Nanofilament Phase

The layer structure corresponding to a phase field constructed from any two dimensional lattice of zeros corresponds to a candidate bulk texture for the HN phase. We consider two highly symmetric cases: the lemniscatic case ($g_2 = 1$, $g_3 = 0$) defines a square lattice and the equianharmonic case ($g_2 = 0$, $g_3 = 1$) corresponds to a hexagonal lattice of bundles[1]. It is convenient to introduce a dimensionless coordinate $\zeta = w/l$, where l is the lattice constant.

The Lemniscatic Case

The square lattice of zeros can be defined by the analytic function

$$\tilde{\Theta}_{\mathrm{sq}}(\zeta) = \mathrm{sd}\left(2K\left(\frac{1}{2}\right)\zeta, \frac{1}{2}\right), \tag{5.15}$$

which also has a lattice of simple poles at $\zeta = j+\frac{1}{2}+i\left(k+\frac{1}{2}\right),\ \forall j,k \in \mathbb{Z}$. The smectic texture resulting from a simple pole is extremely pathological. Consider the local construction, $\phi = \mathrm{Re}\left[(x+iy)^{-1}e^{-iq_0 z}\right] = \frac{x}{x^2+y^2}\cos(q_0 z) - \frac{y}{x^2+y^2}\sin(q_0 z) = \cos(q_0 z-\theta)/r$. Not only does this structure center upon a left handed helicoid, a compression singularity resulting from the convergence of all the layers at the origin plagues it. In the neighborhood of such divergences, the free energy remains finite by allowing the magnitude of the smectic order to vanish (Figure 5.2). The high temperature cholesteric phase lives in these melted regions.

[1] The naming convention is inherited from the corresponding special cases of Weierstrass $\wp$-functions [2].

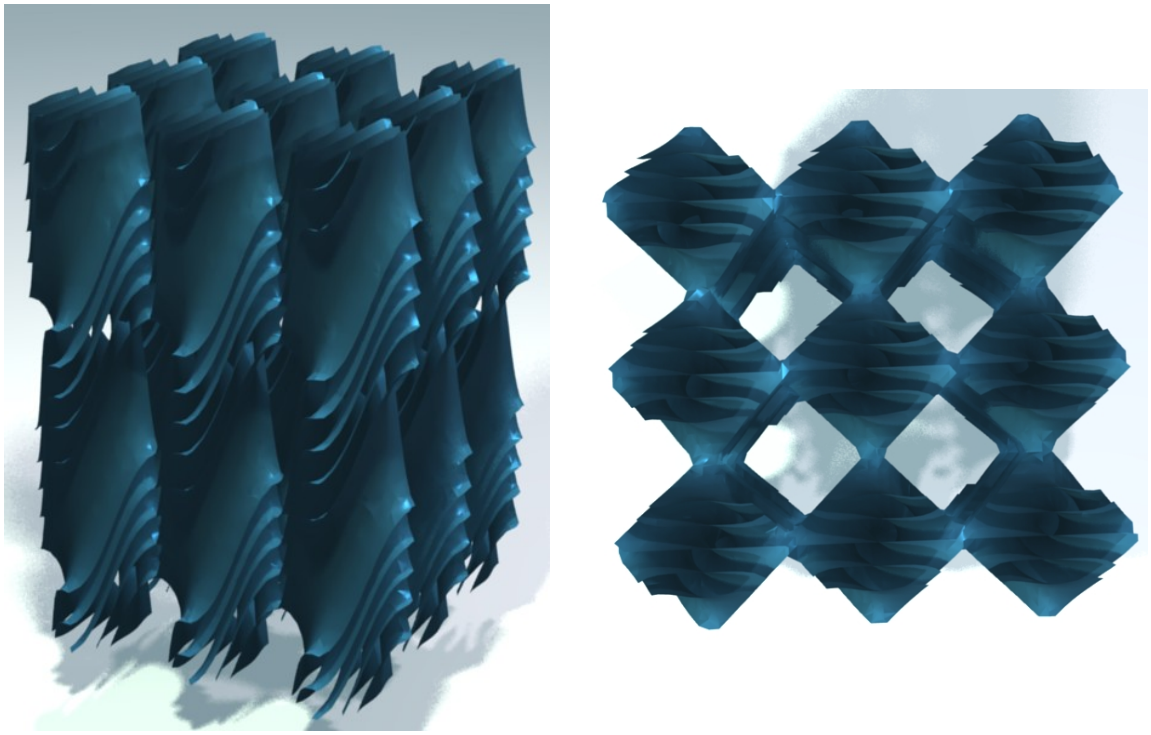

Figure 5.2: *left:* (Video online) The smectic texture corresponding to a square lattice of bundles. The conjugate lattice of defects, $\tilde{\Theta}_{\rm sq} \sim \zeta^{-1}$, correspond to helicoids of the opposite handedness. *right:* Top view.

The Equianharmonic Case

For the equianharmonic case, $e_1 = \frac{1}{2^{2/3}}$, $e_2 = \frac{1}{2^{2/3}}(-1)^{2/3} = \frac{1}{2^{2/3}}\big(-\frac{1}{2} + i\frac{\sqrt{3}}{2}\big)$, $e_3 = \frac{1}{2^{2/3}}(-1)^{4/3} = -\frac{1}{2^{2/3}}\big(\frac{1}{2} + i\frac{\sqrt{3}}{2}\big)$, defined by the function,

$$\begin{aligned}\Theta_{\rm hex}(w) &= \left[e_3 + \frac{e_1 - e_3}{\mathrm{sn}^2\big(\sqrt{e_1 - e_3}w, m\big)}\right]^{-1/2} = \left[e_1 + \left(\frac{e_1 - e_3}{\mathrm{sn}^2\big(\sqrt{e_1 - e_3}w, m\big)} - e_1 + e_3\right)\right]^{-1/2} \\ &= e_1^{-1/2}\left[1 + \big(1 - (-1)^{4/3}\big)\mathrm{cs}^2\big(\sqrt{e_1 - e_3}w, m\big)\right]^{-1/2}, \end{aligned} \tag{5.16}$$

where $m = (-1)^{1/3}$, does not, in its current state, have nice analytic properties because of the complex elliptic modulus. The following algebra involving many well known elliptic function identities, will result in a form on the phase field with favorable complex properties [2, 101]. First we apply the transformation $\mathrm{cs}(w, m) = i\mathrm{ns}(iw, 1-m)$ followed by the Landen

transformation,

$$\mathrm{sn}\left[\left(1+\sqrt{1-M}\right)w, \left(\tfrac{1-\sqrt{1-M}}{1+\sqrt{1-M}}\right)^2\right] = \left(1+\sqrt{1-M}\right)\frac{\mathrm{sn}(w,M)\mathrm{cn}(w,M)}{\mathrm{dn}(w,M)}, \tag{5.17}$$

where $M = \frac{4\sqrt{1-m}}{(1+\sqrt{1-m})^2} = 8-4\sqrt{3}$, which results in the following phase field,

$$\begin{aligned}\Theta_{\mathrm{hex}}(w) &= 2^{1/3}\left[1-\frac{1-\frac{e_3}{e_1}}{\mathrm{sn}^2\left(i\sqrt{e_1-e_3}w, 1-m\right)}\right]^{-1/2} \\ &= 2^{1/3}\left[1-\frac{1-\frac{e_3}{e_1}}{\left(\frac{2}{1+\sqrt{1-m}}\right)^2}\frac{\mathrm{dn}^2\left(\frac{i\sqrt{e_1-e_3}}{\frac{2}{1+\sqrt{1-m}}}w, M\right)}{\mathrm{sn}^2\left(\frac{i\sqrt{e_1-e_3}}{\frac{2}{1+\sqrt{1-m}}}w, M\right)\mathrm{cn}^2\left(\frac{i\sqrt{e_1-e_3}}{\frac{2}{1+\sqrt{1-m}}}w, M\right)}\right]^{-1/2}.\end{aligned} \tag{5.18}$$

One final set of transformations, $\mathrm{sn}(w,M) = -\frac{i}{\sqrt{M}}\mathrm{sc}\left(i\sqrt{M}w, \frac{M-1}{M}\right)$, $\mathrm{cn}(w,M) = \mathrm{dc}\left(i\sqrt{M}w, \frac{M-1}{M}\right)$, $\mathrm{dn}(w,M) = \mathrm{nc}\left(i\sqrt{M}w, \frac{M-1}{M}\right)$, renders the coefficient of the elliptic functions real and the elliptic modulus in the range $[0,1]$, as follows:

$$\begin{aligned}\Theta_{\mathrm{hex}}(w) &= 2^{1/3}\left[1+\frac{\left(1-\frac{e_3}{e_1}\right)\frac{(1+\sqrt{1-m})^2}{4}\frac{4\sqrt{1-m}}{(1+\sqrt{1-m})^2}\ \mathrm{nc}^2\left(\frac{\sqrt{M}\sqrt{e_1-e_3}}{-\frac{2}{1+\sqrt{1-m}}}w, \frac{(1-\sqrt{1-m})^2}{-4\sqrt{1-m}}\right)}{\mathrm{sc}^2\left(\frac{\sqrt{M}\sqrt{e_1-e_3}}{-\frac{2}{1+\sqrt{1-m}}}w, \frac{(1-\sqrt{1-m})^2}{-4\sqrt{1-m}}\right)\mathrm{dc}^2\left(\frac{\sqrt{M}\sqrt{e_1-e_3}}{-\frac{2}{1+\sqrt{1-m}}}w, \frac{(1-\sqrt{1-m})^2}{-4\sqrt{1-m}}\right)}\right]^{-1/2} \\ &= 2^{1/3}\left[1+\frac{\left(1-\frac{e_3}{e_1}\right)\sqrt{1-m}\ \mathrm{cn}^2\left(\frac{-\sqrt{e_1-e_3}}{(1-m)^{-1/4}}w, -\frac{(1-\sqrt{1-m})^2}{4\sqrt{1-m}}\right)}{\mathrm{sn}^2\left(\frac{-\sqrt{e_1-e_3}}{(1-m)^{-1/4}}w, \frac{(1-\sqrt{1-m})^2}{4\sqrt{1-m}}\right)\mathrm{dn}^2\left(\frac{\sqrt{e_1-e_3}}{(1-m)^{-1/4}}w, -\frac{(1-\sqrt{1-m})^2}{4\sqrt{1-m}}\right)}\right]^{-1/2} \\ &= 2^{1/3}\left[1+\sqrt{3}\frac{\mathrm{cn}^2\left(-\frac{3^{1/4}}{2^{1/3}}w, \frac{2-\sqrt{3}}{4}\right)}{\mathrm{sn}\left(-\frac{3^{1/4}}{2^{1/3}}w, \frac{2-\sqrt{3}}{4}\right)\mathrm{dn}\left(-\frac{3^{1/4}}{2^{1/3}}w, \frac{2-\sqrt{3}}{4}\right)}\right]^{-1/2}.\end{aligned} \tag{5.19}$$

Upon transforming to the nondimensionalized coordinate $2K\left(\frac{2-\sqrt{3}}{4}\right)\zeta = \frac{3^{1/4}}{2^{1/3}}w/l$, the simple zeroes corresponding to the centers of each helical bundle live on the lattice $\zeta = w/l = j + \left(\frac{1}{2} + i\frac{sqrt3}{2}\right)k,\ \forall j,k \in \mathbb{Z}$. The compression energy is minimized when $\partial_w = 1$ near a simple zero. We finally arrive at a suitably well behaved function to describe the hexagonal lattice of bundles (Figure 5.3),

$$\tilde{\Theta}_{\mathrm{hex}}(\zeta) = \frac{3^{1/4}}{k}\left(1+\sqrt{3}\frac{\mathrm{cn}^2(k\zeta,m)}{\mathrm{dn}^2(k\zeta,m)\mathrm{sn}^2(k\zeta,m)}\right)^{-1/2}, \tag{5.20}$$

where $k = 2K(m) \approx 3.196$ is twice the complete elliptic integral of the first kind and $m = \frac{2-\sqrt{3}}{4}$ is the square of the elliptic modulus that sets the period ratio. The zeros of $\tilde{\Theta}_{\mathrm{hex}}$ sit on a triangular lattice, and the complementary divergences take the form of square root

branch points, $\tilde{\Theta}_{\rm hex} \sim \zeta^{-1/2}$, situated on a honeycomb lattice. Simple zeros correspond helicoids of the same handedness and pitch as the cholesteric director field while the layer structure near the divergences is that of a half-helicoid of the opposite handedness. Adjacent bundles join together smoothly through saddle points, at which the bulk structure deviates significantly from the single bundle structure.

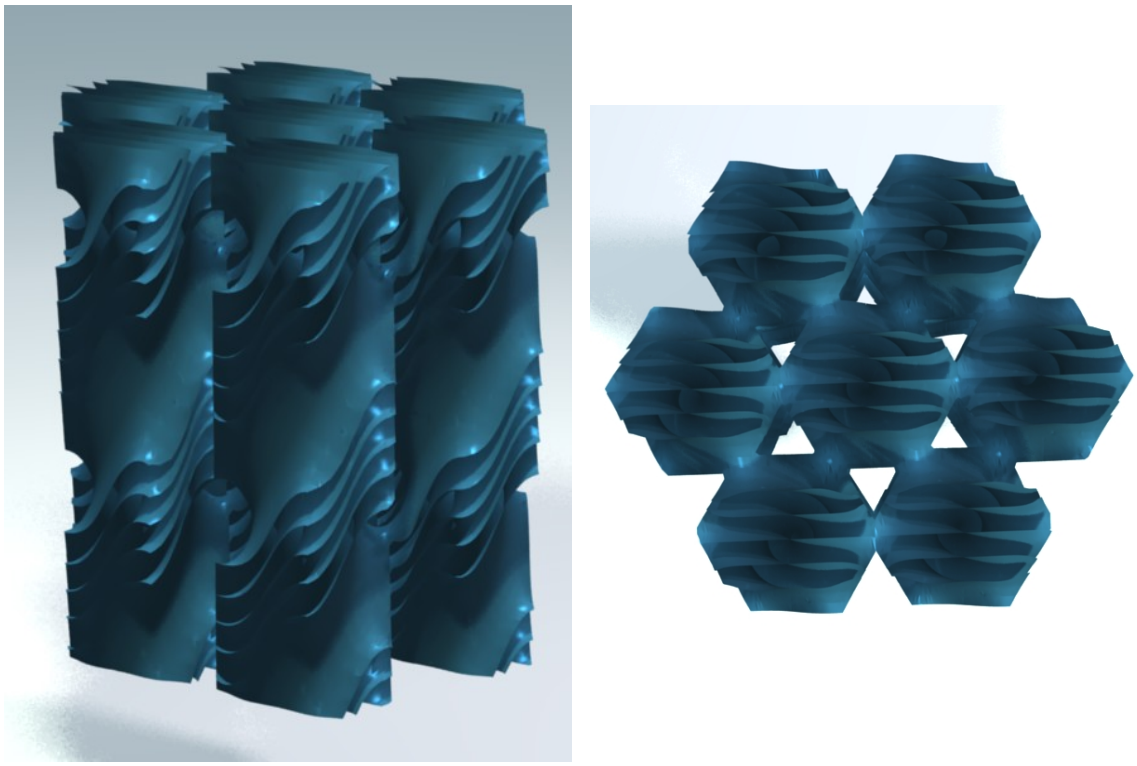

Figure 5.3: *left:* (Video online) In the bulk texture of the helical nanofilament phase, homochiral smectic bundles decorate the vertices of a hexagonal lattice. Each of the helical bundles has on average two defects corresponding to the divergence $\tilde{\Theta}_{\rm hex} \sim \zeta^{-1/2}$. *right:* Top view.

At these saddle points, we might expect the director field to deviate from the simple cholesteric form so as to more closely follow the layer normal, reducing the compression energy. Such screening effects are crucial near the lower critical chirality of the TGB [84] and should be included when the characteristic length scale of the structure is large compared to the penetration depth. However, both the compression and twist contributions are relevant to the free energy, suggesting that we expect $K_2 q_0^2 \sim B$ or equivalently $q_0 \lambda \gtrsim 1$. In the experiment $q_0 l \sim 1$ [46], suggesting that $l \lesssim \lambda$ so that neglecting screening effects should be

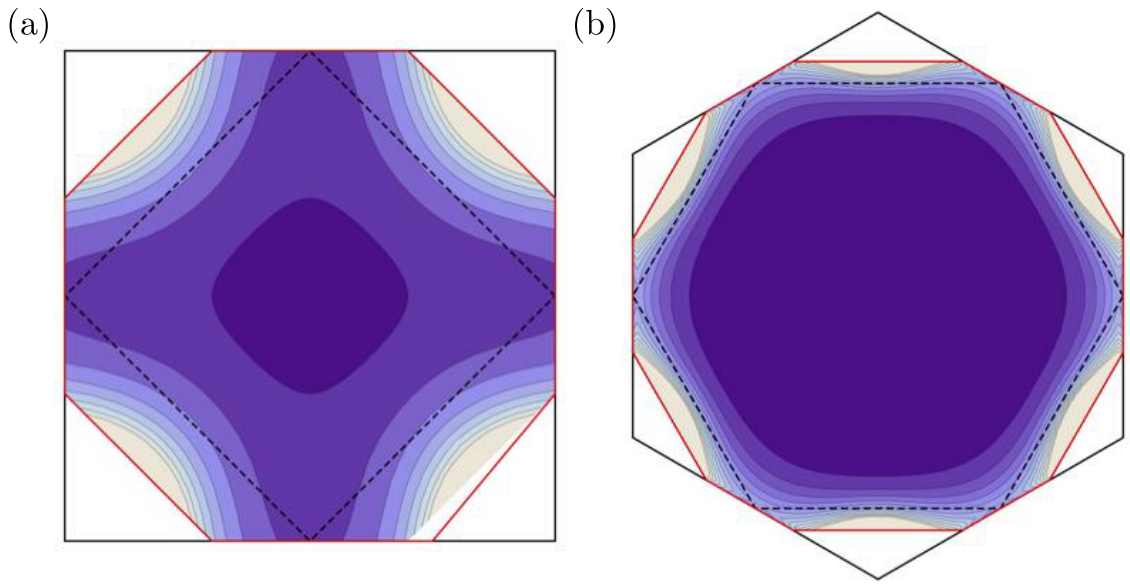

Figure 5.4: The contour plot of the compression energy density for single (a) square and (b) hexagonal unit cells. We approximate the region $\tilde{\Omega}$ where smectic order exists by the truncated hexagon bounded by the solid red line. Within the dashed black line the compression energy is well approximated by an expansion about the origin, while outside it an expansion about the singularities is used.

appropriate.

5.4 The Phase Diagram

Working in the London limit, the free energy per unit volume of the bulk texture becomes

$$\frac{F}{V} = \frac{2}{\sqrt{3}} \int_{\tilde{\Omega}} d^2\zeta \Big\{ \frac{B q_0^2 l^2}{4} |\tilde{\Theta}_{\text{hex}}|^2 + \frac{B}{2} \left| \partial_\zeta \tilde{\Theta}_{\text{hex}} - 1 \right|^2 - \frac{(t - t_c)^2}{u} \Big\}, \tag{5.21}$$

where $(t - t_c)^2/u$ is the condensation energy and we have integrated over the pitch direction and $\tilde{\Omega}$ is the non-dimensionalized domain (Fig. 5.4.b) in which smectic order is present. The compression energy diverges at singularities in $\tilde{\Theta}_{\text{hex}}$, forcing the smectic order to vanish, giving the bulk texture a porous appearance. The energy within the central region defined by the hexagon joining the midpoints between divergences is dominated by the Taylor expansion of $\tilde{\Theta}_{\text{hex}} = \zeta - \frac{|k|^6}{42\sqrt{3}}\zeta^7 + O(\zeta^{13})$ about the origin. Similarly, the energy near the defects is dominated by the Taylor series about the singularities $\tilde{\Theta}_{\text{hex}} = c(1 - i)\zeta^{-1/2} +$

$O(\zeta^{5/2})$, where $c = \frac{1}{2}3^{3/8}k^{-3/2} \approx 0.132$, leading to an energy per unit volume of

$$\begin{aligned}\frac{F}{V} &= B\Big[q_0^2 l^2\Big(\frac{5}{256} + c^2\cosh^{-1}(2)\big(1-2(1-\epsilon)^{1/2}\big)\Big) \\ &+ 0.052 + 6\sqrt{3}c^2\big((1-\epsilon)^{-1/2}-2\big)\Big] - \epsilon\frac{(t-t_c)^2}{u},\end{aligned} \tag{5.22}$$

where ϵ is the filling fraction and the result is valid in the regime where adjacent bundles overlap, $\epsilon \in [\frac{3}{4}, 1)$[2]. For the texture to be stable the divergence in the compression must not be more costly than the condensation energy. Assuming the coherence length is comparable to the layer spacing, $q_{\rm sm}\xi \sim 1$, then sets a hard upper bound for the filling fraction of $\epsilon < 0.91$. It follows that the regions of suppressed smectic order are substantial and occupy a finite fraction of the unit cell.

We note that the only dependence on the lattice constant in the free energy density, Eq. (5.21), is quadratic in l. Since the coefficient is positive definite, the energy expression would lead one to conclude that l should shrink to zero [3]. Of course the small-scale features will be cut off by microscopic length scales as well as additional energetic considerations. Recalling that bent-core mesogens favor layers with negative Gaussian curvature [46], we consider the saddle-splay of the individual layers as the bundle size shrinks: since the saddle-splay is the same as K [26], when the Frank constant $\bar{\kappa} < 0$ is negative, the system rewards the negative K everywhere in each layer. The Gauss-Bonnet theorem states that the integrated Gaussian curvature is purely a topological quantity. Thus, each layer in a bundle contributes the same free energy, $\frac{F_G}{V} \sim \frac{9}{16}\bar{\kappa}q_0^2$ for a filling fraction of $\epsilon = 3/4$. The lattice constant determines the maximum number of layers in a bundle, $n = \lfloor l/a \rfloor$. If l becomes too small for n layers, the system loses the free energy gain from the Gaussian curvature of that $n^{\rm th}$ layer. For experimental parameter values [4] and $\bar{\kappa}/B \sim (1\text{nm})^2$, the ideal bundles have diameter $d \sim 20$nm and contain 5 layers.

[2] The corresponding result for non-overlapping bundles, $\epsilon < \frac{3}{4}$, is given by retaining only the first and third terms in each of the square brackets, but reduced by factors of $(4\epsilon/3)^2$ and $(4\epsilon/3)^7$, respectively.

[3] A one-dimensional variational problem analogous to Eq. (5.21) is given by $I(u) = \int_a^b dx\big((|u_x|-1)^2+u^2\big)$ with $u(a) = u(b) = 0$. Similar to the well-known Bolza example, the infimum is given by the sequence of saw-tooth functions of decreasing period and height, and has $I \to 0$, although the minimum is not attained, see, e.g., [6].

[4] The authors of [46] measured a half-pitch of $q_0 \approx \pi/100$nm, layer spacing of 5nm, and helical bundles with 5 layers with a diameter of $25 \sim 30$nm.

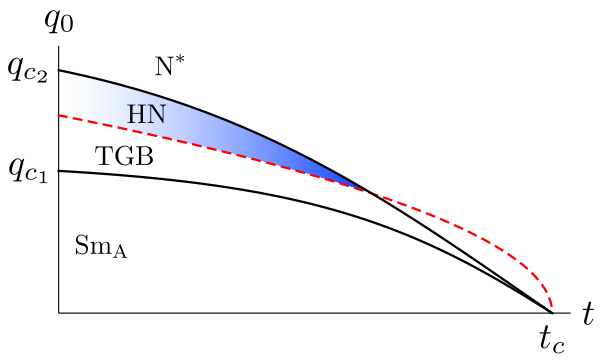

Figure 5.5: We show the schematic phase diagram for chiral smectics. The phase becomes unstable when the chirality exceeds $q_0 = \alpha/\lambda \sim |t_c - t|^{1/2}$ (dashed, red line). The phase transition to the HN phase occurs near the intersection between this line and the upper critical chirality q_{c_2}.

We can see directly from Eq. (5.22) that our bulk texture is energetically preferred over the smectic-A until a short distance below the thermodynamic critical chirality q_{th}, however its stability in relation to the TGB is less obvious. We focus on the region close to the upper critical chirality and argue that the TGB phase will lose stability relative to the HN phase for sufficiently large values of q_0. Within each grain of the TGB the compression energy locks the director to the local layer normal with a cosine potential, leading to a description for the twisting director field in terms of the infinite kink chain solution of the sine-Gordon model [71]. The width of the kinks (where the director rotates from one angle to the next) is set by the penetration depth λ. When the chirality is weak, $K_2 q_0^2 \ll B$, the separation between kinks l_b is large and the rotation is confined to narrow regions, whereas when the chirality is large, $K_2 q_0^2 \gg B$, the rotation occurs at an almost uniform rate, reminiscent of the cholesteric director. As the transition is mean field continuous the TGB structure must evolve towards that of the high temperature N^* phase as q_{c_2} is approached. In particular, we have that $\frac{\alpha}{l_b} \to q_0-$ and that the director field crosses over from the step-wise rotation usually envisaged for the TGB phase to the uniform rotation of the cholesteric. Within the framework of the sine-Gordon model of the TGB director, this crossover is marked by the overlap of kinks when $l_b \lesssim \lambda$. In this regime the energy per unit volume of the TGB swiftly

asymptotes to the value corresponding to having a cholesteric director field

$$\frac{F}{V} = -\frac{(t-t_c)^2}{u} + B\Big[1 - \frac{\sin(\alpha/2)}{\alpha/2}\Big] + B\frac{\sin(\alpha/2)}{q_{\rm sm} l_b}\ln\Big(\frac{l_d}{\xi}\Big), \tag{5.23}$$

where l_d is the spacing between screw dislocations within a grain boundary. As the chirality increases the constraint that $\frac{\alpha}{l_b} \to q_0-$ implies not only that the grain spacing l_b decreases but also that the rotation angle α should increase and we can expect the high chirality limit to correspond to $\alpha \to \frac{\pi}{2}$. For such large grain angles $l_d = \sqrt{2}a$ and the dominant energy cost is provided by the second term of Eq. (5.23), taking a value $\sim 0.099B$ that is larger than that of the HN phase. Thus for chiralites larger than $\sim \frac{\pi}{2\lambda}$ we expect the TGB phase to lose stability with respect to the HN phase, at least close to the upper critical chirality. The onset of the HN phase can be estimated from the intersection of the curves $q_0 = \frac{\pi}{2\lambda} \sim |t_c - t|^{1/2}$ and $q_0 = q_{c_2}(t) \sim |t_c - t|$ and hence should occur for $q_0 \gtrsim q_* = q_{\rm sm}(\frac{\pi\xi}{2\lambda})^2$, leading to the schematic phase diagram of Fig. 5.5.

5.5 Discussion

We have proposed a new chiral organization of a smectic liquid crystal which fills space. Like the blue phases, this phase is stable at high chirality and is built out of smaller building blocks, in this case helical nanofilaments. We find that the compression energy has an instability towards ever finer structure. The fine structure is cut off by considering the discrete nature of the layers and their Gaussian curvature. This explains the fine scale of the bundles seen in experiment, where each bundle is only a few layers thick [46]. Future work will examine the remarkable success of continuum theory despite the fact that the "long" lengthscales are comparable to the molecular size. We will explore the effects of order parameter variations and the deformations of the cholesteric texture.

Chapter 6

In Which We Encounter a Minimal Surface and a Pore is Opened

6.1 Free Energy, Smectic Topology and Minimal Surfaces

Smectics represent a particularly rich system for studying the interplay between geometry and topology. As smectics are a one-dimensional crystal of two-dimensional layers of liquid with equilibrium spacing $d = 2\pi/q_{\rm sm}$, it is apt to describe with a complex order parameter $\psi(\mathbf{x}) = |\psi_0(\mathbf{x})| \exp(-iq_{\rm sm}\Phi(\mathbf{x}))$. The magnitude of the order parameter, $|\psi_0(\mathbf{x})|$, determines whether or not smectic order is present. The phase of the smectic order parameter defines the smectic layers; this may be seen by considering the mass-density wave representation of the smectic, where layers are defined by level sets of the phase field $\Phi(\mathbf{x}) = nd$, $\forall\, n \in \mathbb{Z}$.

Topological defects in liquid crystals occur at points or lines where either the director field. The classification of such defects in nematics has a long tradition of studying the symmetries of the director field and the homotopy theory homotopy [83, 76, 49]. Unfortunately, smectics present a much more complex system, as the symmetries of the ground state define an orbifold and not a manifold [19]. Frequently, a study of the smectic free energy provides a new geometric angle to analyze smectic defects, bypassing the homotopic concerns.

The smectic free energy combines a Landau expansion in the complex smectic order parameter $\psi(\mathbf{x})$ and inherits the low energy distortions of the nematic phase field,

$$\begin{aligned} F_{\text{L-dG}} &= \int d^3\mathbf{x} \left[C|(\nabla - iq_{\rm sm}\mathbf{n})\psi|^2 + t|\psi|^2 + \frac{u}{2}|\psi|^4 + f_{\rm Frank} \right] \\ f_{\rm Frank} &= \frac{1}{2}\Big[K_1(\nabla\cdot\mathbf{n})^2 + K_2(\mathbf{n}\cdot\nabla\times\mathbf{n})^2 + K_3\big((\mathbf{n}\cdot\nabla)\mathbf{n}\big)^2 \Big], \end{aligned} \tag{6.1}$$

where $\mathbf{n}$ is the nematic director field which may deviate from the unit layer normal $\mathbf{N} = \nabla\Phi/|\nabla\Phi|$. Deep in the smectic A phase it is often valid to assume that the director field

is always parallel layer normal $\mathbf{n} = \mathbf{N}$. The last two terms in the Frank free energy are identically zero in this approximation because they violate the geometric condition $\nabla \times \mathbf{N} = 0$. The resulting free energy functional consists of two terms

$$F_{\mathrm{sm_A}} = \frac{1}{2} \int d^3x \Big(B \big| \nabla \Phi - \mathbf{n} \big|^2 + K_1 (\nabla \cdot \mathbf{n})^2 \Big), \tag{6.2}$$

where $B = 2Cq_{\mathrm{sm}}^2 \psi_0^2$ is the compression modulus; the compression term penalizes deviations of the layer spacing from the ideal spacing d and the bending term prefers smectic layers with zero mean curvature, $H = \frac{1}{2} \nabla \cdot \mathbf{N}$. The linear strain energy is rather unwieldy to work with because it is not an analytic function. Any nonlinear term may be used in its place as long as it respects the symmetries of the system and has the same linear approximation.

The effects of surface curvature and topological defects are inextricably linked. While it is simple to see how a single topological defect in a surface or family of surfaces induces curvature into its host, the converse problem is not trivial. Similarly, the addition of further defects into an already curved surface is not merely a superposition, nor are the interactions of a finite number of defects linear. However, the topology of the surfaces themselves provides a framework for studying the collective effects of curvature and topological defects. A deep theorem in differential geometry states that all minimal surfaces are built out of pieces of helicoids and catenoids [23].

An explicit deconstruction of surfaces into their topological constituents will provide a unique language with which to describe the properties of many diverse systems. Extracting the underlying topology of a surface boils down to an exercise in complex analysis. Linear systems often produce harmonic surfaces which possess height functions satisfying the two dimensional Laplace equation. Elliptic functions, generalizations of trigonometric functions, are the generic solutions of this problem. Merely specifying the zeroes and poles in a phase field completely defines the topology of the resulting surface. The properties of elliptic functions vastly simplify both the analytic and numeric calculations of the energy.

6.2 Riemann's Minimal Surface

Riemann's minimal surface is foliated by circles, thus it may be described by a phase field of the following form:

$$\Phi = \big(x - \alpha(z)\big)^2 + \big(y - \beta(z)\big)^2 - R^2(z). \tag{6.3}$$

A minimal surface must satisfy the condition: $\mathrm{H} = \frac{1}{2}\,\nabla \cdot \mathbf{n} = 0,$ where $\mathbf{n} = \nabla\Phi/|\nabla\Phi|$, that it have zero mean curvature everywhere.

6.2.1 Weierstrass elliptic functions

Following Nitsche [80], the phase field must satisfy:

$$\left(\frac{\Phi_z}{R^2}\right)_z + \frac{2}{R^2} = 0. \tag{6.4}$$

From which it follows that R^2 satisfies

$$\Big[\big(R^2(z)\big)'\Big]^2 = 4\Big[(a^2+b^2)\,R^6(z) + 2\,c\,R^4(z) - R^2(z)\Big] \tag{6.5}$$

and, similarly, $\alpha'(z) = a\,R^2(z)$ and $\beta'(z) = b\,R^2(z)$. By considering solutions of the form $R^2(z) = A\,f(z) + B$, equation (6.5) becomes the familiar equation for the Weierstrass $\wp$-function, $\big(\wp'(z)\big)^2 = 4\,\wp^3(z) - g_2\,\wp(z) - g_3 = 4\,\big(\wp(z) - e_1\big)\big(\wp(z) - e_2\big)\big(\wp(z) - e_3\big)$, where $e_1 + e_2 + e_3 = 0$. We obtain the following solution for $R^2(z)$:

$$R^2(z) = \frac{\wp\big(z, \{g_2, g_3\}\big) - 2\,c/3}{a^2 + b^2}, \tag{6.6}$$

where $g_2 = 4(a^2 + b^2 + \frac{4}{3}c^2)$ and $g_3 = -\frac{8}{3}\,c\,(a^2 + b^2 + \frac{8}{9}c^2)$ are the Weierstrass invariants. For reference, the half-period values are

$$\begin{aligned} e_1 &= \wp(\omega_1/2) = -\frac{c}{3} + \sqrt{a^2+b^2+c^2} \\ e_2 &= \wp(\omega_1/2 + \omega_3/2) = \frac{2}{3}\,c \\ e_3 &= \wp(\omega_3/2) = -\frac{c}{3} - \sqrt{a^2+b^2+c^2}, \end{aligned} \tag{6.7}$$

for $c < 0$. Without loss of generality, we set $a = 0$, as this merely fixes the free rotations about the $z-$axis.

6.2.2 Jacobi elliptic functions

It behooves us to work with Jacobi elliptic functions for the remainder of this chapter. Jacobi elliptic functions are doubly periodic with real period $2\,K(m)$ and imaginary period $4\,i\,K(1-m)$, where m is the square of the elliptic modulus and $K(m) = \int_0^{\pi/2} \frac{dt}{\sqrt{1-m\,\sin^2(t)}}$ is the complete elliptic integral of the first kind. To convert between the two equivalent representations of elliptic functions, Weierstrass and Jacobi, we use the identity:

$$\wp(z) = e_3 + (e_1 - e_3)\,\mathrm{ns}^2(z\,\sqrt{e_1 - e_3}, m), \tag{6.8}$$

where $m = (e_2 - e_3)/(e_1 - e_3)$[1]. Therefore, in terms of Jacobi functions, equation (6.6), the square of the radius is,

$$R^2(z) = \frac{e_3 - e_2 + (e_1 - e_3)\mathrm{ns}^2(z\sqrt{e_1 - e_3}, m)}{b^2} = \frac{e_1 - e_3}{b^2}\big(\mathrm{ns}^2(\sigma z, m) - m\big) = \frac{\sigma^2}{b^2}\mathrm{ds}^2(\sigma z, m), \tag{6.9}$$

where $\sigma^2 := e_1 - e_3 = 2\sqrt{b^2 - c^2} = b/\sqrt{m(1-m)}$, and we have used the identity $\mathrm{dn}^2(z,m) + m\,\mathrm{sn}^2(z,m) = 1$, and the integral defining the center of the circles is

$$\int dz\,\mathrm{ds}^2(z,m) = z(1-m) - \frac{\mathrm{cn}(z,m)\mathrm{dn}(z,m)}{\mathrm{sn}(z,m)} - E\big(\mathrm{am}(z,m), m\big), \tag{6.10}$$

where $E(z,m) = \int_0^z dt\sqrt{1 - m\sin^2 z}$ is the incomplete elliptic integral of the second kind. Note that the integral $E\big(\mathrm{am}(z,m), m\big)$ is composed of a linear part, $z\,\frac{E(m)}{K(m)}$, and a periodic part, $Z\big(\mathrm{am}(z,m), m\big)$. In terms of the Jacobi elliptic functions, the phase field is

$$\Phi = x^2 + \left(y - \frac{\sigma}{b}\Big(\tilde{z}(1-m) - E\big(\mathrm{am}(\tilde{z},m), m\big) + \mathrm{cs}(\tilde{z},m)\mathrm{dn}(\tilde{z},m)\Big)\right)^2 - \frac{\sigma^2}{b^2}\mathrm{ds}^2\big(\tilde{z}, m\big) = 0, \tag{6.11}$$

where $\tilde{z} := \sigma z$. Since σz is merely a rescaling of the z-axis, we have the freedom to choose the constant $\sigma = 2K(m)/d$ to ensure that the periodicity of the phase field matches the ideal spacing of the smectic layers d. The final parameter $b = 4K(m)^2\sqrt{m(1-m)}$ may now be expressed in terms of the elliptic modulus. The resulting surface is now a one-parameter

[1] We use the standard Glaisher convention for notation $\mathrm{pq}(z,m) = \frac{\mathrm{pr}(z,m)}{\mathrm{qr}(z,m)}$, where p, q, and r can be any of the following s, c, d, or n and $\mathrm{ss} = \mathrm{cc} = \mathrm{dd} = \mathrm{nn} = 1$. For example, $\mathrm{cs}(z,m) = \frac{\mathrm{cn}(z,m)}{\mathrm{sn}(z,m)}$.

family of surfaces, depending on $m \in [0,1]$.

As there are an infinite number of phase fields that describe the same surface, determining the appropriate representation of the phase field for each given application requires careful consideration. First, we demonstrate that Riemann's minimal surface is composed topologically of two screw dislocations of opposite handedness, and, secondly, we find the most convenient form to be used with the smectic free energy. Expanding the square in y in the phase field we get:

$$\Phi = x^2 + \big(y - \zeta(\tilde{z},m)\big)^2 + 2\frac{\sigma}{b}\big(y-\zeta(\tilde{z},m)\big)\,\mathrm{cs}(\tilde{z},m)\,\mathrm{dn}(\tilde{z},m) - \eta^2(\tilde{z},m) = 0, \qquad (6.12)$$

where we define $\zeta(z,m) := \frac{\sigma}{b}\big(z(1-m) - E\big(\mathrm{am}(z,m),m\big)\big)$, and $\eta^2(z,m) := \frac{\sigma^2}{b^2}\big(\mathrm{ds}^2(z,m) - \mathrm{cs}^2(z,m)\mathrm{dn}^2(z,m)\big) = \frac{\sigma^2}{b^2}\mathrm{dn}^2(z,m)$. After a little algebra, we find an equivalent phase field:

$$\Phi = 1 + \frac{\big(y-\zeta(\tilde{z},m)\big)^2}{x^2-\eta^2(\tilde{z},m)} - \left(\frac{y-\zeta(\tilde{z},m)}{x+\eta(\tilde{z},m)} - \frac{y-\zeta(\tilde{z},m)}{x-\eta(\tilde{z},m)}\right)\frac{\sigma\mathrm{cs}(\tilde{z},m)\mathrm{dn}(\tilde{z},m)}{b\,\eta(\tilde{z},m)} = 0. \qquad (6.13)$$

From this we find a relation between y, $\tilde{z}$, and x

$$\frac{\frac{y-\zeta(\tilde{z},m)}{x+\eta(\tilde{z},m)} - \frac{y-\zeta(\tilde{z},m)}{x-\eta(\tilde{z},m)}}{1 + \frac{y-\zeta(\tilde{z},m)}{x+\eta(\tilde{z},m)}\,\frac{y-\zeta(\tilde{z},m)}{x-\eta(\tilde{z},m)}} = \mathrm{sc}(\tilde{z},m), \qquad (6.14)$$

where we note that the definition of $\mathrm{sc}(z,m) = \sin(\mathrm{am}(z,m))/\cos(\mathrm{am}(z,m))$. Taking the arctangent of both sides and rearranging the terms yields a phase field of the form:

$$\Phi = \mathrm{am}(\sigma z,m) + \tan^{-1}\left(\frac{y-\zeta(\sigma z,m)}{x-\eta(\sigma z,m)}\right) - \tan^{-1}\left(\frac{y-\zeta(\sigma z,m)}{x+\eta(\sigma z,m)}\right) = 0, \qquad (6.15)$$

which is clearly a nonlinear sum of two helicoids of opposite handedness. The cores of the defects are located at $x = \pm\eta(\sigma z,m)$, $y = \zeta(\sigma z,m)$, where $\zeta(\sigma z,m)$ consists of a linear component with a periodic term superimposed upon it, and $\eta(\sigma z,m)$, is a periodic function with maximum at $\eta(0,m) = \sigma^2/b^2$ and miniumum at $\eta(K(m),m) = \sigma^2/b^2\sqrt{1-m}$.

We want to have flat evenly spaced layers at infinity. Thus the phase field must be normalized such that the compression energy vanishes, or $\lim_{x,y\to\infty}\big((\nabla\Phi)^2 - 1\big)^2 = 0$. Since the derivative $\partial_z \mathrm{am}(z,m) = \mathrm{dn}(z,m)$ is not independent of z, this phase field does not satisfy the energetic requirements. One final manipulation, based on the identity $F\big(\mathrm{am}(z,m),m\big) = 0$, where $F(z,m) = \int_0^z dt(1-m\sin^2 t)^{-1/2}$ is the incomplete elliptic

integral of the first kind, gives the phase field

$$\Phi = z + \frac{1}{\sigma} F\left[\tan^{-1}\left(\frac{y-\zeta(\sigma z,m)}{x-\eta(\sigma z,m)}\right) - \tan^{-1}\left(\frac{y-\zeta(\sigma z,m)}{x+\eta(\sigma z,m)}\right), m\right] = 0. \tag{6.16}$$

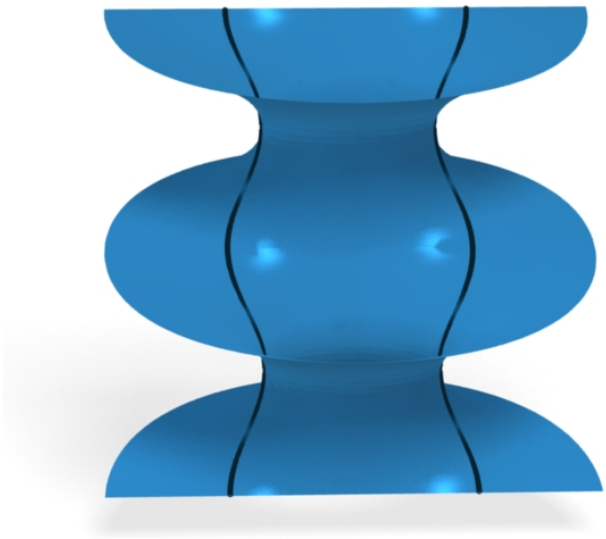

Figure 6.1: (Video online) Riemann's minimal surface, shown here with elliptic modulus m=0.5, is composed of two helices whose cores (shown in black) are linear with a superimposed periodic modulation.

6.3 Pores and Defect Cores

Riemann's minimal surface is a one parameter family of surfaces. As the control parameter $m \in [0,1]$ sweeps through all allowed values the morphology of the surface changes as the defect cores undergo a transformation. In the limit that $m \to 0$, the defect cores are straight and infinitely far apart. However, as m increases, the distance of closes approach between the two cores decreases. If the layers are to remain flat along the boundary at infinity, the cores must bend. Conversely, two straight screw dislocations in a smectic will force the layers to bend. The amplitude of the distortion of the cores also must increase as m increases. The topological character of straight screw dislocations is preserved even though the cores of the dislocations possess curvature. The line integral of the director field around a closed loop encircling a defect, $\oint \mathbf{n} \cdot d\mathbf{l} = \pm d$, remains constant regardless of the

position or orientation of the core.

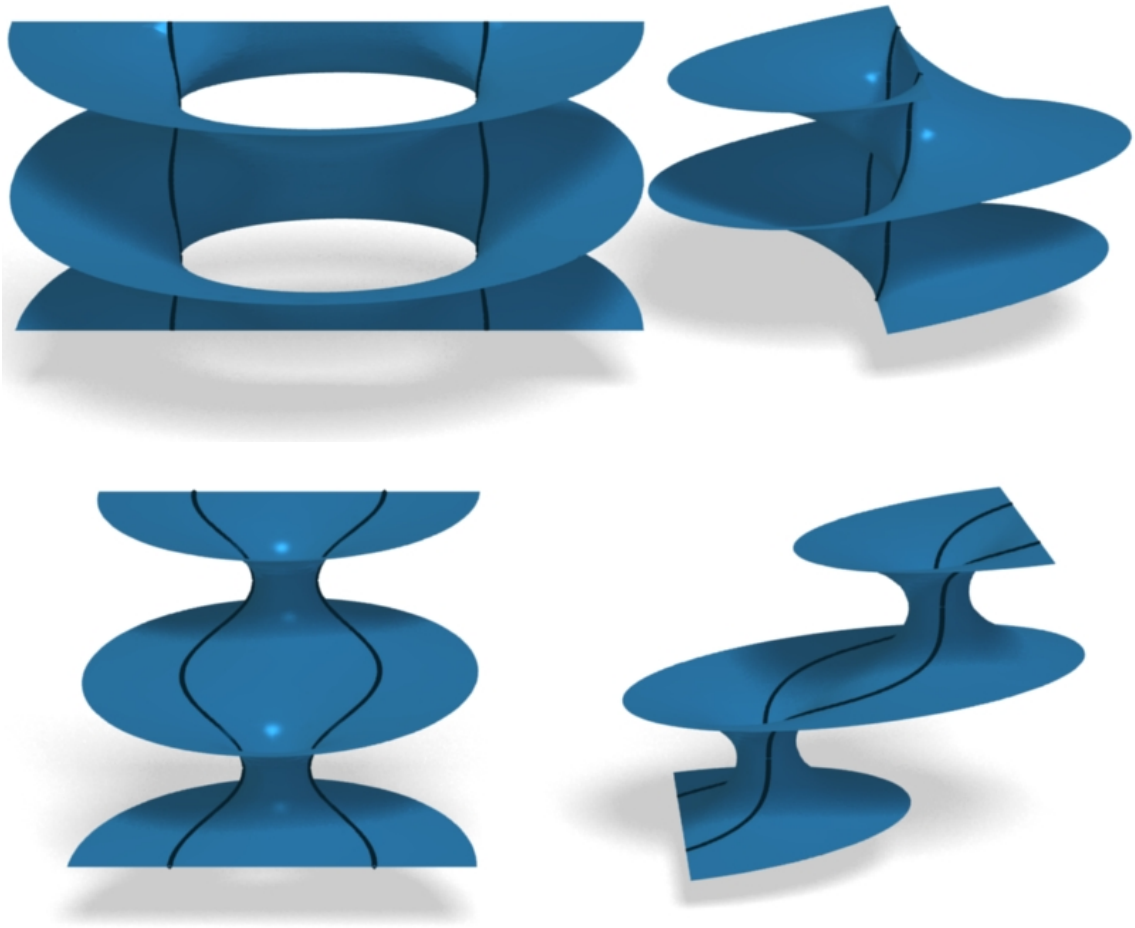

Figure 6.2: (Video online) Riemann's minimal surface evolves from two oppositely handed helicoids that are infinitely far apart at $m = 0$ to a single infinitely thin pore located at the origin at $m = 1$. Shown here from two perspectives is the transformation of the surface for two values of the control parameter, $m = 0.05$ (top) and $m = 0.95$ (bottom).

Although the topology of the minimal surface is that of two oppositely handed helicoids, the construction via foliation of circles implies that layers occur when the radius approaches infinity and that adjoining layers are connected by necks. By varying the surface parameter through the range $m \in [0, 1]$, Riemann's minimal surface transforms between these two morphologies, as seen in Figure 6.2.

6.4 Discussion

Nowhere is the "duality" between the two topological descriptions of Riemann's minimal surface more important than in the energetics. By choosing the helicoidal description of the phase field, the divergences in the energetics lie along the defect cores. Here the smectic layers are flat and evenly spaced at the boundary at infinity. Conversely, a smectic containing a pore will have curvature singularities down the center of the pore and at infinity, reminiscent of the focal lines in the focal conic texture.

This simple example highlights the importance of topological decomposition of minimal surfaces in studying complex systems in nature. Enumerating all topological defects in a surface simultaneously identifies all energetic singularities. This technique will help to explain a variety of phenomena, in particular, triply periodic minimal surfaces which appear in bicontinuous cubic phases of systems ranging from mitochondrial membranes to the dark conglomerate phase of bent core liquid crystals to binary metallic alloys. The network of defects recovered from a topological decomposition will explain both their extraordinary stability and complex phase diagram. By tuning the interfacial preference for negative Gaussian curvature, the cubic phases continuously transform into one another following the progression Schwarz P surface to diamond surface to gyroid. Yet simple curvature considerations cannot explain this series of surfaces. Although these surfaces are topologically distinct, tracking the evolution of the lattice of their defects will elucidate the means by which these surfaces smoothly change topology.

Chapter 7

In Which Equal Spacing is Enforced and We Shed Light on Focal Conic Domains

In equally-spaced layered systems, such as smectics, idealized flat layers are rarely realized while textures permeated with focal conic domains are prevalent [34, 11, 61]. They are beautiful and geometrically precise conic sections that are observed to occur in pairs of perfect confocal partners and with adjacent domains often exhibiting a more widespread level of geometric organization as in Friedel's law of corresponding cones [34, 60], the *treillis et réseaux* expounded by Bouligand [11], or Apollonian packings [9]. Since purely topological considerations are far too pliable to produce this level of geometric precision, focal conics must arise from a more rigid form of constraint; indeed, prior even to the knowledge of their molecular nature, it was realized that they are governed by the criterion of equal layer spacing [34]. The condition of equal spacing, though an idealization, is a boon to the description of smectics, since it enables the form of the layers throughout the entire system to be determined uniquely [90], for instance from their focal sets. In this chapter we describe a hidden symmetry that underlies the structures of focal conics by viewing domains in d-dimensions, $\mathbb{R}^d$, as level sets of hypersurfaces in $d+1$-dimensional Minkowski space, $\mathbb{R}^{d,1}$. In this framework, the equal spacing constraint is equivalent to the condition that the hypersurfaces are lightlike, or *null*. Lorentz transformations, by their very construction, preserve the null condition; the level sets, however, are changed, giving rise to different domain geometries, which nonetheless arise from the same hypersurface.

We quickly recall the symmetries and free energy of the smectic liquid crystal phase. The smectic phase is characterized by a one-dimensional density wave, $\rho(\mathbf{x}) = \rho_0 + \rho_1 \cos\left[\frac{2\pi\phi(\mathbf{x})}{a}\right]$, where the level sets $\phi(\mathbf{x}) = na$, $n \in \mathbb{Z}$, with a the layer spacing, define smectic layers with unit normal $\mathbf{N} = \nabla\phi/|\nabla\phi|$. The ground state consists of equally spaced, flat layers, and

the free energy is

$$F = \frac{1}{2}\int d^d x \left\{ \frac{B}{4}\left[(\nabla\phi)^2 - 1\right]^2 + K\left(\nabla\cdot\mathbf{N}\right)^2 \right\}, \tag{7.1}$$

where the first term, the compression, controls the spacing and the second the mean curvature of the lamellae. Twist modes are expelled *à la* the Meißner effect [24]. The energy is invariant under $\phi \to \phi + \text{constant}$, and $\mathbf{N} \to -\mathbf{N}$. The former symmetry represents a constant displacement of the smectic layers, but we see that $\phi \to \phi + a$ is merely a reparameterization of the density; likewise the nematic symmetry implies that $\nabla\phi \to -\nabla\phi$ results in precisely the same density wave, or equivalently $\phi \to -\phi$. It follows that $\phi \in S^1/\mathbb{Z}_2$. In this Letter we will focus on configurations with vanishing compression.

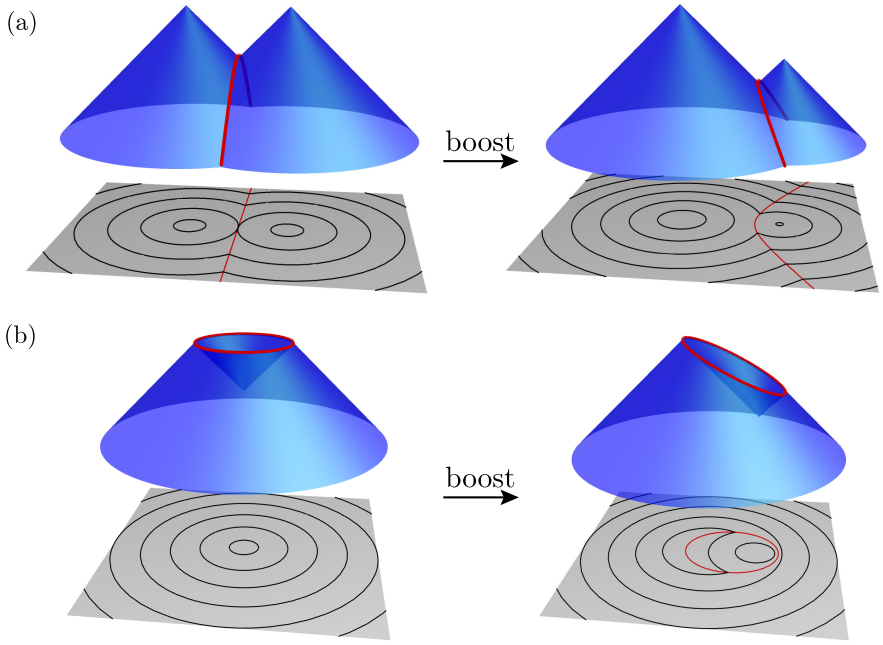

Figure 7.1: Achronal boundaries for (a) a pair of space-like and (b) time-like separated events, both in their rest frames (left) and in a general frame (right). The corresponding smectic textures are shown below each surface, with focal lines indicated in red.

Deferring the full symmetries of ϕ momentarily and instead working in the universal cover, $\mathbb{R}$, we recall that as the phase field associates a real number to every point $\mathbf{x}$ in the material, it is convenient to consider this as the coordinate of an extra dimension and view the smectic as a surface $\big(\mathbf{x}, \phi(\mathbf{x})\big)$ in this larger space [19]. Equally spaced structures, which correspond to focal conic domains, play a privileged role. Examples of equally spaced

smectics include the ground state $\phi = x$, say, where the surface is a plane, and the point defect $\phi = |\mathbf{x}|$, where the surface is a right circular cone. Writing this last example instead as $|\mathbf{x}|^2 - \phi^2 = 0$ affords a more useful interpretation: the surface is the light cone of an event in Minkowski space (with $c = 1$), with the value of the phase field viewed as a time-like direction. Importantly this correspondence is entirely general, as the condition of being null corresponds exactly to moving a unit distance in space for every unit change in ϕ, thereby ensuring equal spacing. Moreover, since Lorentz transformations preserve null hypersurfaces *a fortiori*, focal conics also inherit this symmetry [1]. Defining, according to tradition, β as the boost "velocity" and $\gamma = (1 - \beta^2)^{-1/2}$, the Lorentz transformation is $x' = \gamma(x - \beta\phi)$, $y' = y$, and $\phi' = \gamma(\phi - \beta x)$ [64, 30]. We also bring the reader's attention to the fact that the symmetries relating different textures do not act on ϕ alone, but on a larger space [2]. Just as a cube can cast a square, rectangular, or hexagonal shadow, so too do different "projections" of the same surface lead to different smectic textures, revealing an underlying universal structure: namely the same null hypersurface, just viewed by different "observers."

A general null hypersurface will exhibit points of "singularity," like the apex of the light cone, through which multiple light rays pass. These points correspond to the focal sets of the smectic and provide the most convenient way of describing the texture. It is precisely at these points that the projection of the surface normal is ill-defined, corresponding to disclinations and kinks in the nematic director, normal to the smectic layers. To construct the null hypersurface corresponding to any focal conic texture, it suffices to specify all of its focal sets. However, without prior knowledge of their form, the general case would seem a daunting task. Insight can be gained by first considering a class of null hypersurfaces whose focal sets form a dual pair. Not only does this immediately produce the precise shapes seen

[1] Note that Lorentz covariance is a symmetry of the smectic texture not shared by the free energy functional.

[2] The formal procedure is a sequence of maps:

$$\mathbb{R}^d \xrightarrow{\Phi} \mathbb{R}^{d,1} \xrightarrow{\pi\circ\Lambda_\beta} \mathbb{R}^d \times \mathbb{R} \xrightarrow{(1,\tau)} \mathbb{R}^d \times \left(S^1/\mathbb{Z}_2\right)$$

The first generates a null hypersurface, upon which act Lorentz transformations Λ_β. To then construct a smectic texture consistent with the symmetries of a density wave we fix a frame to return from Minkowski to Euclidean space using a map π that takes $(x, \phi) \in \mathbb{R}^{d,1}$ to $(x, \phi) \in \mathbb{R}^d \times \mathbb{R}$, and subsequently project the former time coordinate ϕ to a phase in $S^1/\mathbb{Z}_2$.

experimentally, but it also yields a natural generalization to multiple domain configurations that again captures the experimental features.

Consider a pair of events in $\mathbb{R}^{2,1}$, which generate two-dimensional focal conics through the intersection of their light cones as shown in Fig. 7.1. As is well known, a pair of events are either space-like, time-like, or null separated. Space-like separated events have coordinates $(\pm r, 0, 0)$ in their preferred or "rest" frame and the intersection of their light cones occurs on the hyperbola $y^2 - \phi^2 = -r^2$, in the $x = 0$ plane. In a general frame, obtained by a boost along the x-direction, the two events lie at $(\pm\gamma r, 0, \mp\gamma\beta r)$, and the intersection of their light cones becomes $y'^2 - (\phi'/\gamma)^2 = -r^2$, $x' = -\beta\phi'$. The smectic layers are given by equal time slices ($\phi' = na$) of the null hypersurface formed by the two light cones. These are circles, or arcs of circles, concentric about $(x', y') = (\pm\gamma r, 0)$ that are the vertical projections of the two events and the foci of one branch of the projected hyperbola $(x'/\gamma\beta)^2 - y'^2 = r^2$, along which there are cusp singularities - precisely the focal lines seen in cross sections of three-dimensional textures.

An identical analysis can be given for two time-like separated events, which in their preferred frame have coordinates $(0, 0, \pm r)$ leading to an intersection of their light cones on the circle $x^2 + y^2 = r^2$ in the $\phi = 0$ plane. Boosting to a general frame as before, the two events take the coordinates $(\mp\gamma\beta r, 0, \pm\gamma r)$, while their conjugate focal set becomes $(x'/\gamma)^2 + y'^2 = r^2$, $\phi' = -\beta x'$, the equation of an ellipse. Again the projections of the two events coincide with the foci of the ellipse. The final case of null separation between the events is exceptional and we defer its treatment for the time being.

In general, focal conics may be defined by their focal sets; for two space-like separated events these sets are $\Sigma = \{x^2 = r^2; y = \phi = 0\}, \overline{\Sigma} = \{y^2 - \phi^2 = -r^2; x = 0\}$, while for two time-like separated events they are $\Sigma = \{x^2 + y^2 = r^2; \phi = 0\}, \overline{\Sigma} = \{-\phi^2 = -r^2; x = y = 0\}$. In both cases these sets are mutually null separated and lie in orthogonal subspaces. In higher dimensions this simple decomposition persists and the focal sets take the form $\Sigma = \{x^2 + \vec{y}^2 = r^2; \vec{z} = \phi = 0\}, \overline{\Sigma} = \{\vec{z}^2 - \phi^2 = -r^2; x = \vec{y} = 0\}$, where $\vec{y}$ and $\vec{z}$ are k- and $(d-k-1)$-dimensional vectors, respectively, with $k \in \{0, 1, .., d-1\}$. This classification of these null hypersurfaces corresponds with those described by Friedlander as being associated

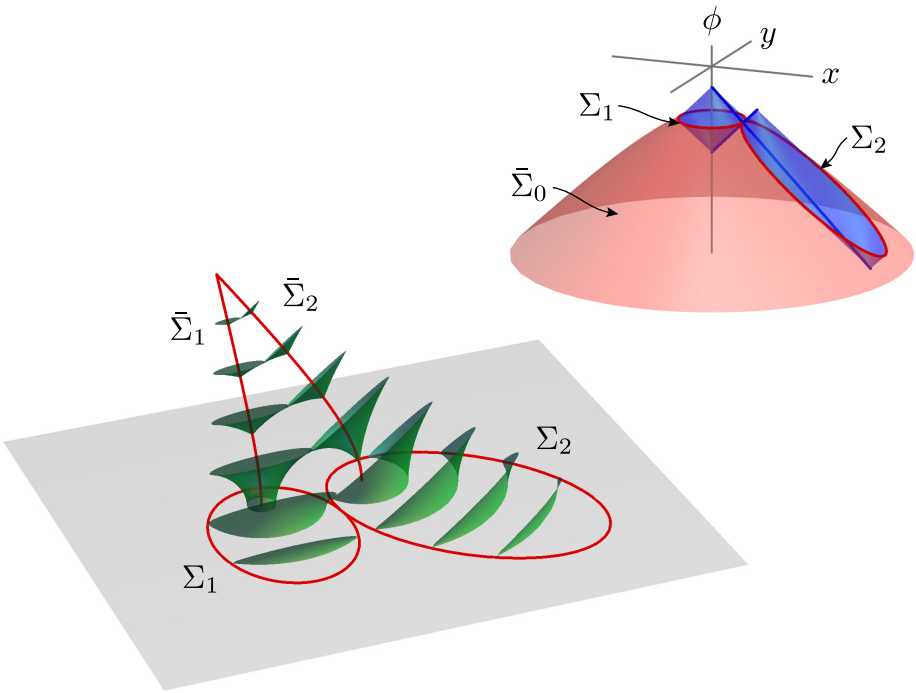

Figure 7.2: Two Dupin cyclide domains sharing a point of tangency in a trellis configuration. The cyclides fill conical regions extending from the point of intersection of their hyperbolae to their focal ellipse, while outside these regions the layers are continued by concentric spheres. In Minkowski space (inset, $z = 0$ subspace) the ellipses lie on the surface of an hyperboloid. Tangency of ellipses corresponds to null separation of their foci, as is most easily seen in the rest frame of one of the ellipses.

with progressive wave solutions of the wave equation [35]. As we shall see they serve as the building blocks for focal conic textures. The limiting cases $k=0$ and $k=d-1$ reduce to a pair of space-like and time-like separated events, respectively. In three dimensions there is only one other possibility, namely $k=1$ where the focal sets are both one-dimensional and correspond to a circle and an hyperbola lying in orthogonal subspaces. These are the elliptic-hyperbolic focal conic domains, which give smectic layers that are confocal cyclides of Dupin [34, 11, 61, 14, 75]. Splitting $R^{3,1}$ into two orthogonal subspaces is equivalent to Maxwell's double canal surface construction [75].

A null hypersurface S can be constructed from the focal sets as the union of all light rays connecting $e \in \Sigma$ to $\overline{e} \in \overline{\Sigma}$; $S = \{p = (e+\overline{e})/2 + \xi(e-\overline{e})/2, \xi \in I_e^{\overline{e}}\}$ where $I_e^{\overline{e}}$ is a connected interval of $\mathbb{R}$ depdending on e and $\overline{e}$. For the confocal hyperbola and ellipse, an explicit representation of S follows from the form of the focal sets [35] $[(s+r)^2 + z^2 -$

$\phi^2][(s-r)^2+z^2-\phi^2]=0$, where $s\equiv\sqrt{x^2+y^2}$ is the radius in cylindrical coordinates, (s,θ,z,ϕ). This is precisely Cayley's quadric expression [14] in its "rest frame", and thus reveals that the Dupin cyclides are a "product of two cones." Note that there is no need to consider different cyclides or different types of elliptic-hyperbolic focal domains as they are all given by the same null hypersurface: one need only exploit Lorentz transformations and take different time slices. However, it is important to make the distinction between the propagation of light and smectic layers. In the former, the wavefronts can pass through each other, while in the latter they cannot. As shown in Fig. 1, for instance, this means that once the cones intersect the null hypersurface ends on this lower-dimensional cusp. In the parlance of general relativity, such surfaces are known as achronal boundaries [41]. In general, for those light rays originating from a point $\overline{e}$ of $\overline{\Sigma}$ with $\phi<0$ we take $I_e^{\overline{e}}=[-1,1]$, while for points with $\phi>0$ we take $I_e^{\overline{e}}=[1,\infty)$. Note that y and z may be replaced with $\vec{y}$ and $\vec{z}$ without change to the foregoing discussion [55].

Elliptic-hyperbolic focal domains arise from a decomposition of Minkowski space into a pair of orthogonal subspaces, one space-like and one time-like, leading to focal sets that are spheres of square radius $\pm r^2$, one in each subspace. The only other construction of this kind is a decomposition of Minkowski space into a pair of orthogonal null subspaces. Denoting by $u_\pm$ the affine distances along the null directions $(1,0,0,\pm1)$, we can take the null subspaces to be the u_+y and u_+z planes, separated by a distance σ along the u_- direction. One may swiftly verify that the sets $\Sigma=\{4\sigma u_++y^2=0;\, u_-=\sigma/2, z=0\}$ and $\overline{\Sigma}=\{-4\sigma u_++z^2=0;\, u_-=-\sigma/2, y=0\}$ are null separated and thus serve as the focal sets for a null hypersurface, S, this time corresponding to a parabolic focal conic. Again these coincide with Friedlander's classification of progressing waves [35].

Although single focal domains correspond to null hypersurfaces in Friedlander's classification of progressive waves, this correspondence does not carry over to textures with more than one focal domain. Here we are tasked with the question of how to appropriately adjoin separate domains to form a larger structure, a task for which the Lorentzian viewpoint provides a convenient perspective. We provide two illustrative examples.

First, we consider the trellis configurations and Friedel's law of corresponding cones [34].

This is a collection of cyclidal domains organized so that their hyperbolae all intersect at a pair of points, as implied in Fig. 7.2. In Minkowski space these points of intersection represent a pair of space-like separated events, which, as we have seen, exhibit a conjugate focal set that is a hyperboloid (cf Fig. 7.1). Friedel's laws are simply the statement that the ellipses of the individual cyclidal domains all lie on this hyperboloid. Concretely, denoting the pair of events by $\Sigma_0 = \{z^2 = R^2;\, x = y = \phi = 0\}$, the conjugate hyperboloid is $\overline{\Sigma}_0 = \{x^2+y^2-\phi^2 = -R^2;\, z=0\}$. Observe that the focal sets $\Sigma_1 = \{x^2+y^2 = r^2; \phi = -\sqrt{r^2+R^2}, z = 0\}, \overline{\Sigma}_1 = \{z^2-(\phi+\sqrt{r^2+R^2})^2 = -r^2; x = y = 0\}$, are cyclidal domains, exhibiting the desired nesting $\Sigma_1 \subset \overline{\Sigma}_0$, $\overline{\Sigma}_1 \supset \Sigma_0$, so that the focal ellipse of this domain lies on the surface of the hyperboloid $\overline{\Sigma}_0$, while the focal hyperbola passes through the original pair of events, Σ_0. Importantly, this is preserved by Lorentz transformations and since these act transitively on $\overline{\Sigma}_0$ they in fact generate all focal sets $(\Sigma_1, \overline{\Sigma}_1)$ with this property.

The null hypersurface for the composite texture is formed by taking the surface for the concentric sphere domain and omitting those light rays connecting Σ_0 to the part of $\overline{\Sigma}_0$ inside the circle Σ_1. These are then replaced by light rays connecting Σ_1 to $\overline{\Sigma}_1$. In this way the excised region of the concentric sphere domain is filled with the cyclides of Dupin [90] and because the interface consists of the same light rays, both the smectic layers and the layer normal are continuous across the join. Of course, this construction can be repeated for a collection of focal domains $\{\Sigma_i, \overline{\Sigma}_i\}_{i=1}^N$ to yield a trellis structure [11]. Tangency of adjacent ellipses corresponds to their foci being null separated with the light rays connecting them passing through their common point, as is readily apparent when viewed from one of their rest frames (Fig. 7.2). When projected into $\mathbb{R}^d$ this is Friedel's observation that straight lines can be drawn between the foci of touching domains that pass through their point of tangency [34].

Tilt-grain-boundaries [9, 60, 10] involve a similar replacement of a region of one type of texture with that of another, and again this can be conveniently achieved by working in the appropriate rest frame. In this instance, one removes a cylindrical region of the ground state and fills it with the inner part of a cyclide domain. This cyclide region is described by those light rays connecting the elliptical focal set $\Sigma = \{x^2+y^2 = r^2;\, z = \phi = 0\}$ to the

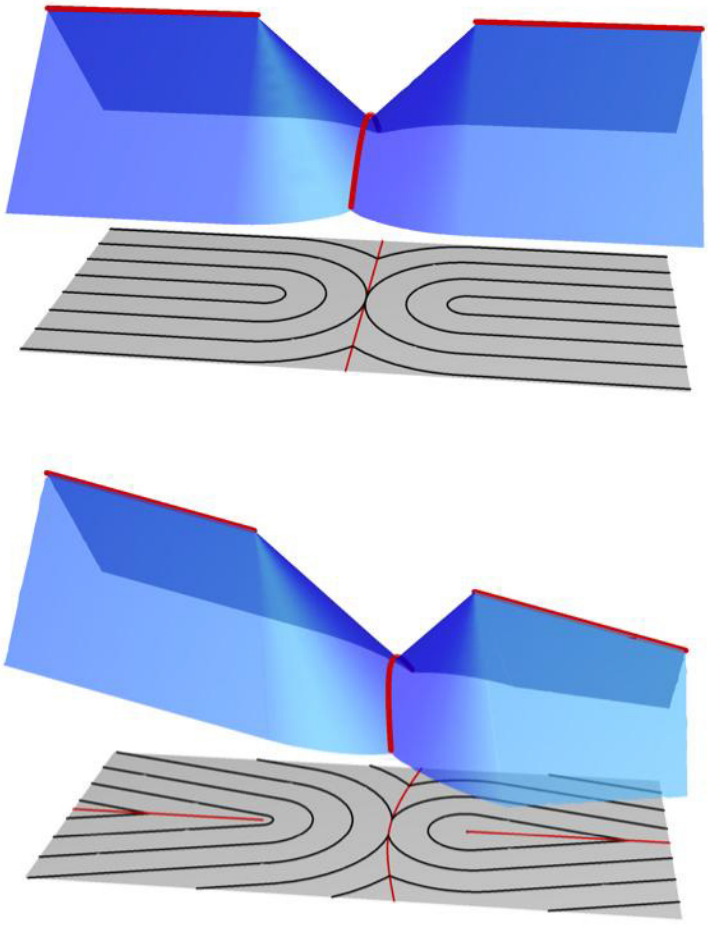

Figure 7.3: Two-dimensional slice ($y = 0$) of a tilt grain boundary configuration, shown both in real space and in Minkowski space. Note the "ridge" at which there is a change in orientation of the ground state: under a boost (bottom) this ridge becomes an additional focal set.

branch of the hyperbola $\overline{\Sigma} = \{z^2 - \phi^2 = -r^2;\, x = y = 0\}$ with $\phi < 0$. Moving out along the hyperbola towards $z \to \pm\infty$ the light rays from any point of the ellipse asymptote onto the directions $(0, 0, \pm 1, -1)$ corresponding to the equivalent ground states $\phi = \mp z$ seen outside of the cyclides, Fig. 7.3. Importantly, although these are equivalent they are not the same ground state, but differ by a change in orientation occuring at the ellipse Σ, which here has the appearance of a $+\frac{1}{2}$ disclination loop. A boost along the x-direction rotates the asymptotic directions to $(\gamma\beta, 0, \pm 1, -\gamma)$, *i.e.*, the cyclide region now connects the ground states $\phi' = -\beta x' \mp \gamma^{-1} z'$, rotated relative to each other by $2\arcsin(\beta)$. Since the boosted ground states are no longer equivalent, they no longer join smoothly on the

plane, $z'=0, \phi'=-\beta x'$, but rather form a plane of cusps (Fig. 7.3). The tilt-grain-boundary construction provides one example of this generic behavior, that additional focal sets are produced when a non-orientable texture is subjected to a Lorentz transformation. Finally let us remark that, although we have considered only one cyclide region, it is clear that any number can be accommodated by tiling the cuspy $z=\phi=0$ plane of the rest frame with circles, each circle being the elliptical focal set of a cyclide domain – in fact, this is what is seen in experiment [61].

This chapter has demonstrated the connection between focal conics in $\mathbb{R}^d$ and null hypersurfaces in $\mathbb{R}^{d,1}$. Specifically, in three dimensions we have shown that simple textures with codimension 2 focal sets arise from intersections of cones and planes. The addition of the extra dimension clarifies the action of the isometries, just as an extra dimension reveals the simplicity of the Möbius Transformations of the plane in terms of the symmetries of the Riemann sphere [5]. Further work will elucidate other smectic structures, such as Apollonian packings and oily-streak textures and will demonstrate that energetic calculations are natural in rest-frame coordinates. Our approach suggests that methods of general relativity will be fruitfully used for the study of defects on curved surfaces [87]. We hope that the structure of defects presented here along with the results of [19] set the framework for a combined theory of disclinations, focal sets, and dislocations.

Chapter 8

In Which a Conclusion is Reached and We Say Goodbye

The study of defects has proven an extremely powerful method for analyzing a wide range of condensed matter systems. The interaction between singularities dominate the elastic energy particularly in nonlinear problems. We have applied these methods to two classes of problems: exploiting elastic instabilities for the rational design of two dimensional patterns with long ranged order and textures in smectic liquid crystals which are governed by sets of defects.

In particular, we have shown that arrays of dislocation dipoles accurately model the buckling instability of holes in a hydrostatically compressed thin elastic sheet confined to two dimensions. Simple interactions between two dislocation dipoles derived from linear elasticity theory are capable of reproducing the diamond plate pattern seen for a square lattice of circular holes. Because of the limited number of Bravais lattices in two dimensions, we turn to a new cylindrical topology to increase the diversity of the instability generated patterns. In addition to calculations, we have conducted an experiment to demonstrate that the dislocation dipole approximation accurately predicts patterns in this new topology. We have explored the square, hexagonal, and honeycomb lattices, and the effect that the orientation in which they are wrapped around the cylinder has on the patterns they produce. An algorithm has not yet been created to assign the positions of holes in order to generate a specific patter.

Defects in smectic liquid crystals often dominate the behavior of their textures. In the both the twist-grain-boundary phase and helical nanofilament phase the proliferation of defects results from the frustration between macroscopic chirality and layered systems. Although similar, these textures have a distinctly different morphologies. The hierarchical

helical nanofilament phase is based on coherently rotating helical bundles, containing $5-7$ layers each, which then assemble into a hexagonal lattice forming bulk texture. This phase occurs at higher chirality and reduced temperature than the twist-grain-boundary phase.

Finally, we examine two limiting cases of the achiral Landau-de Gennes free energy, bending energy dominated and compression energy dominated. Smectic layers often assume the form of a minimal surface in order to minimize bending energy. By studying the topology of minimal surfaces, we gain insight into the comparable smectic. Riemann's minimal surface, for example, is constructed topologically out of two screw dislocations of opposite handedness, yet it has the morphology of a pore. In the opposite limit, focal conic domains, the ubiquitous smectic texture, result from enforcing equally spaced layers. The complexity of geometric construction makes the study of multiple domains simultaneously difficult, if not impossible. By viewing the smectic layers as projections of null hypersurfaces living in one higher dimension, we exploit Poincaré symmetry to study textures created from multiple focal conic domains, including the tilt grain boundary and the iconic *treillis à réseau*.

Acknowledgements

I would like to thank the Acadamy, my director, R. D. Kamien, my co-stars, G. P. Alexander, B. G. Chen, C. D. Santangelo, and the rest of the crew. Entertainment during production was provided by The Beatles, Pink Floyd, Led Zeppelin, and various artists from the '80s. This program was made possible by the National Science Foundation and viewers like you.

Bibliography

[1] Edwin A. Abbott, *Flatland: A Romance of Many Dimensions* (Barns & Noble Books, New York, 1963).

[2] Milton Abramowitz and Irene A. Stegun, *Handbook of Mathematical Functions with Formulas, Graphs, and Mathematical Tables* (National Bureau of Standards, Washington, D.C., 1972), 10th edition.

[3] A. A. Abrikosov, Soviet Physics JETP **5**, 1174 (1957).

[4] Gareth P. Alexander, Bryan Gin-ge Chen, Elisabetta A. Matsumoto, and Randall D. Kamien, Physical Review Letters **104**, 257802 (2010). "Copyright (2010) by the American Physical Society."

[5] D. N. Arnold and J. Rogness. *Möbius Transformations Revealed*, in *Math-Film Festival 2008*, edited by K. Polthier *et al.* (Springer, New York, 2008), http://www.ima.umn.edu/videos/mobius.php.

[6] John M. Ball, Quarterly of Applied Mathematics **4**, 719 (1998).

[7] Katia Bertoldi, Mary C. Boyce, S. Deschanel, S. M. Prange, and Tom Mullin, Journal of the Mechanics and Physics of Solids **56**, 2642 (2008).

[8] Katia Bertoldi, Pedro M. Reis, Stephen Willshaw, and Tom Mullin, Advanced Materials **22**, 361 (2010).

[9] R. Bidaux, N. Boccara, G. Sarma, L. De Seze, Pierre Gilles de Gennes, and O. Parodi, Journal de Physique **34**, 661 (1973).

[10] Christophe Blanc and Maurice Kléman, Physical Review E **62**, 6739 (2000).

[11] Yves Bouligand, Journal de Physique **33**, 525 (1972).

[12] Yves Bouligand and Françoise Livolant, Journal de Physique **45**, 1899 (1984).

[13] Ned Bowden, Scott Brittain, Anthony G. Evans, John W. Hutchinson, and George M. Whitesides, Nature **393**, 146 (1998).

[14] Arthur Cayley, Philosophical Magazine **XXIX**, 19 (1865).

[15] E. Cerda and L. Mahadevan, Physical Review Letters **90**, 074302 (2003).

[16] Enrique Cerda, K. Ravi-Chandar, and L. Mahadevan, Nature **419**, 579 (2002).

[17] P. M. Chaikin and Tom C. Lubensky, *Principles of Condensed Matter Physics* (Cambridge University Press, Cambridge, England, 1995).

[18] Edwin P. Chan and Alfred J. Crosby, Advanced Materials **18**, 3238 (2006).

[19] Bryan Gin-ge Chen, Gareth P. Alexander, and Randall D. Kamien, Proceedings of the National Academy of Sciences USA **106**, 15577 (2009).

[20] Xi Chen and John W. Hutchinson, Scripta Materialia **50**, 797 (2004).

[21] Xi Chen and John W. Hutchinson, Journal of Applied Mechanics **71**, 597 (2004).

[22] Xi Chen and Jie Yin, Soft Matter (2010).

[23] Tobias H. Colding and William P. Minicozzi, Proceedings of National Academy of Sciences USA **103**, 11106 (2006).

[24] Pierre Gilles de Gennes, Solid State Communications **10**, 753 (1972).

[25] Pierre Gilles de Gennes and Jaques Prost, *The Physics of Liquid Crystals* (Oxford University Press, 1993), 2nd edition.

[26] Brian A. DiDonna and Randall D. Kamien, Physical Review Letters **89**, 215504 (2002).

[27] Brian A. DiDonna and Randall D. Kamien, Physical Review E **68**, 041703 (2003).

[28] I. Dozov, Europhysics Letters **56**, 247 (2001).

[29] David J. Earl, Mikhail A. Osipov, Hideo Takezoe, Yoichi Takanishi, and Mark R. Wilson, Physical Review E **71**, 021706 (2005).

[30] Albert Einstein, Annalen der physik **17**, 891 (1905).

[31] J. Fernsler, L. E. Hough, Renfan Shao, Joseph E. Maclennan, Laurence Navailles, M. Brunet, N. V. Madhusudana, O. Mondain-Monval, C. Boyer, and J. A. Zasadzinski, Proceedings of the National Academy of Sciences **102**, 14191 (2005).

[32] F. C. Frank, Discussions of the Faraday Society **25**, 19 (1958).

[33] G. Friedel and E. Friedel, Le Journal de Physique et le Radium **2**, 133 (1931).

[34] G. Friedel and F. Grandjean, Bulletin de la Société Française de Minéralogie et de Crystallographie **33**, 409 (1910).

[35] F. G. Friedlander, Mathematical Proceedings of the Cambridge Philosophical Society **43**, 360 (1947).

[36] John W. Goodby, M. A. Waugh, S. M. Stein, E. Chin, Ronald Pindak, and J. S. Patel, Nature **337**, 449 (1989).

[37] John W. Goodby, M. A. Waugh, S. M. Stein, E. Chin, Ronald Pindak, and J. S. Patel, Journal of the American Chemical Society **111**, 8119 (1989).

[38] A. E. Green, Proceedings of the Royal Society of London. Series A **176**, 121 (1940).

[39] A. E. Green and W. Zerna, *Theoretical Elasticity* (Clarendon Press, Oxford, England, 1954).

[40] Bartosz A. Grzybowski, Kyle J. M. Bishop, Christopher J. Campbell, Marcin Fialkowski, and Stoyan K. Smoukov, Soft Matter **1**, 114 (2005).

[41] S. W. Hawking and G. F. R. Ellis, *The Large Scale Structure of Space-Time* (Cambridge University Press, Cambridge, England, 1973).

[42] J. H. Heinbockel, *Introduction to Tensor Calculus and Continuum Mechanics* (Trafford, Victoria, B.C., 2001).

[43] Stephan Herminghaus, Karin Jacobs, Klaus Mecke, Jörg Bischof, Andreas Fery, Mohammed Ibn-Elhaj, and Stefan Schlagowski, Science **282**, 916 (1998).

[44] John Price Hirth and Jens Lothe, *Theory of Dislocations* (Wiley & Sons, New York, 1982), 2nd edition.

[45] Douglas P. Holmes and Alfred J. Crosby, Advanced Materials **19**, 3589 (2007).

[46] L. E. Hough, Hee-Tae Jung, Daniel Krüerke, M. S. Heberling, Michi Nakata, Christopher Jones, D. Chen, Darren R. Link, J. A. Zasadzinski, Gerd Heppke, Jürgen P. Rabe, W. Stocker, Eva Körblova, David M. Walba, Matthew A. Glaser, and Noel A. Clark, Science **325**, 456 (2009).

[47] R. C. J. Howland, Proceedings of the Royal Society of London. Series A **148**, 471 (1935).

[48] R. C. J. Howland and R. C. Knight, Philosophical Transactions of the Royal Society of London. Series A **238**, 357 (1939).

[49] Klaus Janich, Acta Applicandae Mathematicae **8**, 65 (1987).

[50] G. B. Jeffery, Philosophical Transactions of the Royal Society of London. Series A **221**, 265 (1921).

[51] Randall D. Kamien, Applied Mathematics Letters **14**, 797 (2001).

[52] Randall D. Kamien, Science **315**, 1083 (2007).

[53] Randall D. Kamien and Tom C. Lubensky, Physical Review Letters **82**, 2892 (1999).

[54] Randall D. Kamien and Christian D. Santangelo, Geometriae Dedicata **120**, 229 (2006).

[55] Jyoichi Kaneko, Memoirs of the Faculty of Science. Kyushu University. Series A. **40**, 51 (1986).

[56] Eleni Katifori, Silas Alben, and David R. Nelson, Physical Review E **79**, 056604 (2009).

[57] Dahl-Young Khang, Hanqing Jiang, Young Huang, and Rogers John A, Science **311**, 208 (2006).

[58] Yael Klein, Efi Efrati, and Eran Sharon, Science **315**, 1116 (2007).

[59] W. H. Kleiner, L. M. Roth, and S. H. Autler, Physical Review A **133**, 1226 (1964).

[60] Maurice Kléman and Oleg D Lavrentovich, European Physical Journal E **2**, 47 (2000).

[61] Maurice Kléman and Oleg D. Lavrentovich, Liquid Crystals **36**, 1085 (2009).

[62] C. B. Kooi and A. Verruijt, Tunneling and Underground Space Technology **16**, 59 (2001).

[63] L. D. Landau and E. M. Lifshitz, *Theory of Elasticity* (Elsevier, New York, 1986), 3rd edition.

[64] Joseph Larmor, Proceedings of the Royal Society of London. Series A - Containing Papers of a Mathematical or Physical Character **190**, 205 (1897).

[65] M. Maurice Lévy, Journal de Mathématiques Pures et Appliquées **10**, 5 (1884).

[66] Chih-Bing Ling, Journal of Applied Physics **19**, 77 (1948).

[67] Darren R. Link, Gorgio Natale, Renfan Shao, Joseph E. Maclennan, Noel A. Clark, Eva Körblova, and David M. Walba, Science **278**, 1924 (1997).

[68] Françoise Livolant and Yves Bouligand, Molecular Crystals and Liquid Crystals **166**, 91 (1989).

[69] F. London and H. London, Proceedings of the Royal Society of London. Series A-Mathematical and Physical Sciences **149**, 71 (1935).

[70] Edward Hough Augustus Love, *A Treatise on the mathematical theory of elasticity* (Cambridge University Press, Cambridge, England, 1906).

[71] N. Manton and P. Sutcliffe, *Topological Solitons* (Cambridge University Press, 2004).

[72] Xiaoming Mao and Tom C. Lubensky, Physical Review E **83**, 011111 (2011).

[73] Elisabetta A. Matsumoto, Gareth P. Alexander, and Randall D. Kamien, Physical Review Letters **103**, 257804 (2009). "Copyright (2009) by the American Physical Society."

[74] Elisabetta A. Matsumoto and Randall D. Kamien, Physical Review E **80**, 021604 (2009). "Copyright (2009) by the American Physical Society."

[75] James Clerk Maxwell, The Quarterly Journal of Pure and Applied Mathematics **9**, 111 (1867).

[76] N. David Mermin, Reviews of Modern Physics **51**, 591 (1979).

[77] Tom Mullin, S. Deschanel, Katia Bertoldi, and Mary C. Boyce, Physical Review Letters **99**, 084301 (2007).

[78] Yoichiro Nambu, Physical Review Letters **4** (1960).

[79] Laurence Navailles, B. Pansu, L. Gorre-Talini, and Huu-Tinh Nguyen, Physical Review Letters **81**, 4168 (1998).

[80] J. C. C. Nitsche, *Lectures on Minimal Surfaces*, (translated by J. M. Feinberg) (Cambridge University Press, Cambridge, England, 1989).

[81] Hiroko Niwano, Michi Nakata, Jirakorn Thisayukta, Darren R. Link, Hideo Takezoe, and Junji Watanabe, Journal of Physical Chemistry B **108**, 14889 (2004).

[82] C. W. Oseen, Transactions of the Faraday Society **29**, 883 (1933).

[83] V. Poénaru and G. Toulouse, Journal de Physique **38**, 887 (1977).

[84] Scott Renn and Tom C. Lubensky, Physical Review A **38**, 2132 (1988).

[85] Christian D. Santangelo and Randall D. Kamien, Physical Review Letters **96**, 137801 (2006).

[86] Christian D. Santangelo and Randall D. Kamien, Physical Revew E **75**, 011702 (2007).

[87] Christian D. Santangelo, Vincenzo Vitelli, Randall D. Kamien, and David R. Nelson, Physical Review Letters **99**, 017801 (2007).

[88] Tomoko Sekine, Teruki Niori, Masato Sone, Junji Watanabe, Suk-Won Choi, Yoichi Takanishi, and Hideo Takezoe, Japanese Journal Of Applied Physics **36**, 6455 (1997).

[89] Tomoko Sekine, Teruki Niori, Junji Watanabe, T. Furukawa, Suk-Won Choi, and Hideo Takezoe, Journal of Materials Chemistry **7**, 1307 (1997).

[90] James P. Sethna and Maurice Kléman, Physical Review A **26**, 3037 (1982).

[91] Andrew J. Slaney and John W. Goodby, Liquid Crystals **9**, 849 (1991).

[92] Andrew J. Slaney and John W. Goodby, Journal of Materials Chemistry **1**, 5 (1991).

[93] Anton Souslov, Andrea J. Liu, and Tom C. Lubensky, Physical Review Letters **103**, 205503 (2009).

[94] G. Srajer, Ronald Pindak, M. A. Waugh, John W. Goodby, and J. S. Patel, Physical Review Letters **64**, 1545 (1990).

[95] A. C. Stevenson, Proceedings of the Royal Society of London. Series A **184**, 218 (1945).

[96] Kai Sun, Hong Yao, Eduardo Fradkin, and Steven A. Kivelson, Physical Review Letters **103**, 046811 (2009).

[97] Yoichi Takanishi, Gyo Jic Shin, Jin Chul Jung, Suk-Won Choi, Ken Ishikawa, Junji Watanabe, Hideo Takezoe, and Pierre Toledano, Journal of Materials Chemistry **15**, 4020 (2005).

[98] Toyoichi Tanaka, Shao-Tang Sun, Yoshisugu Hirokawa, Seiji Katayama, John Kucera, Yoshiharu Hirose, and Tanayuki Amiya, Nature **325**, 796 (1987).

[99] Jirakorn Thisayukta, Hideo Takezoe, and Junji Watanabe, Japanese Journal of Applied Physics **40**, 3277 (2001).

[100] R. Von Mises, NACA Technical Note **AD136219**, 1 (1933).

[101] Peter L. Walker, *Elliptic Functions: A Constructive Approach* (John Wiley & Sons, New York, 1996).

[102] David C. Wright and N. David Mermin, Reviews of Modern Physics **61**, 385 (1989).

[103] Ying Zhang, Elisabetta A. Matsumoto, Anna Peter, Pei-Chun Lin, Randall D. Kamien, and Shu Yang, Nano Letters **8**, 1192 (2008).

[104] Ying Zhang, Jason C. Reed, and Shu Yang, Acs Nano **3**, 2412 (2009).

[105] Xuelian Zhu, Ying Zhang, Dinesh Chandra, Shih-Chieh Cheng, James M. Kikkawa, and Shu Yang, Applied Physics Letters **93**, 161911 (2008).